# INFLUENCE OF SIZE AND SPECIFICITY ON PHARMACOKINETICS, BIODISTRIBUTION, AND TUMOR TARGETING OF WIDELY USED BIOLOGICS: FUNDAMENTAL UNDERSTANDING TO APPLICATIONS

A Dissertation

Presented to the Faculty of the Graduate School

of Cornell University

In Partial Fulfillment of the Requirements for the Degree of

Doctor of Philosophy

by

Jeerapond Leelawattanachai

August 2014

# INFLUENCE OF SIZE AND SPECIFICITY ON PHARMACOKINETICS, BIODISTRIBUTION, AND TUMOR TARGETING OF WIDELY USED BIOLOGICS: FUNDAMENTAL UNDERSTANDING TO APPLICATIONS

Jeerapond Leelawattanachai, Ph.D.

Cornell University 2014

Specific and efficient targeting to tumors as well as many other diseases is a key to the success in several therapeutic interventions. The specificity offers the ideal way to transport and deliver a variety of biomedical entities for diagnosis, prevention, and treatment, selectively to the targeted sites. These specific targeting and delivery potentially lead to the advancement of noninvasive diagnostics and provide safer therapeutic options. Numerous factors can effectuate and determine the accomplishment of the site-specific targeting. In this dissertation, I have comprehensively investigated the influence of size and specificity on pharmacokinetics, biodistribution and tumor targeting of commonly used biologics. Six different fluorescently-labeled biologics, including two antibodies, two antibody fragments, serum albumin, and streptavidin, were used in the study to examine their distribution at whole body, ex-vivo tissue, and cellular levels in mice bearing human cervical cancer cells. The understanding of these pharmacokinetic parameters and tumor targeting outcomes would assist not only in future molecular imaging design but also therapeutic intervention development. Thereby it could render opportunity for novel treatment regimens.

Utilizing the fundamental understanding in pharmacokinetics and biodistribution from our study, we have engineered two different targeted delivery systems for both imaging

and delivery applications. The first system is super paramagnetic iron oxide (SPIO) nanoparticle for magnetic resonance imaging (MRI) application. The second system is polyplex nanoparticle for large genetic content delivery. Among a wide range of targeting molecules, intercellular adhesion molecule (ICAM)-1 is of great interest as a versatile targeting molecule due to its constitutively over-expressed in many carcinomas including breast, colon, non-small cell lung, and gastric tumors compared to corresponding normal epithelial cells, in tumor vasculature within an inflammatory network, and in inflammation sites. Targeting ICAM-1 would offer a great benefit through combinatorial targeting strategies to both tumor cells and tumor-associated endothelial cells. Validated in in vivo mouse models, our targeted delivery systems localized preferentially to the tumors, inflamed vasculature, as well as systemic and subcutaneous inflammation. The studies presented here demonstrate a comprehensive understanding of size and specificity parameters to tumor targeting outcomes, along with two examples of targeted delivery systems for imaging and therapeutic implications. We anticipate this work may greatly contribute to successful translation of the molecular imaging and therapeutic delivery systems into the clinic.

# BIOGRAPHICAL SKETCH

Jeerapond is the first child born to a Thai family in January of 1985. She is a daughter of Suchai Leelawattanachai, an entrepreneur in a zipper and textile business, and Sujeera Jeeyasak, a lecturer in Ramathibodi School of Nursing, Faculty of Medicine Ramathibodi Hospital. Jeerapond grew up in Bangkok, a capital city of Thailand, and graduated from Mahidol Wittayanusorn School, the special science school for the gifted in Thailand. During her high school education, she was subconsciously cultivated to be a researcher. Since then, she has had strong desires to earn a Ph.D. and to be an expert in a particular field. Upon her graduation from high school, she was granted a Thai government's scholarship based on her academic qualifications and examination to study in Faculty of Science, Mahidol University, from which she graduated with a bachelor's degree in Physics with first class honors. During her study at Mahidol University, she developed her interest in physics and mathematical modeling and chose to participate and work in a biophysics research group. In the group, she conducted a research project called *Modeling of Signal Transduction via Dynamics of G-Protein-Coupled Receptors: Internalization Consideration.* This project explains the agonist potency and efficacy of drugs and provides further mechanistic understanding in signal transduction that is difficult to detect using experimental observation alone. Her research project was selected to be presented in science project exhibitions, symposiums, and conference, and was published in a peer reviewed journal paper, in which she was a first author.

After completing her undergraduate education, Jeerapond was awarded the Royal Thai Government Scholarship to pursue her graduate study in the United States. Jeerapond

came to Cornell in 2008 and has been worked with Dr. Moonsoo Jin, on various drug/contrast agent delivery systems. By utilizing diverse molecular biology, biochemistry, and biophysical tools, the Jin Lab aims to develop unique therapeutic molecules and nanoparticles to treat cancers and inflammatory diseases. Since joining the lab, Jeerapond has had the great opportunities to collaborate with several research labs, biotechnology companies, cancer centers, and medical schools. Such interactions provide her valuable experiences that are essential to enhance her competence as a researcher. Her research was selected as a top-10 finalist nominee from Cornell University including Weill Cornell Medical College for the 2010 Howard Hughes Medical Institute International Student Research Fellowship Program.

Upon her graduation this fall, she will return to Thailand to join a research institute, National Nanotechnology Center (NANOTECH) at Thailand Science Park as a research scientist.

Dedicated to my parents, grandparents, sister, and brother.

For their endless love, support, and encouragement.

# ACKNOWLEDGMENTS

I am grateful for many people who helped me get through graduate school and finish this thesis. First of all, I am indebted to my advisor, Dr. Moonsoo Jin, for taking me on as his student and for leading me through many aspects of my research career. He has taught me, both consciously and unconsciously, how much it takes to be a great scientist. His enthusiasm to scientific research has never flatted. He always comes up with numerous interesting ideas in research and constantly initiates insightful scientific discussions. He is willing to work hard and to devote his entire time to scientific research. I appreciate all his contributions of time, ideas, and guidance to make my Ph.D. experience productive and fruitful. I am deeply grateful to Dr. Jin for his scientific advice and knowledge and many insightful discussions and suggestions. I am also thankful for the excellent model he has provided as a remarkable scientist full with determination and commitment to his research career.

I would also like to thank my Ph.D. committee members, Dr. Susan Daniel and Dr. Rasa Zarnegar for their helpful research advice and suggestions from their own expertise. Additionally, I am very thankful to Dr. William Frayer and Dr. Zarnegar for bringing me to the operation room and office hours to see the patients. Such invaluable experiences have made me appreciate how important my Ph.D. research can be when it is translated to clinics some day. I am especially grateful to Dr. Peter Doerschuk for all the help and encouragement he has given me throughout my PhD study. I would also like to extend a special thank you to Belinda for her responsive administrative support and the warmest greeting every time we met for the past years.

Many thanks to my colleagues in the Jin research group for their help, support and friendship. I owed a big thank you to Zoe, Ling, Goose, Xuebo, Yvonne, Spencer, Roisin and Taehyun for teaching me lab techniques and several fruitful scientific discussions. I also thank my dear labmates, Keon Woo, Turner, Marjan, Yogi, Richard, Kevin, Tricia, Marina, Leslie, Brain, Nina, Ada, Kathleen, Jared, Yoshi, and Karen for being supportive and wonderful, and specially, Joy, Tarek, Tanwi, Emily, Rinki, and Hao for giving me the opportunity to learn more about being a good mentor. I thank you all for being diligent and excellent students. I am especially grateful and indebted to Joy-Praveesuda Michael, my first student and one of my greatest friends. Without her, I could not make it this far. I would also like to thank our neighbors, the Shen Lab and the Fischbach Lab, for always generously sharing reagents and equipment with me, with special thanks to Pengcheng, Lihua, and Nikolai for their technical help, discussions, and wonderful friendship.

A large part of my success as a graduate student and researcher comes from the collaborations with many experts in the field. I thank Dr. Bruce Weintraub, and Dr. Mariusz Szkudlinski from Trophogen Inc. for introducing me to great problems in biotechnology field and giving me an opportunity for involvement in product development. I also thank Dr. Jason Lewis and Dr. Brian Zeglis from Memorial Sloan Kettering Cancer Center for the help in positron emission tomography imaging, Dr. Thom Santisakultarm from the Schaffer lab for the help in multiphoton imaging, Carol Bayles and Johanna Cruz from Microscopy and Imaging facility for Confocal and whole body mouse imaging, respectively, and Sylvia Allen from Weill hall mouse facility for attending and taking good care of the research animals.

I gratefully acknowledge the funding sources that made my Ph.D. work possible. I was funded by the Royal Thai Government Scholarship for my first 5 years and was awarded

Colman Fellowship for my last semester. My research work was also supported by Cornell Institutional Seed Grant (Weill Surgery-BME), the American Heart Association, and the National Institutes of Health.

My time at Cornell was made enjoyable in large part due to the many friends and roommates that became part of my life. I am exclusively grateful to Dr. Kitipong Assatarakul, Rarinthorn Thammakulkrajang, Dr. Sana Mujahid, Prasit Deewatthanawong, and Moodjalin Sudcharoen for everything they have done for me. They offered me innumerable helps, intellectual and mental support, and the life-long friendship. I am thankful for time spent with several Thai friends here at Cornell. They made me feel like home somehow when being around them, even thought in fact I am physically more than 8000 miles away from home. Thanks P' Namtip, P' Pim, Pao, Annie, Tai (Duangkamon), P' Wahn, P' Tee, Na' Nu, Peung, P' Jeab, P' Mook, P' Mint, P' Natt, P' Pond, P' Noi, P' Deedee, P' Om, P' Art, Jack, Boom, N' Paint, Ping, Som, N' Bo, N' Dutch, Kun, and Oath, very much for the warmth and the wonderful memories. I also would like to express my sincere appreciation to the lovely Hu family for accommodating me for my last year of Ph.D. education.

I am extremely grateful and thankful to my beloved boyfriend, Jiahe Li, who has always been supportive both scientifically and mentally in my research, and could always make me feel better all those times when I thought I could never make it possible. He is the person who steadily proves to me his resilience to life and strong commitment to research that constantly inspire me.

Lastly, I would like to thank my family for all their love and encouragement. My parents and grandparents enlightened me with a passion for science, and supported me for

pursuing my dream. Thank my mom and dad who have always been my role models through hard working and have proven to me with determination and perseverance ones can reach the seemingly unreachable star. Thank my loving, supportive, and encouraging sister and brother who have been taking care of our parents and grandparents very well, making sure everything goes very well and there is nothing to worry about so that I can keep focusing on my research. Thank you so much.

# TABLE OF CONTENTS

# CHAPTER 1

# INTRODUCTION

## Inflammation, cancer, and cancer metastasis

Cancer results from the outgrowth of a clonal population of cells in tissues. Central to the development of cancer, referred to as carcinogenesis, are genetic changes that endow these "cancer cells" with many of the hallmarks of cancer, including 1) sustaining proliferative signaling, 2) evading growth suppressors, 3) resisting cell death, 4) enabling replicative immortality, 5) inducing angiogenesis, 6) activating invasion and metastasis, 7) reprogramming of energy metabolism, and 8) evading immune destruction [1]. Cancer could also be considered as a step-wise development functionally grouped into three phases: initiation-genomic changes within the cancer cell, promotion-clonal expansion of the initiated cells, and progression-substantial growth in tumor size as well as metastasis [2, 3]. However, while the genetic changes that occur within cancer cells themselves, such as activated oncogenes or dysfunctional tumor suppressors, together with cell autonomous promotion and progression properties are necessary for tumorigenesis, they are not sufficient. In fact, several research studies have identified that the neoplastic processes; fostering proliferation, survival, and migration require support from tumor microenvironment, which is largely orchestrated by inflammatory cells [3, 4]. These inflammatory cells promote early neoplastic process by producing an attractive environment for tumor growth, facilitating genomic instability, and promoting angiogenesis [3]. They also produce chemokines and

cytokines, which regulate the growth, migration, differentiation, and metastasis of neoplastic cells [3, 5, 6]. In the late tumorigenic process, neoplastic cells also divert inflammatory mechanisms such as selectin–ligand interactions, MMP production, and chemokine functions to favor neoplastic spread and metastasis [3].

**Cancer targeting strategies**

The major requirement for the success in cancer treatment and imaging is that the therapeutic/imaging agents must efficiently and selectively reach the targeting cells in vivo in optimal quantities with minimal off-targeted cell localization. Over the past century, since Paul Ehrlich, considered the "father of chemotherapy", suggested the concept of a "magic bullet", i.e., "a drug that selectively attaches to diseased cells but is not toxic to healthy cells" [7], a great deal of effort has been made for this direction, focusing particularly on cancer treatment. To reach cancer cells in a tumor, a therapeutic agent must make its way into the chaotic blood vessels of the tumor, across the vessel wall into the interstitium, then transport through the interstitial space and lymphatics, and finally bind to cancer cells [8, 9]. Moreover, during the journey, the therapeutic molecule may bind nonspecifically to proteins or other tissue components, which leads to the rapid clearance and metabolization within seconds after i.v. administration [10, 11]. In addition, several other obstacles, as outlined in Table 1 [12], still persist and need to be overcome.

Many different imaging and delivery systems have been innovatively developed over the past years to overcome these barriers, and to improve their pharmacokinetic profile and their accumulation at the target site. Several strategies have been conceived for nanomedicine

directed to putative biological targets including passive drug targeting, active targeting to cancer cells, active targeting to endothelial cells, and triggered drug delivery (using stimuli-responsive carrier materials) [13-16], as shown in Figure 2.

**Table 1.** Barriers limiting the delivery of i.v. administrated anticancer agents to tumors. Note that several barriers are inter-related, and that not all barriers apply to all types of (chemo-) therapeutic agents. Table is from the article originally published in [12]

| Barriers to drug delivery to tumors | | | |
|---|---|---|---|
| Anatomical barriers | Physiological barriers | Chemical barriers | Clinical barriers |
| Vascular endothelium | Renal filtration | Low solubility | Low efficacy |
| Perivascular space | Hepatic degradation | Low stability | High toxicity |
| Cellular membrane | High tumor cell density | Low molecular weight | Need for hospitalization |
| Nuclear membrane | High interstitial fluid pressure | Large volume of distribution | Frequent administration |
| Blood brain barrier | Drug efflux pumps | Charge interactions | Low cost-effectiveness |

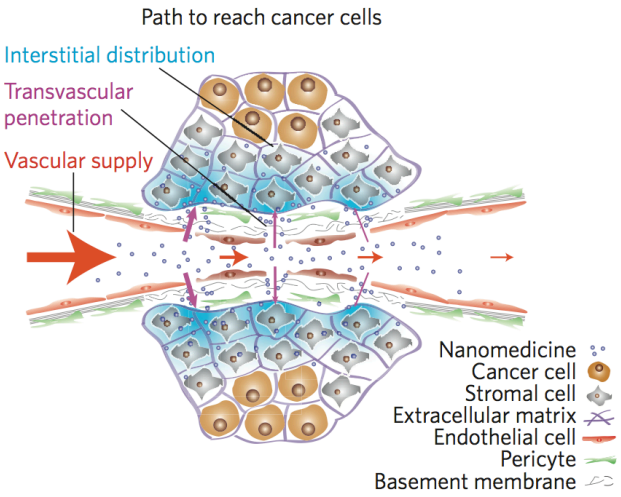


**Figure 1.** The transport barriers to tumor-targeted delivery. Therapeutic agents enter a tumor through its blood supply. These drugs must then extravasate cross the microvascular walls to penetrate into tissues. The drugs then diffuse through the extravascular space and eventually distribute to their target cancer cells. The figure is from the article originally published in [9]. In addition to this, a large number of other barriers need to be considered including e.g. hepatic and enzymatic degradation, the high interstitial fluid pressure that is typical of tumors, cellular and nuclear membranes, and the presence of drug efflux pumps [12].

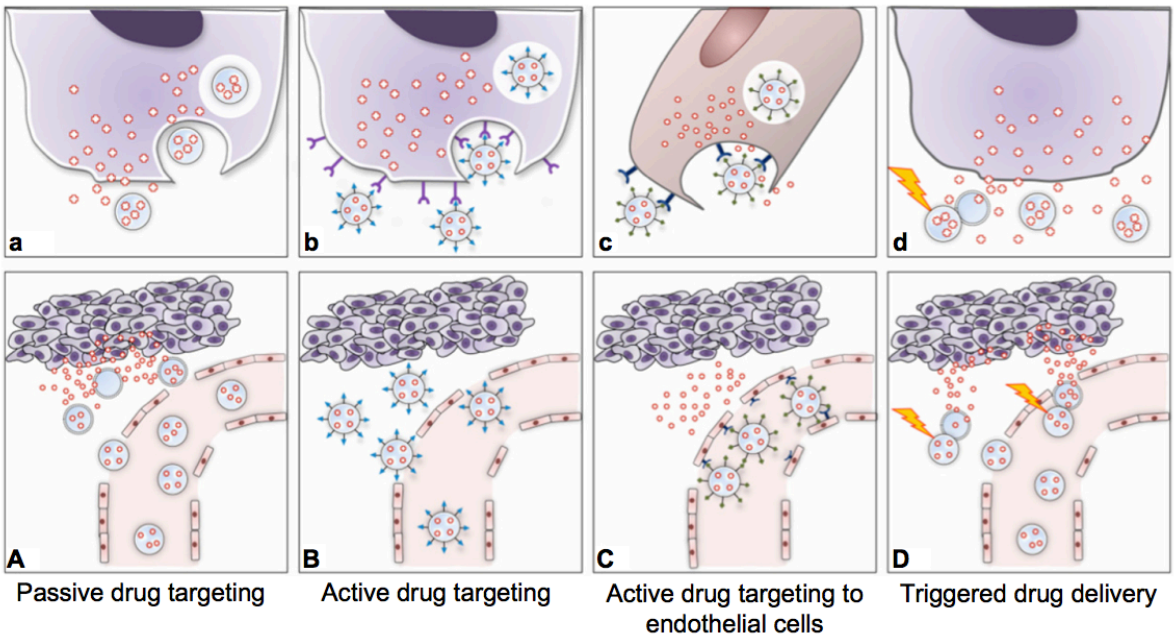


**Figure 2.** Strategies used for biomedical entity targeting and localization to tumor cells. (A) Passive drug targeting. Circulating nanoparticles passively extravasate in solid tumor tissue, by means of the enhanced permeability and retention effect-EPR effect, the property by which nanoparticles tend to accumulate in tumor tissue much more than they do in normal tissue due to the enhanced permeability of blood vessels, i.e., through the disorganized and leaky vasculature surrounding the solid tumor together with the absence of lymphatic drainage (a) After distributed through the extracellular matrix, the released drug diffuses into the cancer cells. (B) Active targeting to cell surface receptors (over-) expressed by cancer cells. Once nanoparticles passively extravasate and concentrate in the target tissue via the EPR effect, the presence of ligands grafted onto the nanoparticle surface enable specific targeting and, in some cases, enhanced uptake and internalization of the nanoparticles via receptor-mediated endocytosis. (b) Tumor-specific ligands on the nanoparticles bind to cell surface receptors, concentrating drug to the tumor cell vicinity and, in case of internalization-prone cell surface receptors, triggering internalization, of the nanoparticles into the cell. The

drug is then released from the nanoparticle, due to acidic pH in endosomes, and diffuses into cytoplasm. (C) Active targeting to receptors (over-) expressed by endothelial cells. Nanoparticles can be targeted to bind to angiogenic endothelial cell surface receptors with the aims of: eradicating tumor blood supply to deprive cancer cells of oxygen and nutrients (c), and improving drug delivery to tumor cells via the EPR effect with synergistic targeting both the vascular tissue and tumor cells. (D) Triggered drug delivery by stimuli-sensitive nanomedicines. After passively accumulating at the tumor via EPR or while circulating in the tumor vasculature (d), the nanoparticles can be activated, to release their contents, by external stimuli, like hyperthermia, light, magnetic fields, ultrasound. Figure 3 (a-d, A-D) are reproduced from [17].

*Passive targeting*

The pathophysiological characteristics of solid tumors feature the enhanced permeability of tumor blood vessels, in contrast to the vasculature in healthy tissues, and the lack of lymphatic drainage. The enhanced permeability in tumor microvasculature is a result of poorly differentiated vasculature, abnormal branching and enlarged interendothelial gaps. These large gaps, up to ~600 nm in size comparing to ~5 nm in normal vessels [17-19], allow for extravasation of nanoparticles into the tumor interstitium. Together with the lack of functional lymphatics, the enhanced permeation and retention effect (EPR effect) can be exploited as a passive targeting mechanism for drug delivery through selective extravasation and accumulation of long-circulating therapeutic agents in the tumor interstitium over time. This passive targeting mechanism is arguably the most important strategy for improving the delivery. The vast majority of currently approved nanomedicines for tumor targeting in

clinics rely heavily on the EPR effect, e.g. Myocet (non-PEGylated liposomal doxorubicin), Doxil (PEGylated liposomal doxorubicin), Abraxane (albumin-based pacitaxel) and Genexol-PM (paclitaxel-containing polymeric micelles; pre-approved in Korea) [12]. Currently several additional passively tumor-targeted nanomedicines are in clinical trials and many more in early- and late-stage preclinical development [12, 20].

*Active targeting to cancer cells*

As opposed to passive drug targeting, active drug targeting involves the use of targeting ligands to direct the binding of nanomaterials to receptor (over-) expressed at the target site [21]. Notably, active drug targeting is generally implemented not to improve overall tumor accumulation, as it relies solely on passive distribution via EPR effect, but to improve target cell recognition and target cell uptake, which is postulated to improve the therapeutic efficacy as compared with nontargeted nanoparticles. While the potential benefit of active targeting nanoparticles seems to be widely accepted, to date only antibody-based nanomedicines, such as Zevalin, Mylotarg, Ontak and Bexxar have been approved for clinical use but none of actively targeted liposomes, polymers, micelles and nanoparticles have thus far been approved for clinical use, and only very few are in clinical trials [12]. The very reason that actively targeted 'classical' nanomedicines, e.g. liposomes, polymers and micelles, have thus far largely failed to demonstrate benefit at the (pre-) clinical level is mostly attributed to the fact that after leaving the highly leaky tumor vasculature, there are quite a number of anatomical and physiological barriers that need to be overcome before antibody- or peptide-targeted formulations can bind to (and enter) cancer cells. These include the presence of several biological cell barriers between endothelial and tumor cells including

pericyte-, smooth muscle cell- and fibroblast-based cell layers, the high cellular density within solid malignancies, and the high interstitial fluid pressure that is a typical characteristic of tumors [20, 22]. Moreover, the binding-site barrier further limits the penetration of actively targeted nanomedicines into the tumor interstitium [23]. Therefore, actively targeted nanomedicines potentially tend to have problems finding their target cells, and they sometimes fail to demonstrate an advantage over passively targeted formulations.

*Active targeting to endothelial cells*

The major shortcoming in both passive and active targeting to tumor cells has been identified in several studies over the years [13, 17, 20, 24-27]. It is related to the poor penetration of nanomedicines through interstitial and tumor tissue due to a variety of biological barriers, including pericyte-based, smooth muscle cell-based, and fibroblast- based cell layers between endothelial and cancer cells, as well as a plethora of cellular processes and anatomic tumor issues (i.e., the high cellular density within solid tumors, high interstitial fluid pressure, and heterogeneous EPR effect dramatically varying from tumor to tumor and from patient to patient [20]). To address these issues, a variety of vascular-targeted nanoformulations have been designed and evaluated [12, 13, 24, 27]. Example of angiogenic endothelium targeting are 1) the antibody fragment L19 against extra-domain B domain of the oncofetal protein fibronectin highly up-regulated on angiogenic vasculature, 2) the natural sLex ligand binding to E- and P-selectin, inflammation markers [28], 3) the peptide termed VP for Vascular cell adhesion protein-1 expressed in inflamed tissue [29, 30] 4) the several linear and cyclic derivatives of the oligopeptides containing the Arg-Gly-Asp (RGD) sequence, which binds to integrins on angiogenic endothelium [31-33]. Tumor vasculature-

targeting nanomedicines do not depend on extravasation and penetration across several biological cell barriers as well as the high tumor cell density and the high interstitial fluid pressure, mentioned earlier, in order to reach the target cancer cells. In addition, they recognize their target receptors much more easily and frequently than do cancer cell-targeting nanomedicines. Thus, it is anticipated that endothelial cell-targeting nanomedicines could offer another highly potential strategy for improving antitumor efficacy [12, 17]. Moreover, therapeutic disrupting tumor vasculature does not only deprive tumors of oxygen and nutrients but also enhance EPR effect due to increased vasculature leakiness. Along with the potential design to release therapeutic contents within the tumor vasculature upon binding, enabling low-molecular-weight drugs to penetrate deep into the tumor interstitium, this vasculature-targeting nanomedicines can significantly provide extra benefits for therapeutic treatment. Furthermore, the recent strategy against cancer is normalizing the tumor microenvironment. For instance, vascular normalization, involves correction of excessive angiogenesis signaling to repair abnormalities in vascular structure and function [35]. Vascular normalizing therapies include anti-angiogenics, reducing interstitial fluid pressure [34] and increasing perfusion [36]. Rationally, active targeting to endothelial cell strategies can be implemented for the success of vascular normalization leading to improvement of nanomedicine supply to tumors as well as increase of their effective permeability [37]. Intriguingly, the vasculature normalization may be combined with other conventional strategies for a pronounced improvement in nanomedicine delivery, distribution and efficacy.

*Triggered drug delivery*

Another targeting strategy capable of generating innovative nanoformulations focuses on the possibility that a nanosystem can be triggered to release their contents upon exposure to external stimuli, such as light, heat, ultrasound, and magnetic fields. An example of such stimuli-responsive nanomedicines that hold significant clinical potential is Thermodox, a temperature-sensitive doxorubicin-PEGylated liposomes. It is designed to release the conjugated chemotherapeutic drug only upon applying regionally confined triggers, either upon EPR-mediated passive tumor accumulation, or already during circulation, thereby maximizing drug release at the pathological site, while preventing damage to potentially endangered healthy tissues [38]. Despite the clinical potential of such nanoformulations, there are still several important limitations to their rapid clinical development, which include manufacturing difficulties and problems with stimuli- responsiveness and the stability of the controlled-release nanomaterials [12]. To overcome these shortcomings and to develop more effective nanoparticles for triggered drug delivery, more effort is being undertaken, both at the academic and at the industrial level.

**Commonly used biologics and nanoparticles in cancer therapy**

Since the discovery in 1948 that cytotoxic folate antimetabolites could be used in the treatment of childhood leukemia, our basic approach to cancer therapy has remained fundamentally the same: surgery followed by sublethal administration of various cytotoxic compounds or radiation [39]. In many cases, conventional treatments for cancer have clinical success, but they also have limitations. Surgery and radiotherapy are effective for the treatment of localized tumors, but they may not be useful for disseminated disease or for

tumors located in areas that are difficult or dangerous to reach [40]. Traditional chemotherapy can be severely toxic to normal tissue and also could not provide enough therapeutic doses. It flags the need of new and better treatment regimes utilizing novel rationales, methodologies as well as therapeutic modalities. Not until 1982 the first biotechnology-derived product (biologic) approved for therapeutic use was biosynthetic "human" insulin made by recombinant DNA technology. Since then biologics hold a great deal of promise among the therapeutic interventions for a wide range of disorders, including cancer and inflammatory diseases. Millions of people worldwide have benefited from hundreds biologic products and vaccines available today [41, 42]. Although the first biologic was approved in the early 1980s, the use of these agents in the treatment of cancer is still relatively new [43].

Biologics differ from traditional pharmaceutical drugs. They are typically larger and more complex molecules than chemical drugs. Biologics include: (1) naturally occurring or modified biologic compounds such as vaccines, hormone extracts, and blood products; (2) recombinant proteins or peptides; (3) monoclonal antibodies and fusion proteins; and (4) antisense oligonucleotides to nucleic acids [44]. Among a wide range of biologic products, albumin is of great interest as a versatile protein carrier for drug targeting and for improving the pharmacokinetic profile of peptide- or protein-based drugs. Albumin is the most abundant plasma protein (35–50 g/L human serum) with a molecular weight of 66.5 kDa. Albumin exhibits very long half-life, extremely robust: it is stable in the pH range of 4–9, soluble in 40% ethanol, and can be heated at 60 °C for up to 10 h without deleterious effects. These properties as well as its preferential accumulation in solid tumors [45-48] and inflamed tissue [49-51], its ready availability, its biodegradability, and its lack of toxicity and

immunogenicity make it an ideal candidate for drug delivery. Clinically, a methotrexate-albumin conjugate, an albumin-binding prodrug of doxorubicin, i.e. the (6-maleimido) caproylhydrazone derivative of doxorubicin (DOXO-EMCH), and an albumin paclitaxel nanoparticle (Abraxane) have been evaluated clinically. Several albumin-based market products have been approved Levemir® and Victoza® (antidiabetic product), Abraxane® (anti non-small cell lung cancer, breast cancer and metastatic pancreatic cancer product) [52], and Nanocoll® and Albures® (for lymphoscintigraphy and diagnosis of cancer and rheumatoid arthritis) [53]. Along with albumin, streptavin is playing an increasing role as a drug carrier in the clinical setting [54-58] due to its comparable benefit properties to albumin plus its uniquely ultra-high affinity to biotin characteristic. This characteristic offers markedly convenience for further carrier modification (e.g. drug, peptide, protein, nucleic acid-conjugation), as it does not require any conjugation chemistry. Recently over the past years since the first FDA-approved therapeutic monoclonal antibody in 1986 for transplant rejection prevention [59, 60] and in 1997 the first antibody for cancer treatment was approved [59], monoclonal antibodies have entered the mainstream of cancer therapy. Their first use was as antagonists of oncogenic receptor tyrosine kinases, but today monoclonal antibodies have emerged as long-sought vehicles for the targeted delivery of potent chemotherapeutic agents and as powerful tools to manipulate anticancer immune responses[39]. In 2007, eight of the 20 best-selling biotechnology drugs in the U.S. are therapeutic monoclonal antibodies [61]. Currently, there are 13 antibodies approved by the FDA for various oncology indications, and many more are currently being evaluated in clinical trials [39]. Antibodies may be used in their native state or as fragments. Commonly well established antibody fragments include antigen-binding fragments (Fab), dimers of

antigen-binding fragments ((Fab′)2), and single-chain fragment variables (scFv). There are, as well, several engineered fragments that would require further gene modification or conjugation procedures, e.g., scFv-crystallizable fragment (Fc), diabody, triabody.

In addition to antibodies, aptamers, which are short single-stranded DNA or RNA, are another promising targeting agent and currently are in active research studies. As an example of aptamer use, docetaxel (Dtxl)-encapsulated nanoparticles are surfacely modified with a targeting aptamer to the antigen on the surface of prostate cancer cells. The system demonstrated high selectivity and efficacy in vivo [62]. Growth factor or vitamin interactions with cancer cells also offering additional strategy to target cancer cells. Epidermal growth factor (EGF) and vitamin folic acid (folate) are examples of growth factor and vitamin that have been used for cancer targeting [63].

While, biologics have widely been accepted for cancer treatment, a new strategy emerges hoping for improving therapeutic efficiency. This strategy utilizes a wide range of engineered materials and formulations to generate sophisticated nanoscaffolds for drug delivery. Generally these nanocarriers are in the size of 1–100 nm in diameter. They generally offer abilities to carry multiple drugs and/or imaging agents and to release drugs in controllable or triggerable manner. The current nanocarriers used as drug delivery vectors include polymer conjugates, polymeric nanoparticles, lipid-based carriers such as liposomes and micelles, dendrimers, carbon nanotubes, silica oxides, metal oxides, quantum dots and gold nanoparticles. These nanocarriers have been explored for a variety of applications such as drug delivery, imaging, photothermal ablation of tumours, radiation sensitizers, detection of apoptosis, and sentinel lymphnode mapping [17, 64-67]. Although these materials are likely to provide several advantages, their utilization in biomedicine is, to certain extent,

limited. To translate the developed nanomedicines into clinical practice successfully, several issues still needed to be addressed, including a favorable blood half- life and physiologic behavior with minimal off-target effects, effective clearance from the human organism, minimal or no toxicity to healthy tissues in living organisms, potentials to commercially scale-up [12, 63, 68].

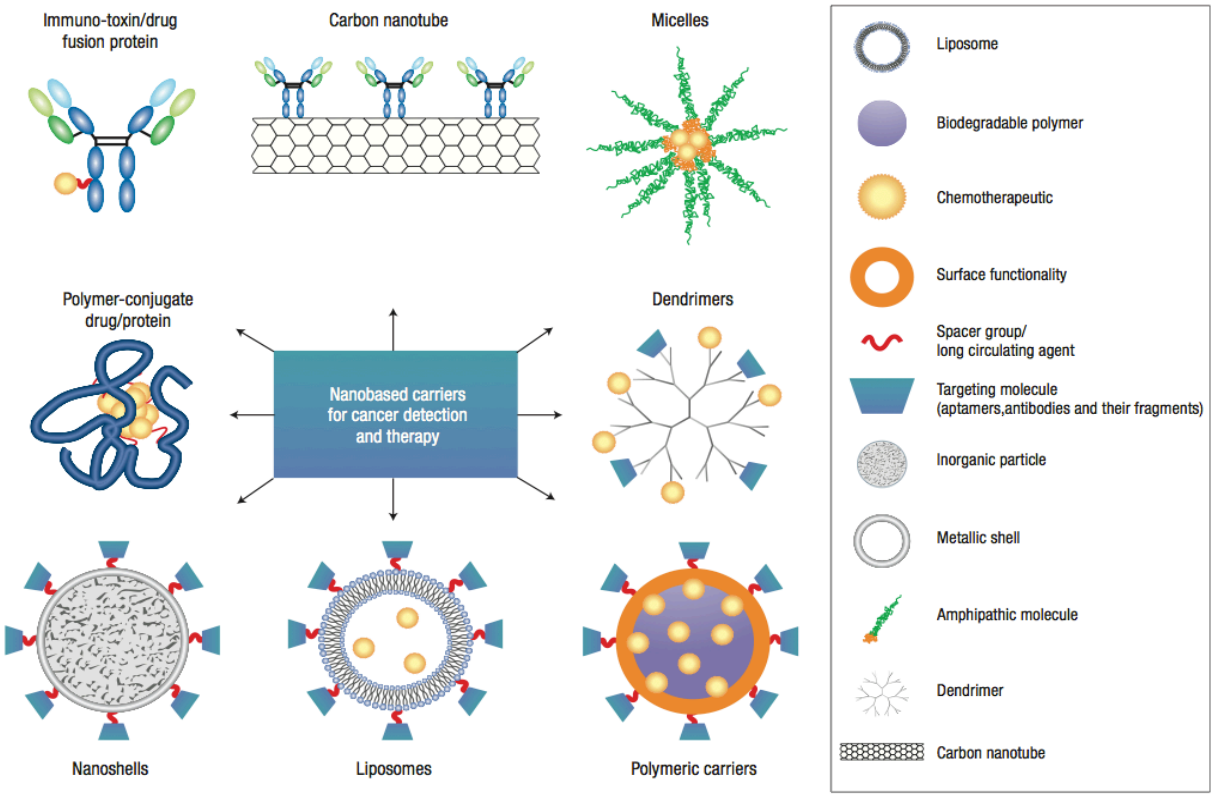


**Figure 3.** Examples of nanocarriers for targeting cancer. A wide range of nanomaterials can be implemented for cancer intervention. However, the three main components, a carrier, a targeting moiety, and a cargo, e.g. therapeutic drugs, are generally preserved. Figure reproduced from [63].

**Table 2.** Representative examples of nanocarrier-based drugs on the market. Table reproduced from [63]

| Representative examples of nanocarrier-based drugs on the market | | | |
|---|---|---|---|
| Compound | Commercial name | Nanocarrier | Indications |
| Styrene maleic anhydride-neocarzinostatin (SManCS) | Zinostatin/Stimalmer | Polymer–protein conjugate | Hepatocellular carcinoma |
| Peg-l-asparaginase | Oncaspar | Polymer–protein conjugate | Acute lymphoblastic leukemia |
| Peg-granulocyte colony-stimulating factor (g-CSf) | Neulasta/Pegfilgrastim | Polymer–protein conjugate | Prevention of chemotherapy-associated neutropenia |
| IL2 fused to diphtheria toxin | Ontak (Denilelukin diftitox) | Immunotoxin (fusion protein) | Cutaneous t-cell lymphoma |
| Anti-CD33 antibody conjugated to calicheamicin | Mylotarg | Chemo-immunoconjugate | Acute myelogenous leukemia |
| Anti-CD20 conjugated to yttrium-90 or indium-111 | Zevalin | Radio-immunoconjugate | Relapsed or refractory, low-grade, follicular, or transformed non-Hodgkin's lymphoma |
| Anti-CD20 conjugated to iodine-131 | Bexxar | Radio-immunoconjugate | Relapsed or refractory, low-grade, follicular, or transformed non-Hodgkin's lymphoma |
| Daunorubicin | DaunoXome | Liposomes | Kaposi's sarcoma |
| Doxorubicin | Myocet | Liposomes | Combinational therapy |

| | | | |
|---|---|---|---|
| | | | of recurrent breast cancer, ovarian cancer, Kaposi's sarcoma |
| Doxorubicin | Doxil/Caelyx | PEG-liposomes | Refractory Kaposi's sarcoma, recurrent breast cancer, ovarian cancer |
| Vincristine | Onco TCS | Liposomes | Relapsed aggressive non-Hodgkin's lymphoma (nHl) |
| Paclitaxel | Abraxane | Albumin-bound paclitaxel nanoparticles | Metastatic breast cancer |

**Pharmacokinetics**

Pharmacokinetics is defined as the study of the time course of drug absorption, distribution, metabolism, and excretion. Clinical pharmacokinetics is the application of pharmacokinetic principles to the safe and effective therapeutic management of drugs in an individual patient. Primary goals of clinical pharmacokinetics include enhancing efficacy and decreasing toxicity of a patient's drug therapy. A drug's effect is often related to its concentration at the site of action, so it would be useful to monitor this concentration. However, direct measurement of drug concentration at the sites of action i.e. receptor sites is generally not practical as we cannot directly sample drug concentration in the tissue, instead we can measure the concentration in easily sampled fluids, e.g. blood, plasma, urine, and saliva. To predict the relationship between plasma drug concentration and concentration at the receptor site, Kinetic homogeneity concept was assumed. It is the assumption that

concentrations of a drug in plasma is directly relate to concentrations at the receptor site, where a given drug produces its therapeutic effect, as well as in other tissues. As the concentration of drug in plasma increases, the concentration of drug in most tissues will proportionally increase and vice versa.

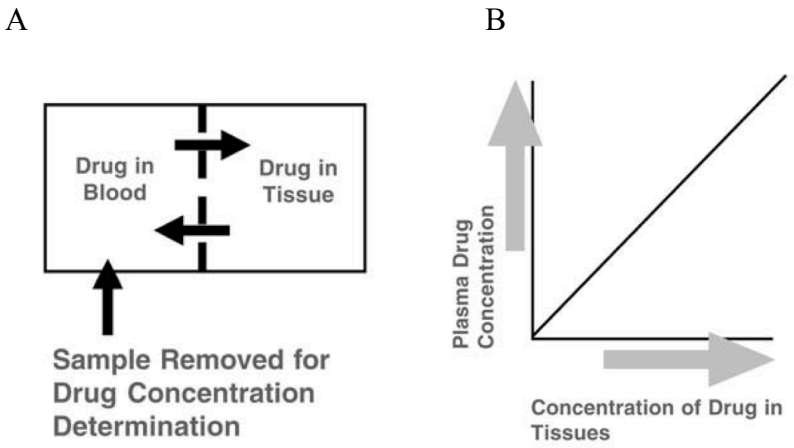


**Figure 4.** Kinetic homogeneity. (A) Schematic diagram represent kinetic homogeneity concept (B) a relationship of plasma to tissue drug concentrations. Figure reproduced from [69].

*Pharmacokinetic models*

Administrated drug into the body undergoes several biological processes, such as absorption, distribution, metabolism, and elimination, which pose difficulty to predict a drug's behavior in the body and to identify drug concentration in target tissues. In order to study the drug's behavior, various body processes need to be simplified utilizing mathematical models. Compartmental models, the basic and widely used models in pharmacokinetics, are categorized by the number of compartments needed to describe the drug's behavior in the body. The compartments generally represent a group of organs or

tissues in which drug distribution is similar instead of each individual specific organ or tissue.

For example, heart, lungs, liver and kidneys, which are often similar and highly blood-perfused, are considered as one compartment, and is usually referred to as the central compartment. On the other hand, fat tissue, muscle tissue, and cerebrospinal fluid, which are less well perfused, are designated as the other compartment, known as the peripheral compartment. Figure demonstrates organs groups for central and peripheral compartments.

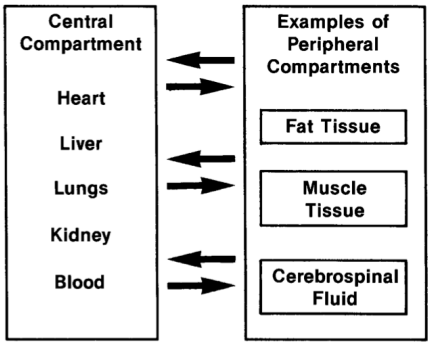


**Figure 5.** Typical organ groups for central and peripheral compartments. Figure reproduced from [69].

Compartmental models are deterministic because the observed drug concentrations determine the type of compartmental model required to describe the pharmacokinetics of the drug. Generally, it is best to use the simplest model that accurately predicts changes in drug concentrations over time. If a one-compartment model is sufficient to predict plasma drug concentrations (and those concentrations are of most interest to us), then a more complex (two-compartment or more) model is not necessary.

- One-compartment model

The one-compartment model is the simplest because there is only one compartment. All body tissues and fluids are considered a part of this compartment. Furthermore, it is assumed that after a dose of drug is administered, it distributes instantaneously to all body areas [70]. Thus the drug concentration–time profile shows a monophasic response (i.e. it is monoexponential) and the log drug concentration-time graph shows a liner relation. It is important to note that this does not imply that the drug concentration in plasma is equal to the drug concentration in the tissues. However, changes in the plasma concentration quantitatively reflect changes in the tissues [70].

- Two-compartment model

However, some drugs do not distribute instantaneously to all parts of the body, even after intravenous bolus administration. Commonly, the drug distributes rapidly in the bloodstream and in highly perfused organs, and then slowly disperses to other body tissues. This pattern of drug distribution is represented by two-compartment model [70]. The drug concentration–time profile of this model shows a curve but the log drug concentration–time plot shows a biphasic response and this can be used to distinguish whether a drug shows a one- or two-compartment model [70].

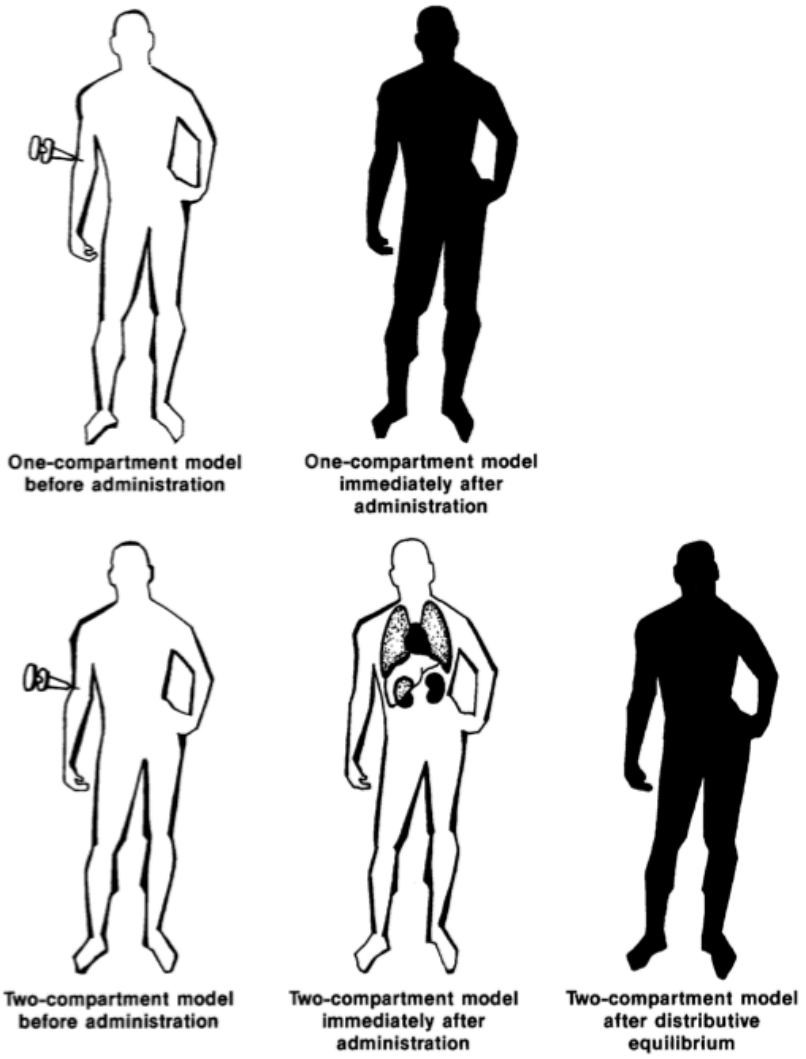


**Figure 6.** Drug distribution in one- and two-compartment models. Figure reproduced from [69].

The one- and two- compartment model can be represented as in Figure 7. Notably, in two-compartment model, drug moves back and forth between these compartments to maintain equilibrium.

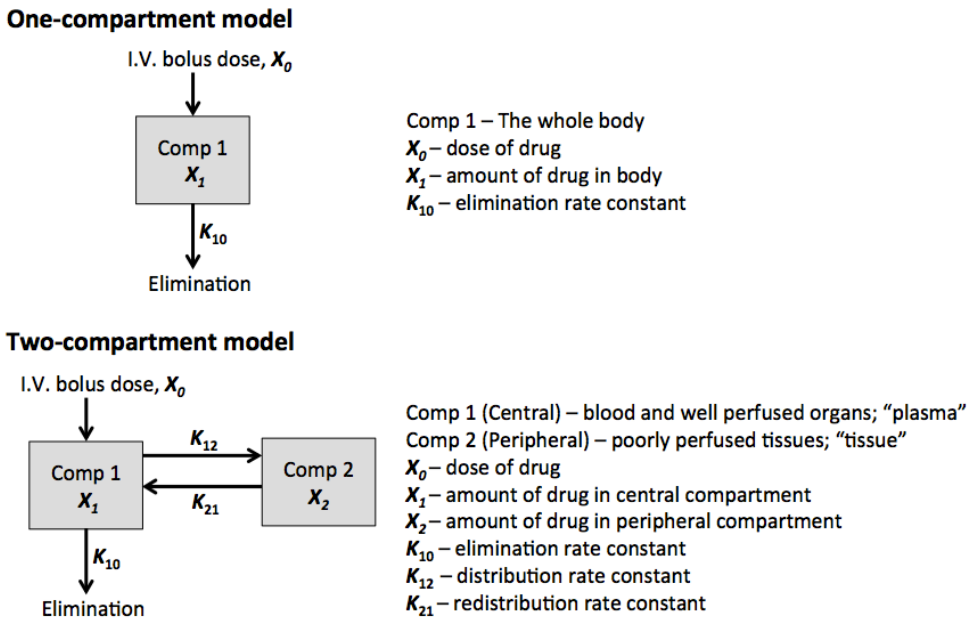


**Figure 7.** One- and two- compartment models. Figure is modified and reproduced from [69-71]

- Multi-compartment model

When the concentration–time profile shows more than two exponentials, it indicates the drug distributes into more than two compartments. In this case, multi-compartment model is required to explain drug's behavior in the body and each exponential on the concentration–time profile describes a compartment. Gentamicin is an example of drug, described by a three-compartment model following a single I.V. dose [70].

*Pharmacokinetic parameters*

This section briefly review the terminology frequently used in pharmacokinetic study.

- Volume of distribution

Volume of distribution (Vd) is an important indicator of the extent of drug distribution into body fluids and tissues. It is defined as the volume of plasma in which the total amount of drug in the body would be required to be dissolved in order to reflect the drug concentration attained in plasma [70]. The volume of distribution actually has no direct physiological meaning and it is usually referred to as the apparent volume of distribution.

A large volume of distribution indicates that the drug distributes extensively into body tissues and fluids. Conversely, a small volume of distribution indicates limited drug distribution in tissues, but mainly in the plasma. When Vd is many times the volume of the body, the drug concentrations in some tissues should be much greater than those in plasma. The smallest volume in which a drug may distribute is the total plasma volume [69].

- Distribution and elimination phase

When drug plasma concentration-time plot after intravenous injection is shown as a semi-logarithmic plot, two different phases can be distinguished; an initial phase during which the plasma concentration steeply decreases i.e. distribution phase, and a second, linear phase which is less steep i.e. elimination phase. During the distribution phase, rapid changes in the concentration of drug in plasma reflect primarily distribution of drug into the different tissues within the body, rather than loss from the body. Once the drug in the plasma and tissues has reached equilibrium, during the linear phase in the semi-logarithmic plot, the decline of plasma concentration is driven by elimination of the drug from the body [72].

- Elimination half-life

Elimination half-life or terminal half-life is the time required for drug concentration in the blood to decrease by 50% after pseudo-equilibrium of distribution has been reached; then, terminal half-life is computed when the decrease in drug plasma concentration is due only to

drug elimination. It is important to note that elimination half-life is not the time necessary for the amount of the administered drug to fall by one half [71]. However, for one-compartment model, elimination half-life is simply referred to the time required to reduce the plasma concentration to one half its initial administrated value [70].

- Clearance

Drug clearance (CL) is defined as the volume of plasma in the vascular compartment cleared of drug per unit time. This drug elimination generally results from liver metabolism and/or excretion by the kidneys [72]. Clearance for a drug is constant if the drug is eliminated by first-order kinetics. If a drug has a CL of 3L/h, this tells you that 3 litres of the Vd is cleared of drug per hour [70].

- Area under the curve

The area under curve (AUC) is integral of the plasma drug concentration-time curve. It reflects the actual body exposure to drug after administration of a dose of the drug and is expressed in mg*h/L [72]. This area under the curve is dependent on the rate of elimination of the drug from the body and the dose administered.

- Mean residence time

Mean residence time (MRT) is the average time the molecule introduced reside within the body [73]. MRT value helps interpret the duration of effect for direct-acting molecules.

**Biodistribution**

Biodistribution is a study of tracking where agents, e.g., compounds, nanoparticles, cells, of interest travel in an experimental animal or human subject. The agents usually are

modified to contain some tractable moieties, e.g. fluorescent dyes, radioisotopes, or genes encoding specific reporter proteins like luciferase and green fluorescent protein. The biodistribution study can be performed both non-invasive and invasive manners. Non-invasive strategy generally refers to imaging of the tracked agents in real time in live animal models. The non-invasive method has gained popularity since 1) the tracking can be performed over time on the same animal, providing more and conclusive information with minimized variation errors, 2) the strategy offers a way to reduce the number of animals used, and 3) a wide range of suitable imaging techniques has become available for research use. The examples of imaging modalities used for biodistribuion study include bioluminescence imaging, fluorescence imaging, Magnetic resonance imaging (MRI), positron emission tomography (PET), single-photon emission computed tomography (SPECT).

Regarding invasive biodistribution study, it is usually involved in euthanizating the experimental animals at terminated time point, and collecting organs or tissues of interest for further analysis of the tracking agent. An example of general procedure, once tested compound is injected intravenously into a group of 16-20 mice, at intervals of 1, 2, 4, and 24 hours, smaller groups (4-5) of the animals are euthanized, and then dissected. The organs of interest (usually; blood, liver, spleen, kidney, muscle, fat, adrenals, pancreas, brain, bone, stomach, small intestine, and upper and lower large intestine) are harvested and analyzed to identify the amount of administrated compounds in each individual tissue. The results give a dynamic view of how the compound moves through the animal. The imaging techniques mention earlier as well as many other conventional laboratory techniques, e.g. immunohistochemical methods, fluorescent/luminescence microplate reader assay and

Polymerase chain reaction (PCR), can be implemented to determine the amount of tracking compounds presenting in the tissues.

# REFERENCES


1. Hanahan, D. and R.A. Weinberg, Hallmarks of cancer: the next generation. Cell, 2011. 144(5): p. 646-74.
2. Kinzler, K.W. and B. Vogelstein, Lessons from hereditary colorectal cancer. Cell, 1996. 87(2): p. 159-70.
3. Coussens, L.M. and Z. Werb, Inflammation and cancer. Nature, 2002. 420(6917): p. 860-7.
4. Rakoff-Nahoum, S., Why cancer and inflammation? The Yale journal of biology and medicine, 2006. 79(3-4): p. 123-30.
5. Coffelt, S.B. and K.E. de Visser, Cancer: Inflammation lights the way to metastasis. Nature, 2014. 507(7490): p. 48-9.
6. Balkwill, F. and A. Mantovani, Inflammation and cancer: back to Virchow? Lancet, 2001. 357(9255): p. 539-45.
7. Strebhardt, K. and A. Ullrich, Paul Ehrlich's magic bullet concept: 100 years of progress. Nature reviews. Cancer, 2008. 8(6): p. 473-80.
8. Jain, R.K., Transport of molecules, particles, and cells in solid tumors. Annual review of biomedical engineering, 1999. 1: p. 241-63.
9. Chauhan, V.P. and R.K. Jain, Strategies for advancing cancer nanomedicine. Nature materials, 2013. 12(11): p. 958-62.
10. Owens, D.E., 3rd and N.A. Peppas, Opsonization, biodistribution, and pharmacokinetics of polymeric nanoparticles. International journal of pharmaceutics, 2006. 307(1): p. 93-102.
11. Aggarwal, P., et al., Nanoparticle interaction with plasma proteins as it relates to particle biodistribution, biocompatibility and therapeutic efficacy. Advanced drug delivery reviews, 2009. 61(6): p. 428-37.
12. Lammers, T., et al., Drug targeting to tumors: principles, pitfalls and (pre-) clinical progress. Journal of controlled release : official journal of the Controlled Release Society, 2012. 161(2): p. 175-87.

13. Farokhzad, O.C. and R. Langer, Impact of nanotechnology on drug delivery. ACS nano, 2009. 3(1): p. 16-20.
14. Davis, M.E., Z.G. Chen, and D.M. Shin, Nanoparticle therapeutics: an emerging treatment modality for cancer. Nature reviews. Drug discovery, 2008. 7(9): p. 771-82.
15. Nicolas, J., et al., Design, functionalization strategies and biomedical applications of targeted biodegradable/biocompatible polymer-based nanocarriers for drug delivery. Chemical Society reviews, 2013. 42(3): p. 1147-235.
16. Kamaly, N., et al., Targeted polymeric therapeutic nanoparticles: design, development and clinical translation. Chemical Society reviews, 2012. 41(7): p. 2971-3010.
17. Sanna, V., N. Pala, and M. Sechi, Targeted therapy using nanotechnology: focus on cancer. International journal of nanomedicine, 2014. 9: p. 467-83.
18. Choi, H.S., et al., Renal clearance of quantum dots. Nature biotechnology, 2007. 25(10): p. 1165-70.
19. Schmidt, M.M. and K.D. Wittrup, A modeling analysis of the effects of molecular size and binding affinity on tumor targeting. Molecular cancer therapeutics, 2009. 8(10): p. 2861-71.
20. Jain, R.K. and T. Stylianopoulos, Delivering nanomedicine to solid tumors. Nature reviews. Clinical oncology, 2010. 7(11): p. 653-64.
21. Marcucci, F. and F. Lefoulon, Active targeting with particulate drug carriers in tumor therapy: fundamentals and recent progress. Drug discovery today, 2004. 9(5): p. 219-28.
22. Heldin, C.H., et al., High interstitial fluid pressure - an obstacle in cancer therapy. Nature reviews. Cancer, 2004. 4(10): p. 806-13.
23. Juweid, M., et al., Micropharmacology of monoclonal antibodies in solid tumors: direct experimental evidence for a binding site barrier. Cancer research, 1992. 52(19): p. 5144-53.
24. Elsabahy, M. and K.L. Wooley, Design of polymeric nanoparticles for biomedical delivery applications. Chemical Society reviews, 2012. 41(7): p. 2545-61.
25. Riehemann, K., et al., Nanomedicine--challenge and perspectives. Angewandte Chemie, 2009. 48(5): p. 872-97.

26. Gautier, J., et al., Design strategies of hybrid metallic nanoparticles for theragnostic applications. Nanotechnology, 2013. 24(43): p. 432002.
27. Petros, R.A. and J.M. DeSimone, Strategies in the design of nanoparticles for therapeutic applications. Nature reviews. Drug discovery, 2010. 9(8): p. 615-27.
28. van Kasteren, S.I., et al., Glyconanoparticles allow pre-symptomatic in vivo imaging of brain disease. Proceedings of the National Academy of Sciences of the United States of America, 2009. 106(1): p. 18-23.
29. Kelly, K.A., et al., Detection of vascular adhesion molecule-1 expression using a novel multimodal nanoparticle. Circulation research, 2005. 96(3): p. 327-36.
30. Frechou, M., et al., Detection of vascular cell adhesion molecule-1 expression with USPIO-enhanced molecular MRI in a mouse model of cerebral ischemia. Contrast media & molecular imaging, 2013. 8(2): p. 157-64.
31. Koning, G.A., et al., Targeting of angiogenic endothelial cells at sites of inflammation by dexamethasone phosphate-containing RGD peptide liposomes inhibits experimental arthritis. Arthritis and rheumatism, 2006. 54(4): p. 1198-208.
32. Temming, K., et al., RGD-based strategies for selective delivery of therapeutics and imaging agents to the tumour vasculature. Drug resistance updates : reviews and commentaries in antimicrobial and anticancer chemotherapy, 2005. 8(6): p. 381-402.
33. Mitra, A., et al., Targeting tumor angiogenic vasculature using polymer-RGD conjugates. Journal of controlled release : official journal of the Controlled Release Society, 2005. 102(1): p. 191-201.
34. Jain, R.K., Normalizing tumor microenvironment to treat cancer: bench to bedside to biomarkers. Journal of clinical oncology : official journal of the American Society of Clinical Oncology, 2013. 31(17): p. 2205-18.
35. Goel, S., et al., Normalization of the vasculature for treatment of cancer and other diseases. Physiological reviews, 2011. 91(3): p. 1071-121.
36. Batchelor, T.T., et al., Improved tumor oxygenation and survival in glioblastoma patients who show increased blood perfusion after cediranib and chemoradiation. Proceedings of the National Academy of Sciences of the United States of America, 2013. 110(47): p. 19059-64.

37. Chauhan, V.P., et al., Normalization of tumour blood vessels improves the delivery of nanomedicines in a size-dependent manner. Nature nanotechnology, 2012. 7(6): p. 383-8.
38. Tagami, T., M.J. Ernsting, and S.D. Li, Efficient tumor regression by a single and low dose treatment with a novel and enhanced formulation of thermosensitive liposomal doxorubicin. Journal of controlled release : official journal of the Controlled Release Society, 2011. 152(2): p. 303-9.
39. Sliwkowski, M.X. and I. Mellman, Antibody therapeutics in cancer. Science, 2013. 341(6151): p. 1192-8.
40. Boyle, R.M., The Use of Biologics in Cancer Therapy. US Pharmacist, 2010. 35(3): p. (Oncology suppl):4-7.
41. Shankar, G., et al., Scientific and regulatory considerations on the immunogenicity of biologics. Trends in biotechnology, 2006. 24(6): p. 274-80.
42. U.S. Food and Drug Administration. Biological Approvals by Year. 2013 [cited 2013 December 17]; Available from: http://www.fda.gov/BiologicsBloodVaccines/DevelopmentApprovalProcess/BiologicalApprovalsbyYear/default.htm.
43. Freeman, C.P., et al., Utilization of Anticancer Biologic Products Among Medicare Beneficiaries, By Diagnostic Cancer Subchapter, 2006-2009: Data Points #7, in Data Points Publication Series2011: Rockville (MD).
44. Sandborn, W.J. and W.A. Faubion, Biologics in inflammatory bowel disease: how much progress have we made? Gut, 2004. 53(9): p. 1366-73.
45. Desai, N., et al., Increased antitumor activity, intratumor paclitaxel concentrations, and endothelial cell transport of cremophor-free, albumin-bound paclitaxel, ABI-007, compared with cremophor-based paclitaxel. Clinical cancer research : an official journal of the American Association for Cancer Research, 2006. 12(4): p. 1317-24.
46. Kratz, F., Albumin as a drug carrier: design of prodrugs, drug conjugates and nanoparticles. Journal of controlled release : official journal of the Controlled Release Society, 2008. 132(3): p. 171-83.

47. Kim, T.H., et al., Preparation and characterization of water-soluble albumin-bound curcumin nanoparticles with improved antitumor activity. International journal of pharmaceutics, 2011. 403(1-2): p. 285-91.
48. Elzoghby, A.O., W.M. Samy, and N.A. Elgindy, Albumin-based nanoparticles as potential controlled release drug delivery systems. Journal of controlled release : official journal of the Controlled Release Society, 2012. 157(2): p. 168-82.
49. Niwa, Y., et al., Serum albumin metabolism in rheumatic diseases: relationship to corticosteroids and peptic ulcer. Journal of clinical & laboratory immunology, 1990. 31(1): p. 11-6.
50. Ballantyne, F.C., A. Fleck, and W.C. Dick, Albumin metabolism in rheumatoid arthritis. Annals of the rheumatic diseases, 1971. 30(3): p. 265-70.
51. Wilkinson, P., et al., The Mechanism of Hypoalbuminemia in Rheumatoid Arthritis. Annals of internal medicine, 1965. 63: p. 109-14.
52. Pazdur, R. FDA Approval for Paclitaxel Albumin-stabilized Nanoparticle Formulation. 2013 [cited 2013 December 18]; Available from: http://www.cancer.gov/cancertopics/druginfo/fda-nanoparticle-paclitaxel.
53. Sethi, A., et al., Albumin as a drug delivery and diagnostic tool and its market approved products. Acta poloniae pharmaceutica, 2013. 70(4): p. 597-600.
54. Knox, S.J., et al., Phase II trial of yttrium-90-DOTA-biotin pretargeted by NR-LU-10 antibody/streptavidin in patients with metastatic colon cancer. Clinical cancer research : an official journal of the American Association for Cancer Research, 2000. 6(2): p. 406-14.
55. Lazzeri, E., et al., Clinical feasibility of two-step streptavidin/111In-biotin scintigraphy in patients with suspected vertebral osteomyelitis. European journal of nuclear medicine and molecular imaging, 2004. 31(11): p. 1505-11.
56. Forero, A., et al., Phase 1 trial of a novel anti-CD20 fusion protein in pretargeted radioimmunotherapy for B-cell non-Hodgkin lymphoma. Blood, 2004. 104(1): p. 227-36.
57. Kalofonos, H.P., et al., Imaging of tumor in patients with indium-111-labeled biotin and streptavidin-conjugated antibodies: preliminary communication. Journal of

nuclear medicine : official publication, Society of Nuclear Medicine, 1990. 31(11): p. 1791-6.

58. Shen, S., et al., Patient-specific dosimetry of pretargeted radioimmunotherapy using CC49 fusion protein in patients with gastrointestinal malignancies. Journal of nuclear medicine : official publication, Society of Nuclear Medicine, 2005. 46(4): p. 642-51.
59. Waldmann, T.A., Immunotherapy: past, present and future. Nature medicine, 2003. 9(3): p. 269-77.
60. Hooks, M.A., C.S. Wade, and W.J. Millikan, Jr., Muromonab CD-3: a review of its pharmacology, pharmacokinetics, and clinical use in transplantation. Pharmacotherapy, 1991. 11(1): p. 26-37.
61. Scolnik, P.A., mAbs: a business perspective. mAbs, 2009. 1(2): p. 179-84.
62. Farokhzad, O.C., et al., Targeted nanoparticle-aptamer bioconjugates for cancer chemotherapy in vivo. Proceedings of the National Academy of Sciences of the United States of America, 2006. 103(16): p. 6315-20.
63. Peer, D., et al., Nanocarriers as an emerging platform for cancer therapy. Nature nanotechnology, 2007. 2(12): p. 751-60.
64. Duncan, R., Polymer conjugates as anticancer nanomedicines. Nature reviews. Cancer, 2006. 6(9): p. 688-701.
65. Ferrari, M., Cancer nanotechnology: opportunities and challenges. Nature reviews. Cancer, 2005. 5(3): p. 161-71.
66. Couvreur, P. and C. Vauthier, Nanotechnology: intelligent design to treat complex disease. Pharmaceutical research, 2006. 23(7): p. 1417-50.
67. Alonso, M.J., Nanomedicines for overcoming biological barriers. Biomedicine & pharmacotherapy = Biomedecine & pharmacotherapie, 2004. 58(3): p. 168-72.
68. Walkey, C.D. and W.C. Chan, Understanding and controlling the interaction of nanomaterials with proteins in a physiological environment. Chemical Society reviews, 2012. 41(7): p. 2780-99.
69. Concepts in clinical pharmacokinetics, 4th ed, in Scitech Book News2006, Ringgold Inc: Portland.
70. Mauro, L.S., Clinical Pharmacokinetics: Edited by Soraya Dhillon BPharm PhD MRPharmS and Andrzej Kostrzewski BSc MSc MMedEd MRPharmS ILTM.

Published by the Pharmaceutical Press, Grayslake, IL, 2006. ISBN 0-85369-571-7. Paperbound, xvii + 262 pp. (23.5 x 15.5 cm), $59.95. http://www.pharmpress.com. Annals of Pharmacotherapy Annals of Pharmacotherapy, 2006. 40(10): p. 1893.

71. Toutain, P.L. and A. Bousquet-Melou, Plasma terminal half-life. Journal of veterinary pharmacology and therapeutics, 2004. 27(6): p. 427-39.

72. T., B., et al. Pharmacokinetics. 2009 [cited 2014 June 4]; Available from: http://sepia.unil.ch/pharmacology/index.php?id=100.

73. Rowland, M. and T.N. Tozer, Clinical pharmacokinetics and pharmacodynamics: concepts and applications. Fourth ed2010: Lippincott Williams & Wilkins.

# CHAPTER 2

# INFLUENCE OF SIZE AND SPECIFICITY ON PHARMACOKINETICS, BIODISTRIBUTION, AND TUMOR TARGETING OF WIDELY USED BIOLOGICS: REQUIREMENT OF SPECIFICITY FOR TUMOR INTERNALIZATION

**Abstract**

Sensitive and specific detection of tumor growth and progression is significant for its ability to better diagnose and stage cancer, and to assess tumors' response to treatment. In this endeavor, a variety of biologics have been used, revealing that molecular size and a half-life in the blood are more dominant parameters for tumor detection than specificity of biologics to tumor antigens. However, few studies exist that used widely used biologics in parallel to examine the parameters that would influence biodistribution, and tumor localization and internalization. Here, we used fluorescently-labeled six different biologics (antibodies, antibody fragments, serum albumin, and streptavidin) and measured their distribution at whole body, ex-vivo tissue, and cellular levels in mice bearing human cervical cancer cells. Although the highest localization into the tumor was obtained with full-length antibody specific to tumor antigen, serum albumin and streptavidin were overall superior in tumor to blood ratios. To our surprise, Fab format of antibodies, comparable in size to albumin and streptavidin, were much inferior in tumor detection to albumin and streptavidin,

partly due to faster clearance of Fab from the blood. Despite high level of localization into the tumor, neither control antibodies nor albumin and streptavidin were not found inside cells. It indicates that specificity to tumor antigen was required for tumor cell internalization by biologics. In summary, our study emphasizes that specific tumor detection by molecular targeting needs to be validated by comparing its biodistribution and targeting with that of control antibodies or other biologics (e.g., albumin). Furthermore, the use of biologics as a cytotoxic drug carrier will require specificity to tumor markers in order to achieve not only localization but also internalization in tumor cells.

**Introduction**

Molecular imaging, enabled by contrast agent-conjugated small molecules, antibodies, and other recombinant peptides or proteins that are more selective towards tumor cells than normal ones, becomes increasingly more important for its ability to better diagnose and stage cancer, and to assess tumor response to treatment. Unlike biologic labeling of tumors in vitro where affinity and specificity of molecules are dominant factors, in vivo tumor detection is much more complex as molecules are first subject to body's physiology before they are distributed in the vicinity of tumors. The factors affecting biologic performance in cancer detection in vivo include molecular size and shape, clearance rate from blood, specificity, and affinity for target antigens [1-4]. The properties inherent to tumor itself also influence sensitivity and specificity of biologics in molecular imaging, such as size and tendency for non-specific uptake, vascular and lymphatic supplies, and permeability within the tumor [5-8].

Previous studies using native antibodies (full-length immunoglobulin (Ig)), enzymatically truncated formats (e.g., Fab, $(Fab')_2$), and various recombinant antibody variants (e.g., scFv, scFv-Fc, diabody, triabody) have revealed that selectivity and affinity are not the only factors that determine their tumor detection capacity [9-11]. With comparable or even lower binding affinity, it has previously been shown that smaller variants of antibodies achieved higher tumor-to-blood ratios than that of Ig [11, 12]. Moreover, in another study using scFv-Fc with the same size and binding affinity but significantly different clearance kinetics, it has disclosed that the fragment versions with shorter serum half-life produced clearer tumor images [10]. In these situations the difference in size and clearance rate from the body circulation mainly contributed to the outcome, emphasizing the importance of pharmacokinetic parameters in molecular imaging. Besides, intriguingly, several studies using serum albumin and streptavidin have also demonstrated that much of tumor localization by biologics is ascribed to passive diffusion of molecules through leaky vasculature within the tumor. This is due to the fact that tumor vasculature is more permeable (pore size ~200-600 nm) then normal vessel (pore size less than ~5 nm [2, 13, 14]), except vascular sinusoids in the liver, spleen, and bone marrow. Only molecules smaller than the vasculature pore sizes are allowed to pass through and extravasate from circulation. Once the molecules emigrate and localize in tumors with less developed lymphatic drainage, they can be accumulated and retained for a long period of time within the tumor, an effect known as enhanced permeability and retention (EPR) effect. The passive tumor targeting then raises an interesting question whether and to what extent, Ig or Ig variants with specificity to tumor antigens would be superior to similarly sized molecules in imaging and therapy applications.

Beyond localization in tumors, defining internalization characteristics of biologics becomes a critical issue when the biologics are developed as therapeutic carriers. Drug carriers that preferentially deliver drugs to target sites attain selectivity by means of molecular targeting, EPR effect, or the combination of both. To date clinically approved drug carriers are built with cancer drugs covalently coupled to antibodies or encapsulated within nanoparticles (e.g., Doxorubicin containing pegylated liposomes (Doxil) and Paclitaxel serum albumin (Abraxane)). Through receptor-mediated endocytosis, antibody-drug conjugates are internalized into cells, while non-specific uptake by cells is mainly responsible for drug delivery by non-targeted nanoparticle-carriers.

Despite a plethora of studies demonstrating the influence of size and specificity on tumor detection, to our knowledge, there have been few studies that have examined, in parallel in the same animal model, widely used biologics for their biodistribution, pharmacokinetics, and tumor detection as well as internalization. Here, we have chosen mice xenografted with human cervical cancer cells (HeLa) with overexpression of a molecule known as intercellular adhesion molecule (ICAM)-1. ICAM-1 is constitutively over-expressed in many carcinomas including breast, colon, non-small cell lung, and gastric tumors compared to respective normal epithelial cells, and in tumor stroma within an inflammatory network [7]. In terms of biologics, we used mouse antibody against ICAM-1 and control antibody, both of them in Ig and fragment antigen binding (Fab) formats. To compare how size, specificity, and pharmacokinetics affect tumor detection, we also used serum albumin and streptavidin, which are currently being used for drug carrier and imaging applications in clinic. Our study shows that biologics such as serum albumin and streptavidin with optimum size and clearance rate can outperform similarly sized molecules with

specificity to tumor antigens. However, for internalization of biologics into tumors, we found that specificity to tumor antigen is essential.

## Materials and methods

### *Mammalian cell culture*

HeLa, and HEK 293 cells (ATCC) were cultured in Advanced Dulbecco's modified Eagle's medium containing 10% (v/v) fetal bovine serum, 2 mM L-alanyl-L-glutamine dipeptide, and 100 U/ml Penicillin-Streptomycin (all from Invitrogen) at 37°C in a 5% $CO_2$ humidified incubator.

### *Purification of monoclonal antibody R6.5 IgG and enzymatic fragments*

A mouse R6.5 or R6-5-D60 IgG2a was produced by a mouse-mouse hybridoma cell line; R6.5.D6.E9.B2, also called R6-5-D60 (ATCC® HB-9580™) [15]. The hybridoma cells were maintained under culture conditions listed on the ATCC website (http://www.atcc.org/products/all/HB-9580.aspx#culturemethod). In summary, the cells were propagated in RPMI 1640 medium supplemented with 10% (v/v) fetal bovine serum, 2 mM L-alanyl-L-glutamine dipeptide, 100 U/ml Penicillin-Streptomycin, and 5 μg/ml Plasmocin™ (InvivoGen) at 37°C in a 5% CO2 for a few passages before antibody production. Maintain cultures at a cell concentration between $3\times10^4$ and $5\times10^5$ cells/ml during propagation. The cells were then switched to CD Hybridoma media with 2 mM L-alanyl-L-glutamine dipeptide, 100 U/ml Penicillin-Streptomycin, and 5 μg/ml Plasmocin™ during antibody production process. R6.5 IgG was affinity purified from cell culture supernatants using Affi-

Gel® Protein A MAPS™ II Kit (Bio-Rad). Eluted fractions were immediately neutralized, concentrated using 10 kDa cut-off Amicon Ultra-15 Centrifugal Filter Units (EMD Millipore) and desalted into phosphate-buffered saline (PBS) upon PD-10 Desalting Columns (GE Healthcare). Fab fragments were generated by the digestion of the purified IgG with papain, as previously described [16]. Briefly, one volume of 2 mg/ml purified R6.5 IgG in PBS, pH 6.2 was incubated at 37°C for 15 h with one volume of 0.02 mg/ml papain (Sigma-Aldrich) in freshly prepared digestion buffer, PBS containing 0.02M ethylenediaminetetraacetic acid disodium salt and 0.02M cysteine (both from Sigma-Aldrich), pH 6.2. The Fab fragments were separated from the other digestion products, Fc and undigested IgG, by Affi-Gel® Protein A MAPS™ II Kit followed by buffer exchange into PBS using PD-10. The protein concentration of purified antibody and fragment was determined by NanoDrop (Thermo Scientific). Sodium dodecyl sulfate polyacrylamide gel electrophoresis (SDS-PAGE) was further used to qualitatively analyze purified antibody as well as digestion products.

*In vitro binding and internalization assays*

Biologics used for this study include a murine anti-human ICAM-1, R6.5 IgG, mouse IgG from mouse serum (Sigma-Aldrich), Fab fragments of R6.5 and control IgG, streptavidin (Invitrogen), and bovine serum albumin (BSA) (Fisher Scientific). Prior to binding and internalization study, Alexa Fluor® 488 sulfodichlorophenol ester (Alexa488) and Alexa Fluor® 750 succinimidyl esters (Alexa750) were covalently conjugated to the biologics. Degree of labeling (D.O.L.) of each dye was determined using Nanodrop following the manufacturing protocol. To test biologic binding in vitro, HeLa and HEK 293 cells were

trypsinized and washed with ice-chilled complete cell culture medium. 10 μg/ml Alexa Flour® labeled biologics were incubated with cells (200,000 cells per labeling sample) in 50 μl completed cell culture medium on ice for 1 h. Cells were washed twice in 300 μl of completed cell culture medium. After final washing, cells were resuspended in 300 ml PBS and subjected to flow cytometer (BD-Biosciences LSRII Flow Cytometer). For quantitative uptake evaluation, the biologic labeled cells were chased for 0, 1 or 3 h in cell culture medium at 37°C. At the end of chasing time, cells were rapidly chilled and half the samples were incubated on ice for 2 h with (surface quenched samples) or without (unquenched samples) 25 ug/ml rabbit anti-Alexa488 (Molecular Probes, Invitrogen A11094) in 70 μl complete cell culture medium. The cells were then washed twice before FACS analysis. The amount internalized was calculated from collected mean fluorescence intensity data after correcting for incomplete surface quenching, as previous described [17, 18]

*Subcutaneous tumor model and biologic treatments*

HeLa cells ($3\times10^6$) suspended in 1:1 PBS: Matrigel (BD) mixture in a total volume of 150 μl were injected subcutaneously on the back around lower flank area of 4-wk-old female, severe combined immunodeficiency (SCID) hairless outbred (SHO) mice, approx. weight 20 g (strain code: 474, Charles River Laboratories). Tumor growths were measured using a vernier caliper and the tumor volumes were calculated by formula: 0.5 × length × $(\text{width})^2$. When tumors reached approximately 150 $mm^3$, the animals were randomized into eight different groups (n = 3) and were treated with the same mass (100 μg) of different fluorescently-labeled biologics in sterile PBS buffer (200 μL) via retro-orbital injections using 29G insulin syringes. R6.5 and control IgG groups were each conducted with 2

terminal time points; 24 and 168 h. All animal experiments were performed in compliance with the guidelines of the Institutional Laboratory Animal Use and Care Committee of Cornell University.

*Pharmacokinetic studies*

After biologic administration, the blood (30 μL) was collected at different time points through the submandibular vein using 22G needles. The plasma (15 μL) was separated from whole blood by centrifugation (5000×g, 10 min). The collected plasma was kept at -20°C until analysis. The fluorescent signal from the plasma (10 ul in black 384 well microplates (Corning)) was measured by a microplate reader (Bio-Tek). The amount of biologics was quantified according to a standard curve, which was achieved by adding various amounts of the test materials to the plasma of an untreated mouse. The pharmacokinetic parameters were determined by fitting the percentage of injected dose per milliliter of blood (% ID/mL) versus time (h) curve into a two-compartmental pharmacokinetic model using PK Solver Microsoft Excel plug-in freeware as described previously [19].

*In vivo imaging and biodistribution studies*

In vivo imaging was performed in real-time by optical imaging using a Xenogen IVIS-200 (Perkin Elmer). Mice were anesthetized with 5% isoflurane (VetOne) before they were placed in the Xenogen and maintained at 2% isoflurane during whole body imaging. The whole body fluorescence images were acquired using the ICG channel at different time points. At the terminated time point, the mice were euthanized, the tumor and major tissue and organs were dissected, and ex vivo fluorescence images were obtained. Images and

measurements of fluorescent signals were acquired and analyzed with Living Image software. The fluorescent signal measurement data of biologic materials prior to injection were used to quantify the amount of biological materials in each organ. The biodistribution of the biologics in various organs was then calculated and normalized in unit of percentage of injected dose per gram of tissue (% ID/g).

*In vivo internalization detection*

Collected tumors at terminated time points (24 or 168 h post biologic administration) were dissociated using collagenase A (Roche) as described previously [20]. In brief, tumors were minced and digested in 1 mg/ml collagenase A in complete DMEM medium for 2 h at 37 C. Singlet lung cells were prepared by passage through 70 μm nylon mesh cell strainer (BD Falcon) and incubation with red blood cell lysis buffer (eBiosciences, San Diego, CA, USA) for 20 min at room temperature. Cells were then washed and divided into 2 groups, 100,000 cells each, with and without surface fluorescence quenching by the rabbit anti-Alexa488. The samples were then subjected to FACS analysis. Internalized fluorescence was calculated from quenched and non-quenched sample data as described earlier in 2.3 In vitro binding and internalization assays.

*Statistical analysis*

Data were expressed, unless otherwise stated, as mean ± standard error of the mean (SEM), of no smaller than triplicates. Statistical analysis of data was performed using GraphPad Prism 5 (Graphpad Software). Differences with p values $< 0.05$ were considered significant. Student's t-Test was used for testing the difference between two means (Fig. 6B).

Two-way ANOVA was used to compare the mean responses of different biologic treatments to different time points or to different tissues, followed by Bonferroni post-hoc test to determine statistical significance (Fig. 2A, Fig. 3C,D, & Fig. 4B).

## Results

*Preparation of biologics, in vitro assays to confirm ICAM-1 dependent binding*

Natural IgG and enzymatically truncated or recombinant variants of IgG have been the dominant sources of biologics for molecular imaging applications. Besides antibodies, two other widely used biologics include bovine serum albumin and streptavidin for their superior in vivo safety and pharmacokinetics. In this study, ICAM-1 specific monoclonal antibody (mAb), R6.5 (mouse IgG2) in native and Fab formats were used to selectively bind ICAM-1 positive HeLa cells. As a control for R6.5, polyclonal IgG purified from mouse serum was used. In total, we examined six different biologics, differing in size (50-150 kDa) and specificity to ICAM-1, in mice bearing subcutaneous HeLa xenograft (Fig. 1A).

mAb R6.5 was produced from hybridoma (~20 mg/L of culture supernatant), and purified to >95% purity (Fig. 1B). Fab fragments of both R6.5 and control IgG were produced by treating antibodies with papain, followed by removal of antibody Fc fragment with protein A column (Fig. 1C). Under a reducing condition of SDS-PAGE, Fab migrated as two bands of heavy and light chain fragments. To confirm size and purity, all six biologics were purified and analyzed by non-reducing SDS-PAGE (Fig. 1D). Mouse IgG migrated into at least two distinct bands, indicative of polyclonality consisting mainly of IgG1 and IgG2 isotypes. Streptavidin (~52 kDa) and BSA (~66 kDa) migrated close to their theoretical

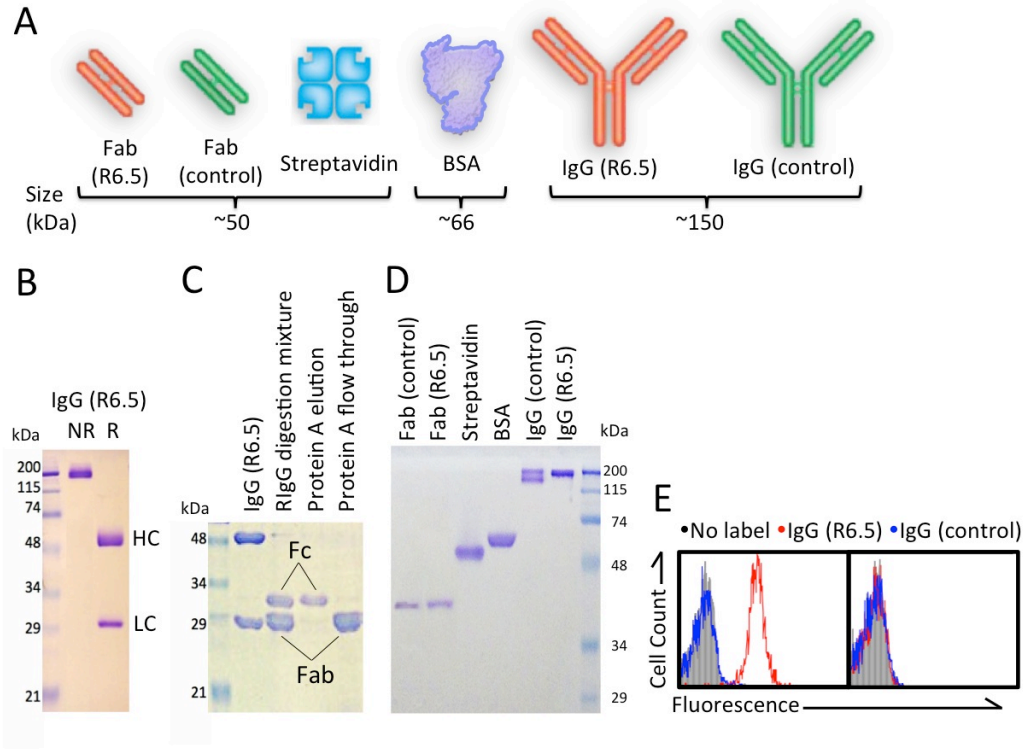


**Figure 1.** Preparation of biologics and in vitro assays to confirm ICAM-1 dependent binding. (A) Schematic illustration and sizes of studied biologics. Coomassie blue stained 12% SDS-PAGE analysis of (B) protein A purified R6.5 IgG under non-reducing (NR) and reducing (R) conditions, (C) R6.5 fragments from enzymatic fragmentation under reducing condition, and (D) the studied biologics under non-reducing condition. (E) Flow cytometry histogram illustrates specific binding of R6.5 to ICAM-1. Constitutive ICAM-1 expressing HeLe cells and negative ICAM-1 expressing HEK 293 cells were incubated with Alexa488-labeled R6.5 and control IgG, washed, and analyzed by FACS. Autofluorescence of cells without labeling is shown in solid filled histogram.

molecular weights; both Fab fragments of R6.5 and control antibody exhibited faster mobility, migrating with nominal molecular weight of 40 kDa. To confirm specificity to ICAM-1 in vitro and in vivo assays, biologics were labeled with two different fluorescent dyes (Alexa488 and Alexa750). Labeling condition was adjusted to add on average, 1.2-1.5 dyes of each kind to one biologic molecule. The specificity of R6.5 against ICAM-1 was confirmed by selective binding to ICAM-1 positive HeLa but a lack of binding to ICAM-1 negative HEK 293 cells. Control IgG, BSA, and streptavidin exhibited no discernible binding above background levels to either HeLa or 293 cells (Fig. 1E and data not shown).

*Measurement of biologics' pharmacokinetics*

Prior to imaging biologics for biodistribution in mice, we first examined pharmacokinetics of each molecule by measuring its concentration in the blood over 1 or 7 days postinjection, which was plotted as the percentage of injected dose per milliliter of blood (%ID/mL) versus time (days) (Fig. 2A). These measurements were then used to fit the two compartmental PK model, which is characterized by an initial rapid clearance from the central compartment (blood and well perfused organs) to the peripheral compartment (poorly perfused tissues) (described by rate constants, $K_{12}$ and $K_{21}$) and a slower rate of clearance due to an elimination from the central compartment (rate constant, $K_{10}$) (Fig. 2B). From this model, standard pharmacokinetic parameters were obtained that include distribution and elimination half-lives ($t_{1/2(\alpha)}$ and $t_{1/2(\beta)}$), area under the curve (AUC), mean residence time (MRT), clearance from the central compartment (CL), and volume distribution ($V_d$). The elimination half-lives of both R6.5 (IgG2a) and control IgG (polyclonal mixture) in young SCID mice were ~2 days, considerably faster than the half-lives measured in adult normal

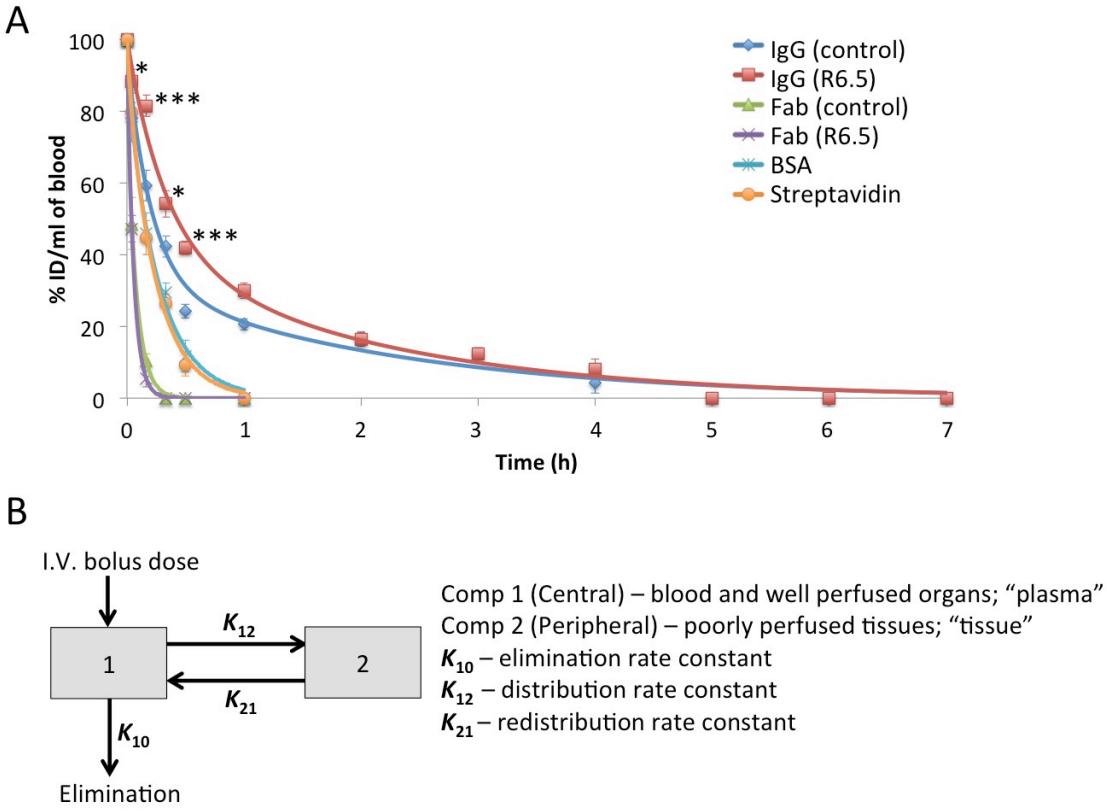


**Figure. 2**. Pharmacokinetic study. (A) Plots of the pharmacokinetic profile of the studies biologics. All the fluorescence-labeled biologics (100 mg) in sterile PBS buffer were intravenously administered into SCID mice (n = 3 for each group of animals). Blood samples were collected at different time points and analyzed for biologic concentrations. The data were plotted as a percentage of injected dose in blood (% ID/mL) versus time. Error bars are SEMs. For R6.5 and control IgG (*$p < 0.05$, ***$p < 0.001$, n = 3 (except at 1, 4, 12 and 24h post injection time points, n = 6)). (B) Scheme of two compartment pharmacokinetic model.

mice (6-8 days). Despite small difference in molecular mass, Fab fragments of R6.5 and control IgG were cleared much faster from the blood (~1 h) than BSA and streptavidin (4-5 h) (Fig. 2A & Table 1), likely due to a rapid clearance of Fab through renal filtration (~60 kDa of cut-off molecular mass).

*Whole body imaging of biologics in mice bearing human tumors*

Six different biologics labeled with near-infrared (NIR) fluorescent dyes were then compared for their biodistribution in mice xenografted with HeLa tumors (Fig. 3). Overall, highest accumulation into tumors was associated with ICAM-1 specific antibody, R6.5, which persisted up to 7 days after injection. Consistent with faster clearance of Fab from circulation, bright signals were detected in the kidneys of the mice injected with Fab. Despite being specific to HeLa, R6.5 Fab was marginally better than Fab of control antibody in delineating tumors. In comparison, BSA and streptavidin, which would localize to the tumors through EPR effect, provided higher signals in the tumor than Fab fragments. When the signal intensity within the tumor region was normalized to the tumor weight (%ID/g), in agreement with a visual grading of biologics in tumor detection, the time between injection and peak intensity was shortest with R6.5 Fab fragments (~1 h), followed by BSA/streptavidin (~4 h), and R6.5 IgG (~24 h). The elapsed time to peak intensities in the tumor were overall in correlation with the elimination half-lives (Fig. 3C&D and Table 1).

*Biodistribution quantification of biologics at tumor and organ levels*

Whole body imaging of NIR dyes is biased to detection of biologics distributed closer to the skin, requiring isolation and imaging of the major organs and tumors for quantitative

**Figure 3.** Real-time whole body imaging and tumor accumulation. (A, B) The merged fluorescence and bright field images of HeLa-implanted SCID mice (n = 3 for each group of animals) at different time points after intravenous administration of the fluorescence labeled biologics. (C,D) A comparison of tumor accumulation profile of the injected biologics. Images and measurements of tumor localized fluorescence signals were acquired and analyzed with Living Image software. Error bars are SEMs (*$p < 0.05$, **$p < 0.01$, ***$p < 0.001$, n = 3 (except R6.5 and control IgG at 1, 4, 12 and 24h post injection, n = 6)).

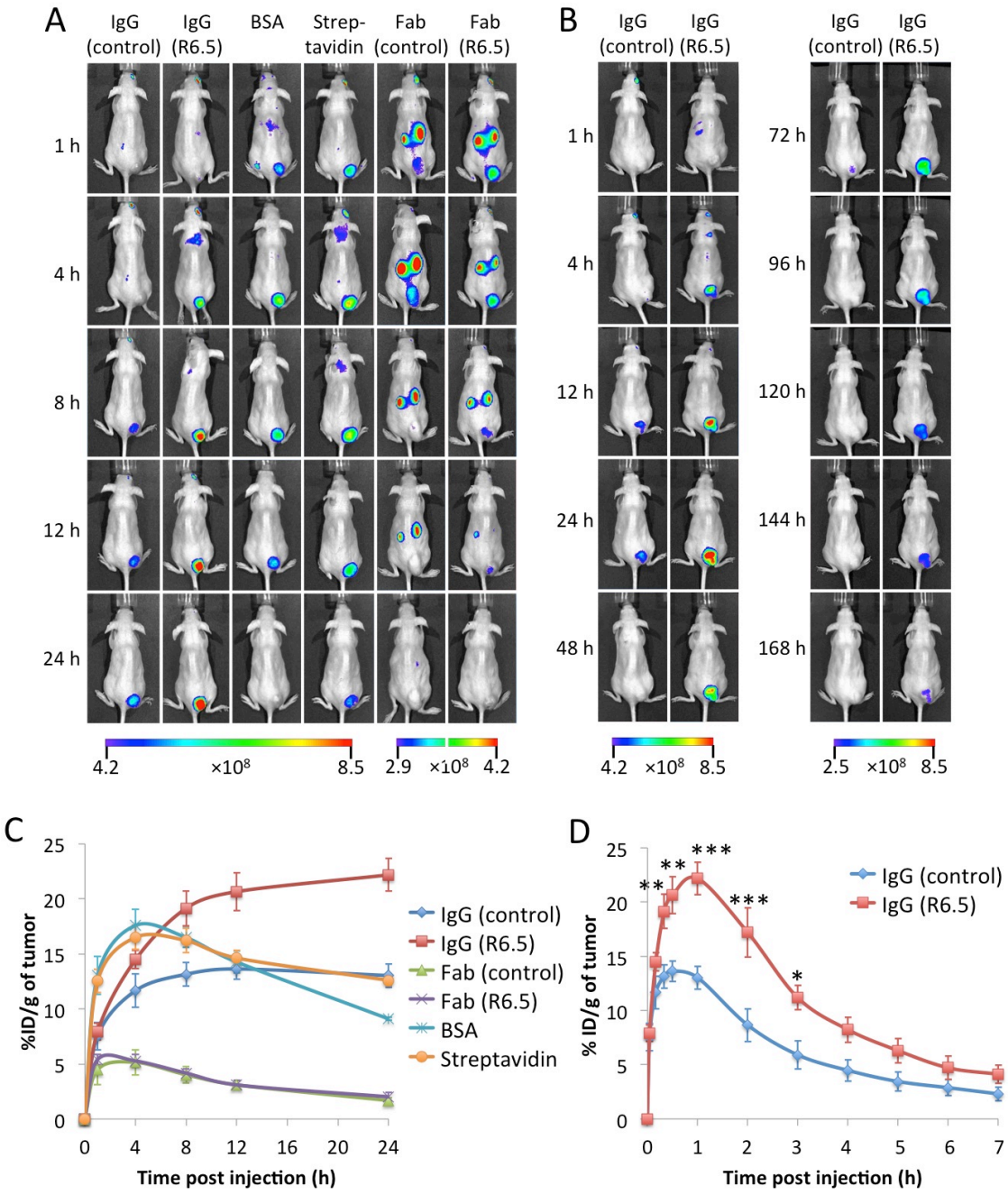
A
IgG (control)
IgG (R6.5)
BSA
Strep-tavidin
Fab (control)
Fab (R6.5)
1 h
4 h
8 h
12 h
24 h
4.2 ×10^8 8.5
2.9 ×10^8 4.2
B
IgG (control)
IgG (R6.5)
1 h
4 h
12 h
24 h
48 h
72 h
96 h
120 h
144 h
168 h
4.2 ×10^8 8.5
2.5 ×10^8 8.5
C
%ID/g of tumor
Time post injection (h)
IgG (control)
IgG (R6.5)
Fab (control)
Fab (R6.5)
BSA
Streptavidin
D
% ID/g of tumor
Time post injection (h)
IgG (control)
IgG (R6.5)
**
**
***
***
*

**Table 1**

A table showing the pharmacokinetic parameters of the biologics.

| Biologics | $t_{1/2\ (\alpha)}$ (h) | $t_{1/2\ (\beta)}$ (h) | $AUC_{0\text{-}t^*}$ (h.ug/ml) | $AUC_{0\text{-}inf}$ (h.ug/ml) | MRT (h) | CL (ml/h) | $V_d$ (ml) | $K_{10}$ (1/h) | $K_{12}$ (1/h) | $K_{21}$ (1/h) |
|---|---|---|---|---|---|---|---|---|---|---|
| IgG (control) | 3.8 | 51.5 | 1233.7 | 1607.2 | 63.7 | 0.1 | 1.6 | 0.0 | 0.1 | 0.1 |
| IgG (R6.5) | 6.5 | 52.1 | 1547.5 | 1981.3 | 61.0 | 0.1 | 1.5 | 0.0 | 0.0 | 0.0 |
| Fab (control) | 0.1 | 1.3 | 106.4 | 106.6 | 1.9 | 0.9 | 1.5 | 0.6 | 0.9 | 5.2 |
| Fab (R6.5) | 0.6 | 1.0 | 90.0 | 90.0 | 1.4 | 1.1 | 1.5 | 0.7 | 0.0 | 1.1 |
| BSA | 0.7 | 4.7 | 327.6 | 393.7 | 6.7 | 0.3 | 1.5 | 0.2 | 0.1 | 0.9 |
| Streptavidin | 0.7 | 4.1 | 315.1 | 362.7 | 5.9 | 0.3 | 1.5 | 0.2 | 0.1 | 0.9 |

*t = 168h for IgG, t = 24h for Fab, BSA and Streptavidin

Abbreviations: distribution half-life ($t_{1/2\alpha}$), elimination half-life ($t_{1/2\beta}$), area under the curve (AUC), mean residence time (MRT), clearance (CL), volume of distribution ($V_d$), elimination rate constant ($K_{10}$), distribution rate constant ($K_{12}$), redistribution rate constant ($K_{21}$).

mapping of biologics in the body. After mice were euthanized, major organs (lungs, heart, spleen, kidneys, brain, and liver) and tumors were isolated and subjected to ex vivo NIR imaging (Fig. 4A). In agreement with whole body level imaging of tumor detection at 24 h postinjection, the localization of biologic into the tumor was highest with R6.5, followed by control IgG, streptavidin, and BSA, and lowest with Fab. At 7-days after injection, signals from R6.5 were still persistent, far higher than those in the lungs and liver (Fig. 4). The uptake of biologics by the immune cells in the mononuclear phagocytic system (MPS) would produce signals in the liver, lungs, and spleen. The signal intensity (%ID/g) from the liver at 24 h was significantly higher than that from the tumor in control IgG, Fab fragments, and BSA groups. Contrarily, these live-tumor signals are comparable in the cases of R6.5 IgG and streptavidin.

By 7 days postinjection, the signal intensity of R6.5 IgG in the tumor was the only signal reliable detectable among other tissues. Although being foreign antigens in the body of mouse, BSA and streptavidin localization to MPS organs at 24 h were not significantly different from those of mouse IgGs (Fig. 4).

*Validation of in vitro assays to confirm ICAM-1 specific internalization*

Biologics that not only localize but also internalize into tumors will be advantageous as a molecular probe as their association with the site of tumors would be longer than the molecules residing outside of cells. For the use of biologics as drug carriers, internalization into cells via specific molecular interaction may be a key to achieve targeted cell death. The magnitudes and kinetics of internalization into cells were investigated using anti-AF488 antibody, which bind and quench AF488 that is covalently coupled to biologics. Therefore,

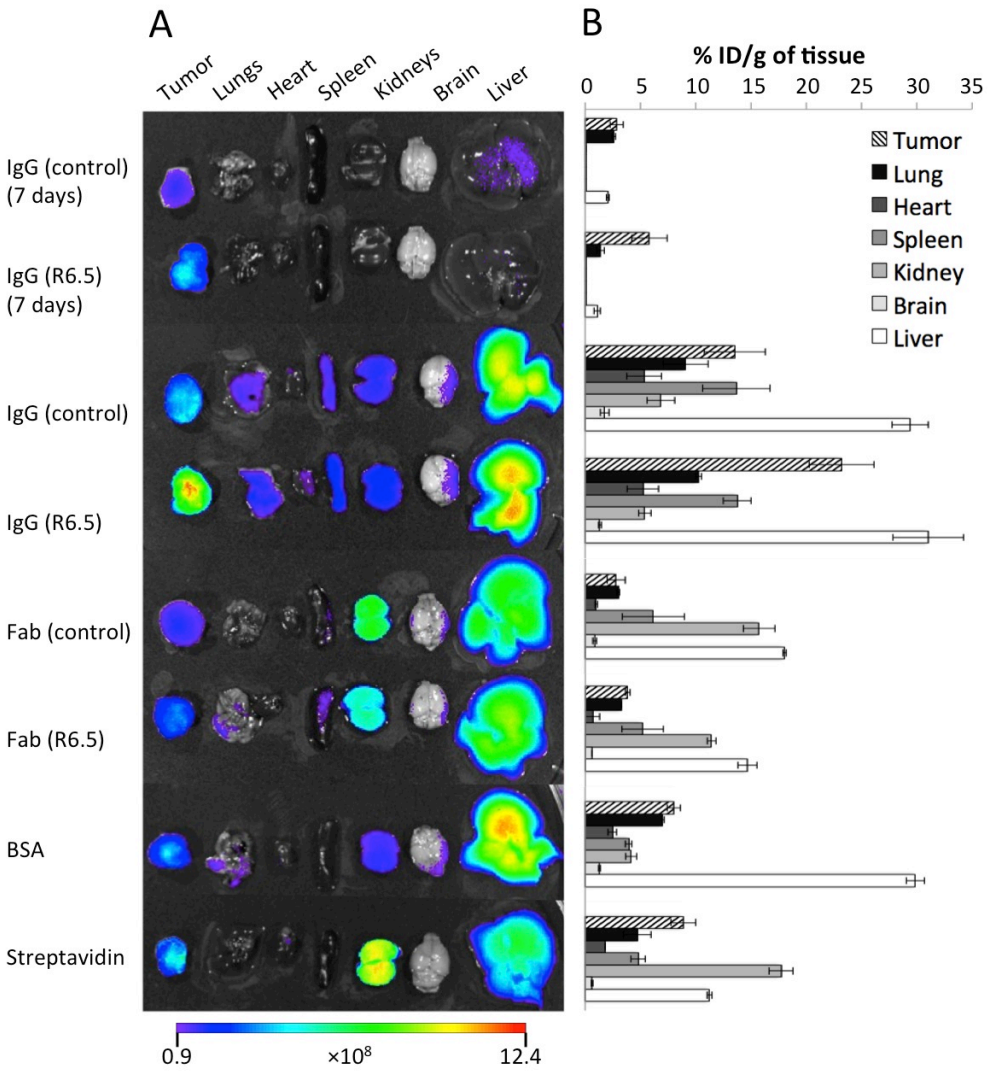


**Figure 4.** Biodistribution of biologics at tumor and major organs. The merged fluorescence and bright field images (A) and a bar chart shows the percentage of injected dose (% ID/g of tissue) ± SEM (B) of harvested HeLa tumors and different organs at 24h and 7d post biologic administration (n = 3 for each treatment group).

the higher degrees of reduction in fluorescence intensity after quenching with anti-AF488 antibody, the more biologics remain bound on cell surface without internalization. For this assay, HeLa was first labeled with R6.5 and Fab fragment of R6.5 at 4°C to prevent antibody internalization, and a subset of R6.5 labeled cells was subsequently incubated with anti-AF488 antibody. As shown in Fig. 5A, the level of fluorescence labeling was much higher with R6.5 IgG than Fab, indicating that monomeric interaction between R6.5 Fab and ICAM-1 was not high affinity and could be greatly dissociated during washing steps. After anti-AF488 antibody labeling, there was substantial fluorescence reduction in both cases, amounting to approximately 92±4% and 88±3% decreases for IgG and Fab, respectively. To investigate the degree of internalization of R6.5 IgG and Fab, surface labeled cells were then incubated at 37°C for 1 and 3 hours to induce antibody internalization. The reduction of fluorescence after addition of AF488 antibody was then used to compute the amount of R6.5 IgG and Fab internalization. After 3 h incubation at 37°C, the level of internalization was comparable for both R6.5 IgG and R6.5 Fab at ~20% (Fig. 5A&B).

*Specific interaction is required for cell binding and internalization*

We then examined the level of tumor binding and internalization of all the studied biologics after i.v. administration. For this assay, singlet cells were isolated from the harvested tumors. The cells were then subjected to flow cytometry to measure the amount of biologics associated with HeLa cells, from the combination of both cell surface binding and internalization (Fig. 6A&B). To our surprise, there was little signal associated with non-ICAM-1 binding biologics, independent of the level of tumor localization. This suggests the biologics passively accumulated into the tumor through EPR effect remained outside of cells

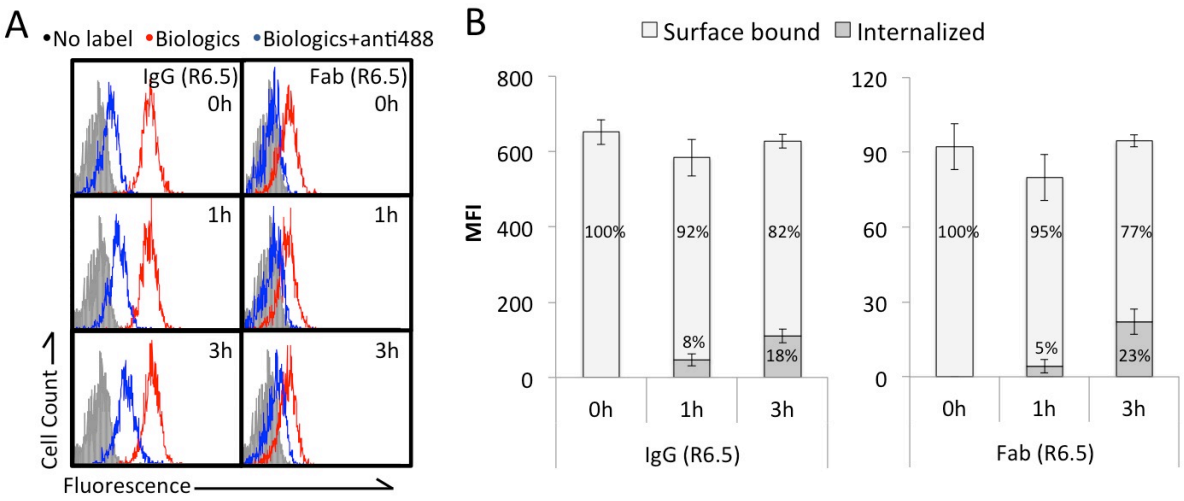


**Figure 5.** In vitro assays to confirm ICAM-1 specific internalization. (A) HeLa cells were bound with 1 ug/ml Alexa488-labeled R6.5 IgG or Fab variants on ice, washed and chased for 0, 1, or 3 h at 37°C (• Biologics). Half of the samples were surface quenched with anti-Alexa488 (• Biologics+anti488) prior to FACS analysis. (B) Internalization and surface fractions of ICAM-1 bound R6.5 IgG and Fab are shown in bar graph as MFI ± SEM (n=3).

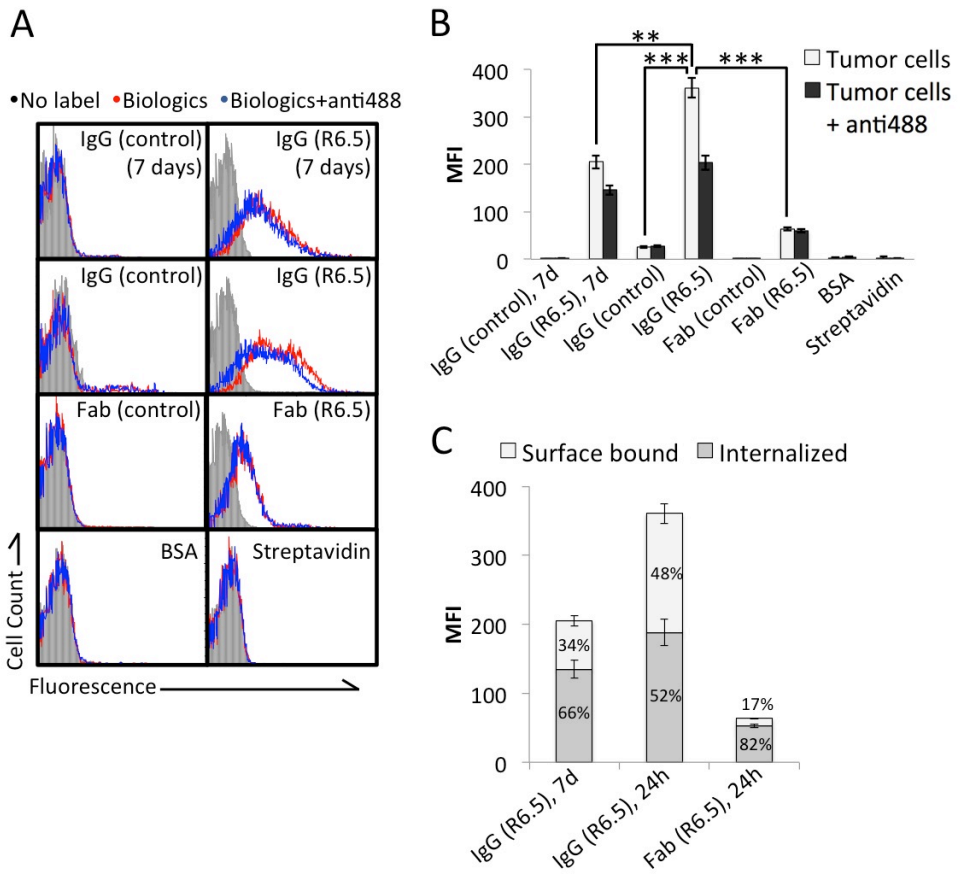


**Figure 6.** Specific interaction is required for cell binding and internalization (A) Binding and internalization study of the biologics into HeLa cells isolated from xenograft tumors. Collagenase-digested tumors, collected at 24h and 7d post biologic injections (• Biologics) were halved and surface quenched with anti-Alexa488 (• Biologics+anti488) prior to FACS analysis. Digested tumors from non-treated mice were also collected and measured for autofluorescence (• No label). (B) MFI measured by FACS in Fig. 6A are quantitatively shown in bar graph. (C) Internalization and surface fractions of ICAM-1 bound R6.5 IgG and Fab were shown in bar graph. All error bars in this figure denote SEM (**$p < 0.01$, ***$p < 0.001$, $n = 3$).

and were washed out in the course of cell isolation. On the other hand, both R6.5 IgG and Fab were found to label the isolated HeLa cells remarkably. From the amount of fluorescence quenching by anti-AF488 antibody, the percentage of R6.5 IgG internalized into cells was determined to be as much as 50-65%. The degree of internalization was even higher with R6.5 Fab, reaching ~80%, ascribed to lower affinity of R6.5 Fab, which would enable only internalized Fab to be associated with HeLa cells.

**Discussion**

Biologics labeled with contrast agents for optical imaging, MRI, and PET have been actively developed for early and sensitive detection of cancers utilizing specific-targeting biomarkers. However, the presence of leaky vasculature and hypotension within the tumor, and inherent difference in vascularity and leakiness in different types of tumors present challenges to determining relative contribution of specific molecular interaction versus EPR effect on tumor localization. In order to study the influence of specificity and pharmacokinetics of biologics on tumor localization, we used IgGs and Fab fragments, and other widely used biologics, i.e., serum albumin and streptavidin, to examine in parallel tumor localization and internalization in mice xenografted with human cancer cells. Our studies recapitulated prior studies that biologics such as albumin and streptavidin, due to their ideal size and plasma half-life in the blood, are useful reagents in tumor detection by EPR effect. As a matter of fact, the amount of albumin and streptavidin localized to the tumor was better than ICAM-1 specific Fab fragments with a shorter half-life in blood, reaffirming the caution that targeting by IgG variants, such as scFv and Fab, was to a great extent from EPR

effect. However, of biologics comparable in size and pharmacokinetics, specificity to target antigen was associated with higher accumulation into tumors and more importantly binding and internalization into tumor cells.

The biologics used for detecting tumor locations and even tumor phenotype, e.g., expression of specific biomarkers, need to be determined for the best time window for imaging after injection to maximize detection sensitivity and signal-to-noise ratios. Our study suggests that the time-to-peak intensity of Fab fragments and non-antibody biologics in tumor detection was almost equal to their elimination half-lives in the blood, i.e., ~1 h for Fab fragments and 4 h for serum albumin and streptavidin. In the case of IgGs, the highest or near highest intensity was observed ~24 h, falls between the time to reach 50% reduction in concentration (~12 h) and the elimination half-lives (~50 h). However, the signals of most biologics used in this study were significantly lower in the tumor than those in the liver at 24 h after injection. R6.5 IgG showed almost comparable signals between the tumor and the liver at 24 h, and by 7 days postinjection, tumor was the only tissue that retained significant level of R6.5. Although, no intermediate measurements were performed between 24 h and 7 days, by interpolating the changes of R6.5 in the ratios of tumor to other organs, it is likely that as early as 2 days postinjection, the signal in the tumor would be far above the signals in other tissues.

One of the most important findings in our study is the demonstration that specific molecular interaction was necessary for biologics to bind and enter cells. Biologics taken by cells would then largely avoid gradual clearance by the body, and increase signal-to-noise ratios in tumor detection. Of particular importance is the ability to go inside target cells if biologics are to be used to as a carrier of therapeutics, e.g., antibody-drug conjugates. This is

to a considerable degree in contrast to prior observations with nanoparticles where nanoparticles as drug carriers can be taken up by cells without specific molecular interactions. Particle-based drug carriers would be superior in the aspect of delivering a large content of drugs per particle, superior specificity to target cells attained by antibodies may compensate for the lower ratio of drug to biologic ratios.

In summary, our study underscores the influence of size and pharmacokinetic parameters of biologics on tumor localization, and emphasizes the need for careful examination of biologic biodistribution in evaluating tumor phenotypes.

# REFERENCES


1. Chames, P., et al., Therapeutic antibodies: successes, limitations and hopes for the future. British journal of pharmacology, 2009. 157(2): p. 220-33.
2. Sanna, V., N. Pala, and M. Sechi, Targeted therapy using nanotechnology: focus on cancer. International journal of nanomedicine, 2014. 9: p. 467-83.
3. James, M.L. and S.S. Gambhir, A molecular imaging primer: modalities, imaging agents, and applications. Physiological reviews, 2012. 92(2): p. 897-965.
4. Ferrari, M., Cancer nanotechnology: opportunities and challenges. Nature reviews. Cancer, 2005. 5(3): p. 161-71.
5. Shi, J., et al., Self-assembled targeted nanoparticles: evolution of technologies and bench to bedside translation. Accounts of chemical research, 2011. 44(10): p. 1123-34.
6. Heneweer, C., et al., Magnitude of enhanced permeability and retention effect in tumors with different phenotypes: 89Zr-albumin as a model system. Journal of nuclear medicine : official publication, Society of Nuclear Medicine, 2011. 52(4): p. 625-33.
7. Jain, R.K., Transport of molecules, particles, and cells in solid tumors. Annual review of biomedical engineering, 1999. 1: p. 241-63.
8. Jain, R.K. and T. Stylianopoulos, Delivering nanomedicine to solid tumors. Nature reviews. Clinical oncology, 2010. 7(11): p. 653-64.
9. Qi, J., et al., Pharmacological efficacy of anti-IL-1beta scFv, Fab and full-length antibodies in treatment of rheumatoid arthritis. Molecular immunology, 2014. 57(2): p. 59-65.
10. Kenanova, V., et al., Tailoring the pharmacokinetics and positron emission tomography imaging properties of anti-carcinoembryonic antigen single-chain Fv-Fc antibody fragments. Cancer research, 2005. 65(2): p. 622-31.
11. Casey, J.L., et al., Preparation, characterisation and tumour targeting of cross-linked divalent and trivalent anti-tumour Fab' fragments. British journal of cancer, 1996. 74(9): p. 1397-405.

12. Sharkey, R.M., et al., Biodistribution and radiation dose estimates for yttrium- and iodine-labeled monoclonal antibody IgG and fragments in nude mice bearing human colonic tumor xenografts. Cancer research, 1990. 50(8): p. 2330-6.
13. Choi, H.S., et al., Renal clearance of quantum dots. Nature biotechnology, 2007. 25(10): p. 1165-70.
14. Schmidt, M.M. and K.D. Wittrup, A modeling analysis of the effects of molecular size and binding affinity on tumor targeting. Molecular cancer therapeutics, 2009. 8(10): p. 2861-71.
15. Springer, T.A., et al., Intercellular adhesion molecules, and their binding ligands, 1994, Dana Farber Cancer Institute, Boston Mass.: USA. p. 1-71.
16. Andrew, S.M. and J.A. Titus, Fragmentation of immunoglobulin G. Current protocols in cell biology / editorial board, Juan S. Bonifacino ... [et al.], 2003. Chapter 16: p. Unit 16 4.
17. Austin, C.D., et al., Endocytosis and sorting of ErbB2 and the site of action of cancer therapeutics trastuzumab and geldanamycin. Molecular biology of the cell, 2004. 15(12): p. 5268-82.
18. Shen, B.Q., et al., Conjugation site modulates the in vivo stability and therapeutic activity of antibody-drug conjugates. Nature biotechnology, 2012. 30(2): p. 184-9.
19. Wagh, A., et al., A short circulating peptide nanofiber as a carrier for tumoral delivery. Nanomedicine : nanotechnology, biology, and medicine, 2013. 9(4): p. 449-57.
20. Kang, S., et al., Virus-mimetic polyplex particles for systemic and inflammation-specific targeted delivery of large genetic contents. Gene therapy, 2013. 20(11): p. 1042-52.

# CHAPTER 3

# INFLAMED LEUKOCYTE-MIMETIC NANOPARTICLES FOR MOLECULAR IMAGING OF INFLAMMATION


**Abstract**

Dysregulated host inflammatory response causes many diseases, including cardiovascular and neurodegenerative diseases, cancer, and sepsis. Sensitive detection of the site of inflammation will, therefore, produce a wide-ranging impact on disease diagnosis and treatment. We hypothesized that nanoprobes designed to mimic the molecular interactions occurring between inflamed leukocytes and endothelium may possess selectivity toward diverse host inflammatory responses. To incorporate inflammation- sensitive molecular interactions, super paramagnetic iron oxide nanoparticles were conjugated with integrin lymphocyte function-associated antigen (LFA)-1 I domain, engineered to mimic activated leukocytes in physiology. Whole body optical and magnetic resonance imaging in vivo revealed that leukocyte-mimetic nanoparticles localized preferentially to the vasculature within and in the invasive front of the tumor, as well as to the site of acute inflammation. This study explored in vivo detection of tumor-associated vasculature with systemically injected inflammation-specific nanoparticles, presenting a possibility of tumor detection by



This chapter is modified and reprinted from, Chen X, Wong R, Khalidov I, Wang AY, Leelawattanachai J, Wang Y, and Jin M. Inflamed leukocyte-mimetic nanoparticles for molecule imaging of inflammation. Biomaterials 2011;32(30):7651–7661, with permission from the publisher. Leelawattanachai J assisted in the animal experiments with regard to Fig 3b, Fig 3c, Fig 3d, Fig 4a, Fig 4b, Fig 4c, Fig 4d, Fig 4g and Fig 4h.

inflamed tumor microenvironment.

## Introduction

Dysregulated inflammatory responses of the host are implicated in the pathogenesis of many human diseases [1]. Acute inflammation from infection can cause sepsis [2], while chronic inflammation, and continual coexistence between acute and chronic inflammation are associated with various neurodegenerative [3] and cardiovascular diseases [4], metabolic disorders [5], and cancer [6,7]. Accordingly, sensitive and early detection of inflammation and site-specific delivery of anti-inflammatory agents will have a wide-ranging impact on the treatment of various inflammation-related diseases. Upon induction of inflammation, a set of adhesion molecules is upregulated in endothelium, with which immune cells interact using counter adhesion molecules such as integrins to adhere to endothelium and to initiate diapedesis. Many existing studies have investigated targeted nanoparticles for the detection and treatment of inflammation employing antibodies or peptides specific to adhesion molecules such as intercellular adhesion molecule (ICAM)-1 [8-10], vascular cell adhesion molecule (VCAM)-1 [11-13], selectins [14], and collagen [15], all of which display distinct spatiotemporal responses to inflammation. Among these molecules, ICAM-1 has caught a particular interest because of its highly inducible and localized expression upon inflammatory signals, serving as a marker for inflammation despite its constitutive low level expression [16,17].

In this study, we developed nanomicelle encapsulating super paramagnetic iron oxide (SPIO) nanoparticles, designed for facile and robust conjugation with targeting moieties and

in vivo detection by optical imaging and magnetic resonance imaging (MRI). In order to design nanoparticles to mimic the behavior of inflamed leukocytes in their ability to locate to the inflamed site, SPIO nanoparticle was coated with an optimum number of high affinity inserted (I) domain of integrin called lymphocyte function-associated antigen (LFA)-1 [18], a physiological receptor for ICAM-1. Leukocyte-mimetic nanoparticles were examined for detection of ICAM-1 overexpression in tumor cells, tumor vascular microenvironment, and acute inflammation in vivo. With our recently developed MRI technique for quantitative mapping of contrast agent [19,20], we explored the possibility of quantitative spatiotemporal mapping of iron oxide distribution in vivo using a mouse model of acute inflammation.

## Materials and methods

### *Preparation and characterization of protein coated SPIO nanomicelles*

Oleic acid-capped super paramagnetic iron oxide (SPIO) nanocrystals (Ocean Nanotech, LLC) in 5 mg were suspended in 1 ml chloroform with 12 mg 1,2-dipalmitoyl-sn-glycero-3-phosphoethanolamine-N-[methoxy(polyethylene glycol)-2000](DPPE-PEG) and 3 mg 1,2-dioleoyl-sn-glycero-3-[(N-(5-amino-1-carboxypentyl)-iminodiacetic acid)succinyl] nickel salt (DOGS-NTA) (Avanti Polar Lipids, Inc.). For radiolabeled nanoparticles, 60 μCi of L-α-Dipalmitoyl-Phosphatidylcholine, [Choline-Methyl-3H] (Perkin Elmer) was also added at this step. After 10 min sonication and overnight desiccation, 1 ml of water was added to the residue to form a micelle layer on SPIO. After another 10 min sonication and filtration through 0.22 μm filters (Millipore), optically clear suspension containing SPIO micelles were obtained. Empty micelles without

SPIO in the core were removed by ultracentrifugation. SPIO nanoparticles were purified and resuspended in pH 7.4 phosphate-buffered saline (PBS) by size exclusion S200 column (GE Healthcare). The wild-type (wt), D137A, and F265S/F292G mutants of LFA-1 I domains fused to His tag (6 histidine residues) at the N-terminal were produced as previously described [17]. Conjugation of SPIO with His tagged I domains was obtained by incubation at 4 °C overnight. Free proteins were removed by size exclusion. All fluorescently labeled SPIO nanoparticles were prepared by covalently conjugating Alexa Fluor (AF) succinimidyl esters (Invitrogen) to the I domains. Conjugation of fluorescence dyes to the proteins rather than to phospholipid was chosen due to significant fluorescence quenching between iron oxide and AF-phospholipids. The coating density of proteins on SPIO was determined from the ratio of SPIO amount (OD600nm 1 = 0.42 mg/ml) and the concentration of the proteins bound to SPIO (by Lowry's method). Specific activities of radiolabeled SPIO were measured by scintillation counter (Beckman Coulter LS6500). Dynamic light scattering (DLS, Malvern Instruments) was used to measure the average hydrodynamic size of SPIO after assembly and protein conjugation. Transmission electron microscopy (TEM; FEI Tecnai) images of SPIO were also taken before and after protein conjugation. 1% uranyl acetate was used for protein staining.

*Cell culture*

All mammalian cells used in this study were cultured in Advanced Dulbecco's modified Eagle's medium containing 10% (v/v) fetal bovine serum and 2 mM L-glutamine (Invitrogen) at 37 °C in a 5% $CO_2$ humidified incubator. For induction of inflammation, bEnd.3 (ATCC) cells were treated with 1 μg/ml of LPS (Escherichia coli. 026:B6, Sigma) for

12 h. HeLa and 293T cells stably expressing GFP were established using pSMPUW-miR-GFP/Puro Lentiviral Expression Vector system (Cell Biolabs).

*Immunofluorescence flow cytometry*

Cells were trypsinized and washed once with the ice-chilled labeling buffer (pH 7.4 PBS, 1% (w/v) BSA, 1 mM $MgCl_2$). 100,000 cells were incubated in 100 μl of the labeling buffer for 30 min on ice with 10 μg/ml of Alexa Fluor labeled proteins or SPIO conjugated with the same amount of proteins. For competition assay, 50 μg/ml of unlabeled proteins were included in the labeling buffer during incubation. Cells were washed twice and resuspended in 300 μl of the labeling buffer and subjected to flow cytometer (Beckman Coulter EPICS XL-MC).

*Microscopy visualization of cell labeling in vitro*

For immunofluorescence microscopy detection of protein labeling, cells were plated, washed in pH 7.4 PBS, and fixed with 4% paraformaldehyde for 15 min. After washing three times, cells were incubated with 10 μg/ml of Alexa Fluor labeled proteins in PBS/Triton (pH 7.4 PBS, 0.3% (v/v) Triton X-100, 1 mM $MgCl_2$) at room temperature for 1 h. Cells were rinsed once with pH 7.4 PBS and twice with high salt PBS (pH 7.4 PBS, 0.4 M NaCl, 1 mM $MgCl_2$). 300 nM DAPI (4,6-diamidino-2-phenylindole, Invitrogen) in PBS was then added and incubated for 10 min for nucleus staining. Stained cells were washed and imaged with a confocal microscope (Zeiss LSM 710). For detection of SPIO labeling, HeLa cells were plated and incubated with 50 μg/ml of SPIO coated with Alexa fluor 488 conjugated proteins in culture media for 2 h at 37 °C. Cells were washed in pH 7.4 PBS, incubated for 1 h in

serum-free medium for chasing, and imaged using confocal microscopy (Leica TCS SP2). After fluorescence imaging, cells were then prepared for Perl's Prussian blue staining for iron detection. Labeled cells were fixed with 4% paraformaldehyde, followed by incubation in a freshly prepared solution of 2% potassium ferrocyanide in 2% HCl for 20 min and counterstaining with 1% neutral red.

*Magnetic cell labeling and quantification*

Trypsinized cells were incubated for 4 h at 37 °C in the labeling buffer (PBS, 1 mM $MgCl_2$) under constant rotating with different concentrations of radiolabeled SPIO, washed and then fixed in 4% paraformaldehyde. Cells were divided into two conditions, half of which were used for radioactivity measurement using scintillation counter (Beckman Coulter LS6500), while the remaining half for MRI scanning and QSM measurement after imbedding in 100 μl 2% agarose block. MR imaging of the magnetically labeled cells were performed on a 3T MRI scanner (Signa, GE, Milwaukee, WI). A 3D multi-echo gradient sequence was used to sample multiple TEs in one TR. Imaging parameters were as follows: TEs 3.696 ms, 4.196 ms, 5.696 ms, 11.696 ms, 35.696 ms; TR 40 ms; flip angle 30°; matrix size 256 × 64 × 64; voxel size 500 $\mu m^3$ isotropic. A 3D Fourier transform was applied to the raw k-space data to reconstruct $T2^*$ weighted images. QSM was obtained through Multiple Orientation Sampling (COSMOS) technique, as previously described [19].

*Subcutaneous tumor model*

$3\times10^6$ human cervical cancer HeLa cells and human embryonic kidney 293T cells stably expressing GFP mixed in Matrigel (BD) were injected bilaterally into the front lower

flank areas of 8-wk-old female nude mice. Mice were used for experiments 16-20 days after injection when tumor size reached about 300 $mm^3$. All animal experiments were conducted in compliance with the regulations defined by the Institutional Laboratory Animal Use and Care Committee of Cornell University.

*Acute LPS-inflammation model*

For subcutaneous LPS, 1 mg/ml LPS in 100 μl PBS and 100 ml PBS were injected bilaterally into the lower flank areas of 8-wk-old female BALB/c mice. For systemic LPS, 1 mg/ml LPS in 100 μl PBS were injected into 8-wk-old female BALB/c mice. Prior to imaging hair was removed to reduce background fluorescence.

*Near-IR optical imaging of mice*

Animals were anesthetized with isoflurane mixed with oxygen at 5% and maintained at 2% isoflurane during whole body imaging (Olympus, OV100). Mice were administered with SPIO coated with AF750-conjugated proteins in 150 μl PBS via retro-orbital injection. 500 and 100 μg of SPIO were used for tumor imaging and acute inflammation models, respectively. Near-IR images were taken at different time points post-injection of SPIO. Tumor growth was detected by imaging green fluorescence. Image analysis was performed with Matlab R2007a (MathWorks).

*MR imaging of mice with acute inflammation*

For subcutaneous LPS model, prior to nanoparticle injection mice were exposed to LPS/PBS for 12 h. At 4 h after injection of SPIO in 150 μl PBS, mice were euthanized by

intraperitoneal injection of 2.5% tribromoethanol (20 μl/g), transcardially perfused with PBS, and fixed in paraformaldehyde. Prepared mice were scanned on a 7T scanner (Bruker BioSpin, Biospec 70/30 USR) with 3D FLASH sequence. Imaging parameters were as follows: TEs (echo time) 5 ms, 6 ms, 30 ms, 35 ms; TR (repetition time) 35 ms; excitation pulse angle 15°; matrix size 150 × 150 × 100; voxel size 200 $mm^3$ isotropic; NEX 1. A 3D Fourier transform was applied to the raw k-space data to reconstruct the images [19]. For systemic LPS model, prior to nanoparticle injection mice were exposed to LPS for 12 h. At 1, 8, and 25 h post-injection of SPIO coated with proteins in 150 μl PBS, mice were euthanized likewise. Prepared mice were scanned on a 3T scanner (GE Signa Excite) with 3D multi-echo EFGRE sequence [19]. Imaging parameters were as follows: TEs 3.696 ms, 4.196 ms, 5.696 ms, 11.696 ms, 35.696 ms; TR 40 ms; flip angle 30°; matrix size 256 × 64 × 64; voxel size 500 $\mu m^3$ isotropic. QSMs were reconstructed using the COSMOS technique, as previously described.

*Histology*

Tumor and normal tissues were collected from tumor bearing mice before or at the end of in vivo imaging experiments. 10 μm frozen tissue sections were sliced, fixed in paraformaldehyde, and stained with hematoxylin and eosin (H&E) or in Perl's Prussian blue. Images of the tissue sections were acquired by scanscope (Aperio). For immunofluorescence, antibodies used include rat anti-mouse CD31 (BD, MEC13.3) and goat anti-rat IgG labeled with AF350 (Invitrogen). Six different fields of view containing CD31 staining for each sample were counted using 25 Chalkley's random point method over an area of 0.16 $mm^2$ for vascularity analysis (Fig. 3d). To quantify the level of staining, three different regions of

interest (ROI) with 0.50 $mm^2$ area were sampled for each condition in immunofluorescence staining (Fig. 3c) and four ROI with 0.04 $mm^2$ area in each Prussian blue staining (Fig. 4f). Specific colors (blue for endothelium and Prussian blue, red for F265S/F292G) were extracted and intensities were measured using Image-Pro Plus 6.0 (Media Cybernetics) and ImageJ 1.41 (NIH).

*Statistical analysis*

Data were expressed as mean ± standard deviation of no smaller than triplicates, and analyzed for statistical significance using GraphPad Prism 5 (Graphpad Software). Linear regression was used to examine the correlation between SPIO measurements by radioactivity and QSM (Fig. 2c). One-way ANOVA was used to compare the staining and vascularity levels between different tissues, followed by Tukey's post-hoc test to determine statistical significance (Fig. 3c,d). Two-way ANOVA was used to compare the mean responses of different nanoparticles to different time points or to different tumors, followed by Bonferroni post-hoc test to determine statistical significance (Fig. 4d,f, Fig. 5b, & Fig. 6c,d).

**Results**

*Synthesis and characterization of leukocyte-mimetic nanoparticles*

Selective binding of SPIO nanoparticles to overexpressed ICAM- 1 was conferred by surface coating at an optimal density (~100 molecular/particle) with the I domain of LFA-1 integrin, engineered for high affinity by mutations of F265S/F292G (denoted as F265S/F292G, $K_D$ = 6 nM) [18]. Among physiological ligands for LFA-1 such as ICAMs and

junctional adhesion molecule (JAM)-1 [21], ICAM-1 is most important in the setting of leukocyte adhesion to inflamed endothelium due to its highest affinity to LFA-1 [22], being highly inducible over basal low level expression, and localized expression upon inflammatory signals [16,23]. In order to fine-tune coating density of F265S/F292G and present targeting moiety in a most functional orientation, oleic acid-capped SPIO nanocrystals (Ocean Nanotech) were encapsulated with a layer of phospholipid consisting of 80% n-poly(ethylene glycol) phosphatidylethanolamine (DPPE-PEG) and 20% dioleoyl-glycero-succinyl-nitrilotriacetic acid (DOGS-NTA) (Fig. 1a). DOGS-NTA was used for non-covalent conjugation of targeting moieties with His tag in a robust and reproducible manner via high affinity binding to nickel ions chelated by NTA (Ni-NTA) [17,24]. DPPE-PEG was included to maintain solubility, stability, and for its low immunogenicity and non-specific binding to cells and tissues in vivo [25]. Transmission electron microscope (TEM) images revealed monodispersed SPIO nanocyrstals with an outer layer of micelle-like structure (Fig. 1b; dark ring density corresponds to uniformly distributed nickel ions (the black arrow in top right) and diffuse dark density to His-tagged proteins attached to Ni-NTA (the white arrow in bottom right)). Hydrodynamic size of SPIO with or without protein conjugation was measured to be 60 ± 10 nm by dynamic light scattering (DLS), an increase from 15 nm diameter SPIO core mainly due to the addition of phospholipid and PEG.

Prior to detecting ICAM-1 with nanoparticles, we first examined by immunofluorescence flow cytometry (Fig. 1c) and fluorescence microscopy (Fig. 1d) soluble I domain (labeled with Alexa Fluor 488 (AF488), Invitrogen) binding to ICAM-1 expressed in monolayer culture of cervical cancer cells (HeLa). Specific binding to ICAM-1 was detected with the F265S/F292G, which was inhibited by unlabeled F265S/F292G.

**Figure 1.** Synthesis, characterization, and in vitro delivery of leukocyte-mimetic nanoparticles. (a) A schematic diagram of iron oxide nanocrystals encapsulated into a micelle-like layer composed of amphiphilic phospholipid copolymers (stage I-II) and subsequent protein conjugation for molecular targeting (stage III). (b) Uniformly sized, monodispersed SPIO with 15 nm core revealed by TEM. A close up view on top demonstrates a dark halo corresponding to nickel ions (black arrow) chelated by NTA groups surrounding SPIO. On the bottom is the negative staining of protein-conjugated SPIO with proteins and PEG groups darkly stained (white arrow), in contrast to a brighter phospholipid layer. (c) Flow cytometry measurements of HeLa cells stained with different I domains (10 μg/ml) labeled with AF488. Non-stained HeLa cells are shown in grey shaded histograms. In a competition assay, non-labeled I domains were used at 50 μg/ml. (d) Shown in green is immunofluorescence staining of ICAM-1 in HeLa cells using F265S/F292G labeled with AF488. Nuclei staining by DAPI is shown in blue. (e) Flow cytometry measurements of HeLa cells stained with nanoparticles (25 μg/ml of SPIO and 10 μg/ml of I domains) conjugated with different I domains. Non-labeled I domains as a competitor were used at 50 μg/ml (f) ICAM-1 dependent internalization of SPIO into HeLa cells was confirmed with confocal fluorescence microscopy and Perl's Prussian blue staining.

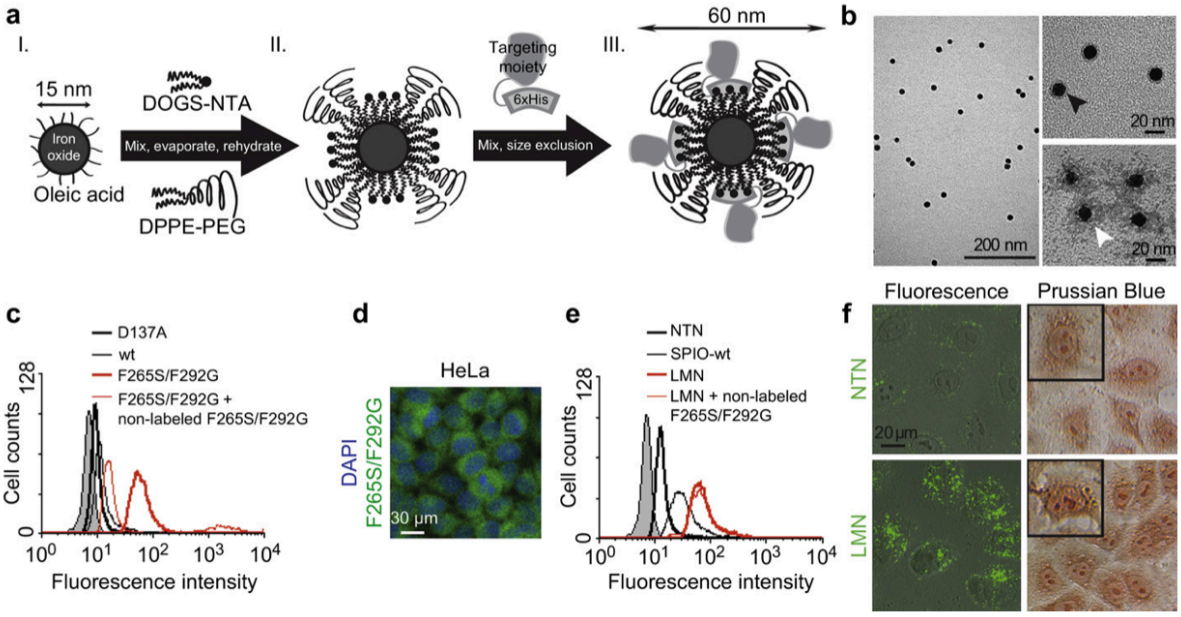
a
I.
15 nm
Iron oxide
Oleic acid
DOGS-NTA
DPPE-PEG
Mix, evaporate, rehydrate
II.
Targeting moiety
6xHis
Mix, size exclusion
III.
60 nm
b
200 nm
20 nm
20 nm
c
D137A
wt
F265S/F292G
F265S/F292G + non-labeled F265S/F292G
Cell counts
128
0
$10^0$ $10^1$ $10^2$ $10^3$ $10^4$
Fluorescence intensity
d
HeLa
DAPI
F265S/F292G
30 µm
e
NTN
SPIO-wt
LMN
LMN + non-labeled F265S/F292G
Cell counts
128
0
$10^0$ $10^1$ $10^2$ $10^3$ $10^4$
Fluorescence intensity
f
Fluorescence
Prussian Blue
NTN
LMN
20 µm

In contrast, no significant binding was observed with the wt I domain ($K_D$ = 1.7 mM) [22] and the I domain containing a mutation of D137A [17], which disrupts the metal-ion dependent adhesion site (MIDAS) and abolishes ICAM-1 binding. The level of nanoparticle binding coated with the I domain variants was overall in good agreement with the soluble I domain binding, which varied in order from highest to lowest, F265S/F292G, wt, and D137A (Fig. 1e). Markedly, specific binding of SPIO conjugated with F265S/F292G (abbreviated as Leukocyte-Mimetic Nanoparticle or 'LMN') was not inhibited by competition with soluble I domain, presumably due to multivalent interaction between nanoparticles and HeLa cells. Enhanced binding due to avidity effect was also observed in the binding of nanoparticle coated with the wt I domain to HeLa, which resulted in greater binding than with the free wt I domain. ICAM-1-mediated binding of LMN but not with the nanoparticles coated with D137A (abbreviated as Non-Targeted Nanoparticle or 'NTN') led to significant cell surface labeling and internalization into the cells, evidenced by fluorescence microscopy and Perl's Prussian blue staining (Fig. 1f).

*Quantitative measurement of selective binding of LMN by MRI*

SPIO nanoparticles are being used in clinics as T2* negative contrast agent for MRI. In order to validate SPIO as MRI contrast agent as well as to test the accuracy of our MRI technique for quantitative mapping of SPIO [19], $^3$H-labeled phospholipid was additionally incorporated into the outer phospholipid layer of SPIO. When HeLa cells were incubated with LMN for 4 h at 37 °C, an increase in concentration led to an increase in cellular uptake of nanoparticles, reaching a plateau at 450 ng/$10^6$ cells (Fig. 2a). LMN delivery was specific to ICAM-1 expression, evidenced by little accumulation into HeLa with NTN and much

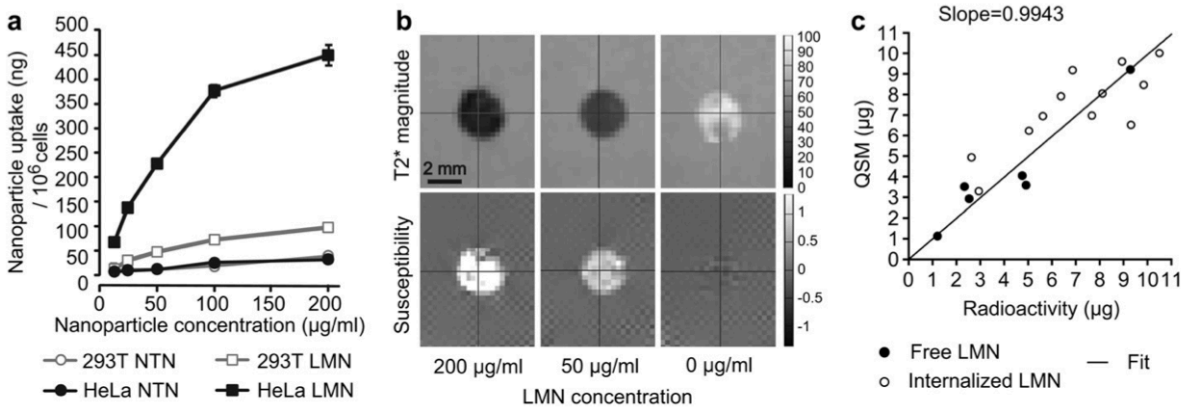


**Figure 2.** Quantitative measurement of selective binding of SPIO to ICAM-1 by MRI. (a) The amount of SPIO internalized into HeLa or 293T was measured by radioisotope measurement of $^3$H-phospholipid incorporated into SPIO nanoparticles. SPIO nanoparticles were coated with either F265S/F292G (LMN) for ICAM-1 targeting or with D137A (NTN) as a control. (b) T2* and susceptibility images of agarose-embedded HeLa cells that were labeled with 200-0 μg/ml of LMN. (c) A comparison of iron mass estimated by QSM technique and radioisotope measurement. Shown are the measurements of agarose-embedded free LMN (closed circles) and LMN internalized into HeLa cells (closed circles).

lower delivery with LMN into 293T, a cell line with no or little expression of ICAM-1. HeLa cells with known amount of internalized LMN by $^{3}$H-radioisotope decay were then embedded into agarose and scanned with a MRI scanner. As expected, T2* showed a decrease in magnitudes with an increase in the amount of SPIO (Fig. 2b). With quantitative susceptibility mapping (QSM) algorithm was observed a close agreement with ~30% standard deviation from direct radioactivity measurements of free or intracellular SPIO, highlighting the ability of QSM in detecting as low as 1 μg accumulation into 100 μl in volume (Fig. 2c).

*Ex vivo detection of ICAM-1 induction in human tumor xenograft and in inflamed stroma*

Not only is ICAM-1 upregulated in several carcinomas compared to respective normal epithelium, implicating active involvement of ICAM-1 in cancer development, its induction has also been observed in tumor vasculature caused by an inflamed network encompassing tumor and tumor microenvironment [26-28]. Previously, we have found that human LFA-1 I domain cross-reacted with murine ICAM- 1 [17], which was recapitulated by the staining of ICAM-1 induced in murine brain endothelium (b.End3) after lipopolysaccharide (LPS) treatment (Fig. 3a). When tissue sections of GFP-expressing HeLa xenograft were analyzed for ICAM-1 detection by soluble F265S/ F292G labeled with AF594 (Invitrogen), most of the GFP signal was overlapped with red fluorescence (Fig. 3b). Notably, we found that the majority of endothelial cells (PECAM-1 (CD31) positive) within the tumor were also stained by F265S/F292G. In contrast, the level of ICAM-1 induction and colocalization with CD31 staining in the vasculature away from the tumor, such as those in the skin, was far lower, amounting to ~15% compared to 70% and 35% of the vasculature

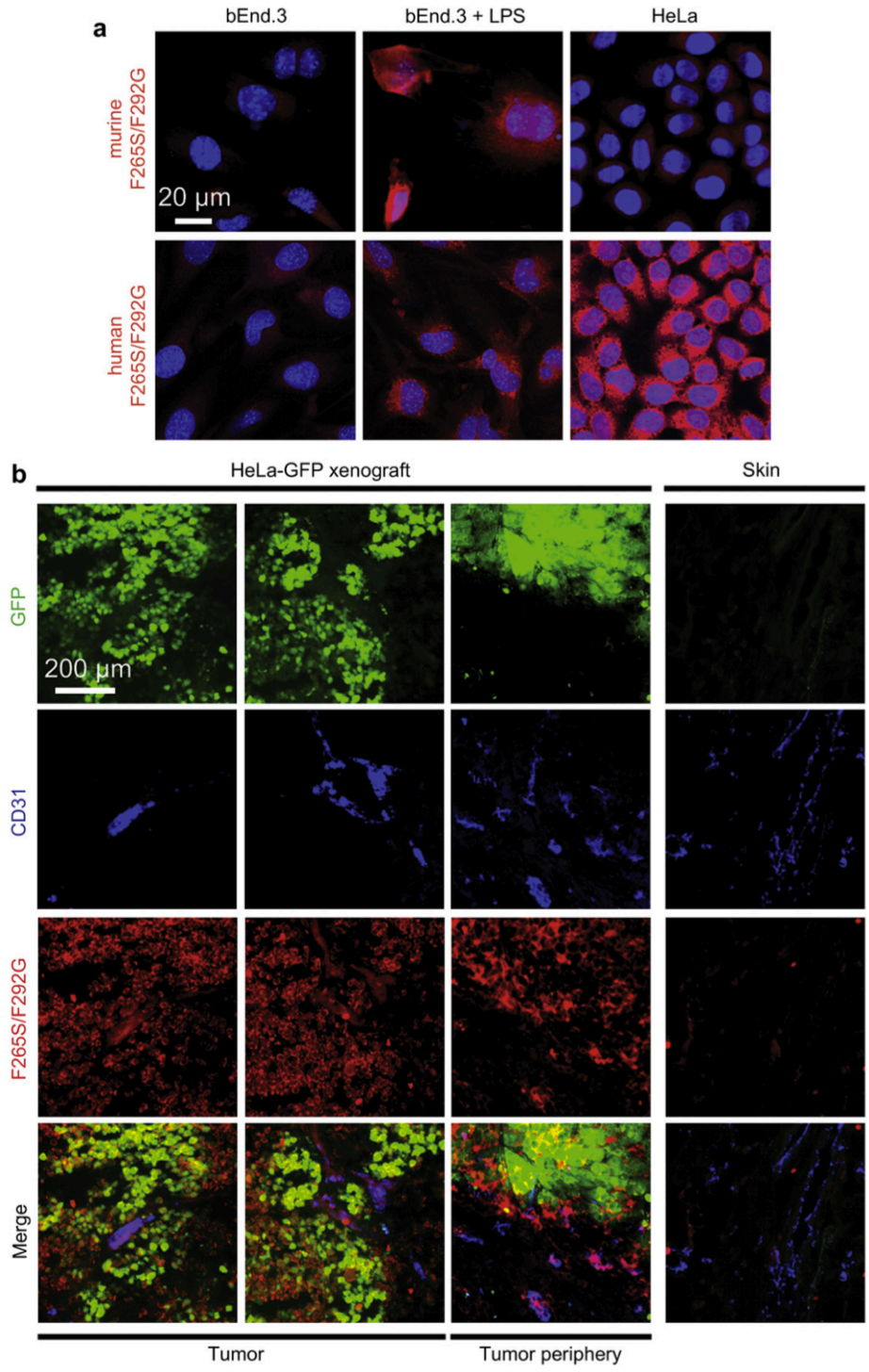
a
bEnd.3
bEnd.3 + LPS
HeLa
murine F265S/F292G
human F265S/F292G
20 μm
b
HeLa-GFP xenograft
Skin
GFP
CD31
F265S/F292G
Merge
200 μm
Tumor
Tumor periphery

Fig. 3 (continued)

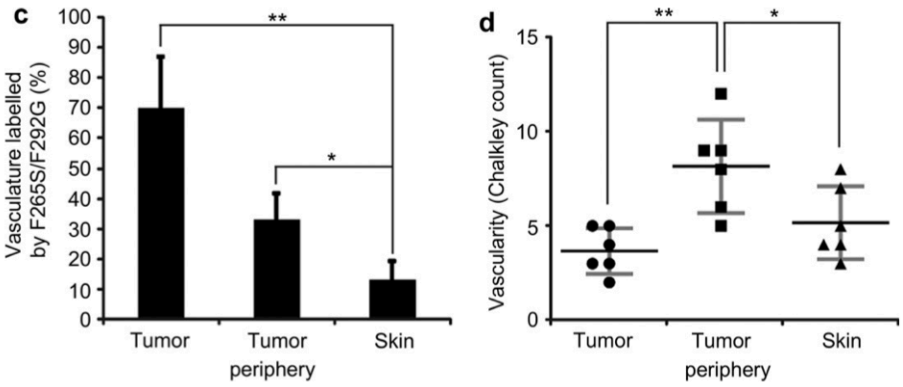


**Figure 3.** Ex vivo molecular imaging of tumor and tumor-associated vasculature. (a) Confocal fluorescence images of murine b.End3 cells before and after LPS treatment and HeLa cells stained with murine (top) and human (bottom) I domains (F265S/F292G) labeled with AF594. Nuclei staining by DAPI is shown in blue. (b) Immunofluorescence images of GFP-expressing HeLa xenograft tumor tissue costained with F265S/F292G-AF594 and anti-murine CD31 antibodies. Skin tissues from non-tumor bearing mice were used as control. (c) The percentages of endothelium costained with CD31 and F265S/F292G within the tumor, in the periphery (300 μm from the tumor), and in the skin were determined from immunohistology (n = 6). (d) Vascularity within the tumor, in the periphery (300 μm from the tumor), and in the skin was quantified using Chalkley's method (25 random points per field of view) (n = 3; *$p < 0.05$, **$p < 0.01$).

within the tumor and its periphery (defined as a region within 300 μm distance from the edge of tumor), respectively (Fig. 3b-d).

*In vivo detection of ICAM-1 induction in human tumor xenograft and in inflamed stroma*

After confirming specific detection of ICAM-1 in ex vivo tumor slice by free F265S/F292G, we then examined if systemically-delivered nanoparticles would accumulate to the tumor and inflamed stroma by ICAM-1 targeting. To validate that nanoparticle localization is ICAM-1 specific and not due to an increased permeability of the tumor vasculature, NTN and ICAM-1 negative 293T cell xenograft were used as controls. The growth of HeLa and 293T xenograft in mice was confirmed by whole body imaging of GFP (Fig. 4a). At 50 h after intravenous injection of nanoparticles, whole body imaging of near-infrared (near-IR) fluorescence (AF750 attached to the I domains) indicated accumulation of LMN into HeLa but much less into 293T xenograft (Fig. 4a,b). Subsequent ex vivo imaging of the tumor and the major organs harvested from the mice further confirmed a greater level of delivery into HeLa xenograft with LMN (Fig. 4c). The signal from the kidney was by far greater than those from other organs both for LMN and NTN, indicating ICAM-1 independent clearance through the kidney (Fig. 4c). Interestingly, higher fluorescence was also detected in the liver with LMN, presumably caused by persistent, low level inflammation in the liver. Whole body imaging of nanoparticles localized to HeLa and 293T xenograft over the time course of 30 min-50 h post-injection showed that the peak accumulation occurred at 1-3 h post-injection, followed by a gradual decrease over 3 days and a complete clearance by 7 days (Fig. 4d). The presence of LMN into HeLa was also confirmed by direct staining of iron with Prussian blue (Fig. 4e,f). To map the distribution of

**Figure 4.** In vivo molecular imaging of tumor and tumor-associated vasculature. In vivo (a, b) and ex vivo (c) near-IR imaging of mice at 50 h after intravenous injection of NTN vs. LMN. GFP indicates the growth of HeLa ('1') and 293T ('2') tumors. The distribution of nanoparticles into the major organs ('3'-'8') were also examined. (d) Near-IR fluorescence intensities of HeLa and 293T tumors at different time points after intravenous injection of LMN vs. NTN (n = 4; **P < 0.01, ***p < 0.001). (e) Perl's Prussian blue staining of tumor sections collected at 50 h after the injection of LMN vs. NTN. Stained iron is marked with black arrows. (f) Percentage of cells stained in Prussian blue (top) and the intensity of Prussian blue in the field of view (bottom) within tumor sections (n = 3; ***p < 0.001 between LMN vs. NTN in Hela tumor. $^{\dagger\dagger\dagger}$p < 0.001 between HeLa and 293T tumor using LMN). (g) Immunofluorescence imaging of tumors at 4 h post-injection of LMN. Tumor sections were also stained with anti-CD31 antibody for delineating vasculature. LMN localization into the tumor vasculatures was indicated with white arrows. (h) Fluorescence imaging of tumors at 4 h post-injection of NTN.

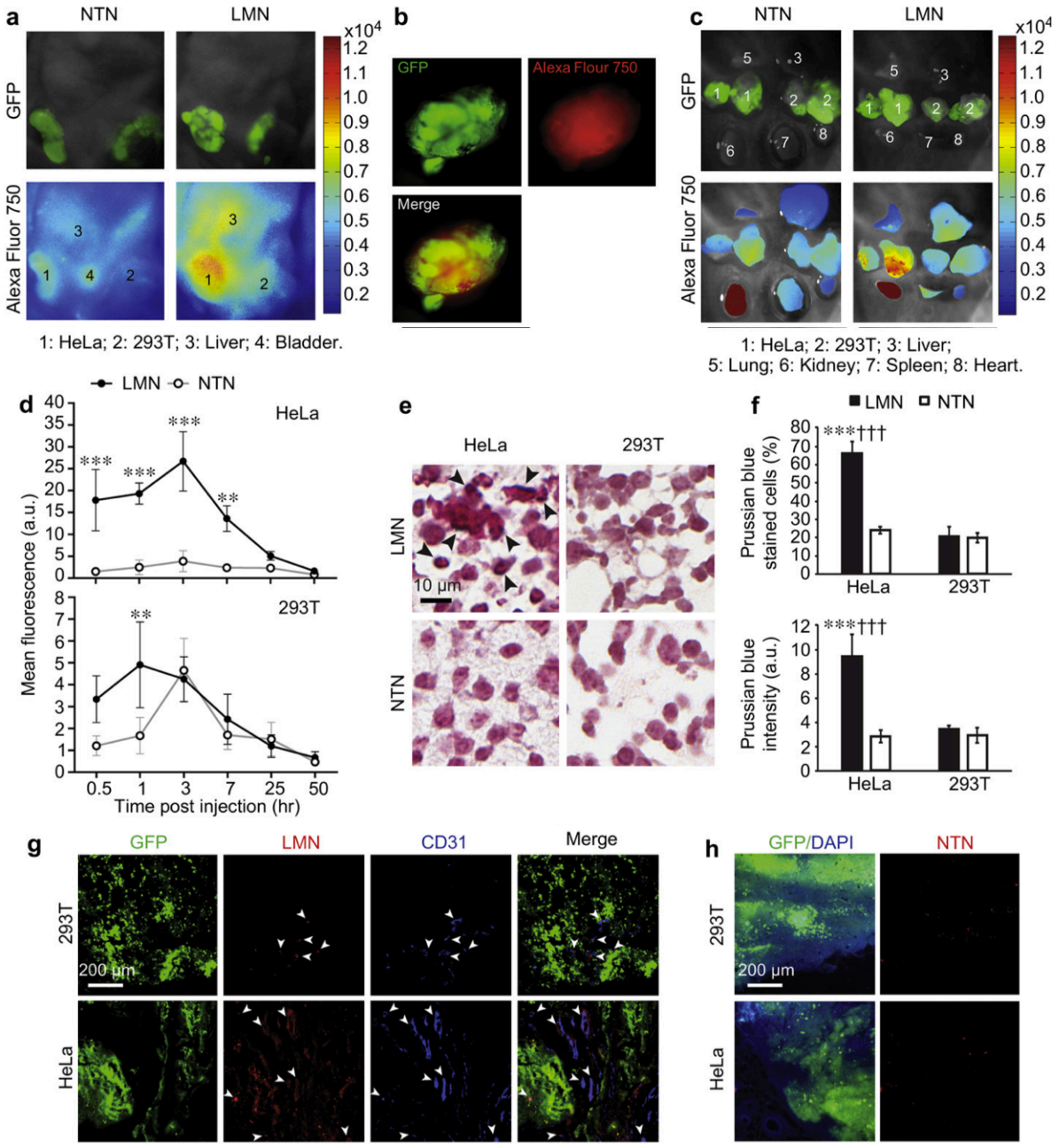
a
NTN
LMN
GFP
Alexa Fluor 750
x10^4
1.2
1.1
1.0
0.9
0.8
0.7
0.6
0.5
0.4
0.3
0.2
1: HeLa; 2: 293T; 3: Liver; 4: Bladder.
b
GFP
Alexa Flour 750
Merge
c
NTN
LMN
GFP
Alexa Fluor 750
1: HeLa; 2: 293T; 3: Liver;
5: Lung; 6: Kidney; 7: Spleen; 8: Heart.
d
LMN
NTN
HeLa
293T
Mean fluorescence (a.u.)
Time post injection (hr)
0.5
1
3
7
25
50
e
HeLa
293T
LMN
NTN
10 μm
f
LMN
NTN
Prussian blue stained cells (%)
Prussian blue intensity (a.u.)
HeLa
293T
g
GFP
LMN
CD31
Merge
293T
HeLa
200 μm
h
GFP/DAPI
NTN
293T
HeLa
200 μm

LMN by fluorescence microscopy, SPIO nanoparticles conjugated with AF594-labeled I domains were intravenously injected into the mice with HeLa/293T xenograft. When the xenograft tissue was examined 4 h after nanoparticle injection, specific accumulation of LMN into HeLa tumor was observed, judging from colocalization between GFP expression in HeLa and AF594 fluorescence (Fig. 4g,h). Importantly, consistent with the detection of ICAM-1 in the tumor vasculature by direct staining of the tissue (Fig. 3b), a high percentage of CD31 positive cells in HeLa as well as in 293T xenografts were also targeted by LMN. The localization of ICAM-1 specific nanoparticles within the tumor-associated vasculature, therefore, was likely responsible for higher signals detected within 293T xenograft at earlier time points (Fig. 4d), despite the fact that 293T itself exhibited almost no binding of LMN (Fig. 4e,f). This finding highlights a potential use of LMN for detection of tumor growth by their accumulation into inflamed tumor vasculature, irrespective of the type of tumor surface antigen.

*In vivo detection of temporal dynamics of inflammation by optical imaging and MRI*

In order to further confirm that our leukocyte-mimetic nanoparticles sensitively detect the induction of ICAM-1 not only due to an inflammatory milieu in the tumor but also by acutely induced inflammation, we imaged mice after subcutaneous (Fig. 5) or intravenous injection of LPS (Fig. 6). Temporal mapping of nanoparticle distribution demonstrated a greater localization of LMN into the LPS injection site over PBS injection site as a control, peaking at 12 h post-injection of LPS and gradually decaying over 72 h (Fig. 5a,b). Higher accumulation into the liver was also observed with LMN, attributed to the inflammatory response induced by the leakage of locally injected LPS into circulation. We also observed a

rapid increase in fluorescence in the bladder, irrespective of targeting moieties, attributed to renal clearance of some fraction of proteins dissociated from nanoparticles. Interestingly, NTN accumulated more into the LPS site than into the PBS site, presumably due to non-specific phagocytosis of nanoparticles by immune cells. Selected mice treated with systemic delivery of 100 μg LMN were then subjected to MRI after whole body optical imaging to demonstrate that our nanoparticles could be used for quantitative detection of inflammation by a clinically relevant imaging technique (Fig. 5c). T2* magnitude images identified the presence of LMN in the LPS injection site as darkness, which could be confused with other dark regions. QSM revealed the accumulation of ~0.3 μg of iron oxide (corresponding to detection of less than 1% of injected dose) into the LPS injection site, colocalized with the site identified by near-IR imaging (Fig. 5a).

In response to systemic inflammation caused by intravenous injection of LPS for 12 h prior to nanoparticle (~200 μg) injection, optical mapping of nanoparticle distribution demonstrated greater localization of LMN in the liver compared to that of NTN in mice (Fig. 6a,c), peaking at 1h post-injection of nanoparticles and subsequently diminishing at later time points. The level of delivery overall was higher with LPS even with NTN, indicating some of nanoparticles accumulated into the liver was caused by ICAM-1 independent phagocytosis. After optical imaging, mice were transcardially perfused with PBS for MRI, which would have removed nanoparticles retained in the blood pool in the liver. Temporal mapping of SPIO distribution using MRI QSM measured about 20% of the total dose of LMN was specifically uptaken by the liver 1 h post-injection due to LPS-induced inflammation (Fig. 6b,d and supplementary videos). QSM quantification also demonstrated a similarly greater localization of LMN into the liver under acute inflammation at different time points,

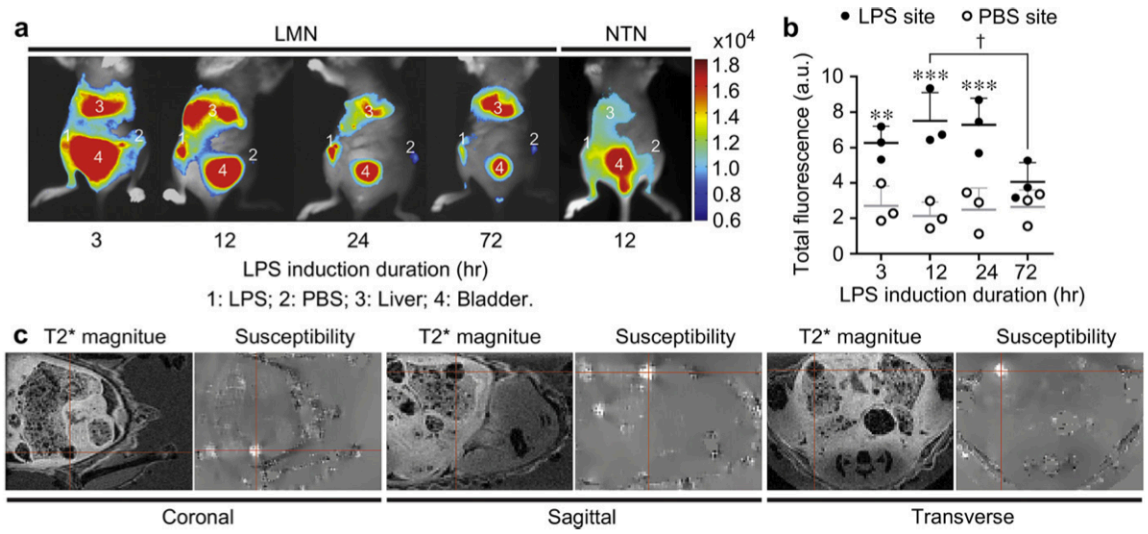


**Figure 5.** In vivo molecular imaging of subcutaneous acute inflammation using near-IR camera and MRI. (a) In vivo near-IR whole body imaging of LMN vs. NTN distribution in mice 1 h after nanoparticle injection. Mice were exposed to LPS ('1') and PBS ('2') for 3, 12, 24, or 72 h at the time of nanoparticle delivery. (b) Fluorescence intensities of LMN at LPS vs. PBS injection sites were shown (n = 3; **$p < 0.01$, ***$p < 0.001$ between LPS and PBS site at specific time points; $^{\dagger}p < 0.05$ between 12 h and 72 h at LPS site). (c) T2* magnitude and susceptibility mapping images of nanoparticle distribution in mice at 4 h after nanoparticle injection. Mice were exposed to LPS/PBS for 12 h at the time of nanoparticle injection. Bright spot identified by susceptibility mapping as the accumulation of SPIO was indicated with crosshair.

**Figure 6.** In vivo molecular imaging of systemic acute inflammation using near-IR camera and MRI. In vivo near-IR whole body imaging (a) or MRI (b) of LMN vs. NTN distribution in mice at 1, 8, 25 h post-injection of nanoparticles in mice exposed to systemic LPS for 12 h or control mice with no treatment. LMN vs. NTN distributions into the liver were quantified by near-IR optical imaging (c) and MRI (d) ($n = 3$; $*p < 0.05$, $***p < 0.001$ between LMN vs. NTN at specific time points).

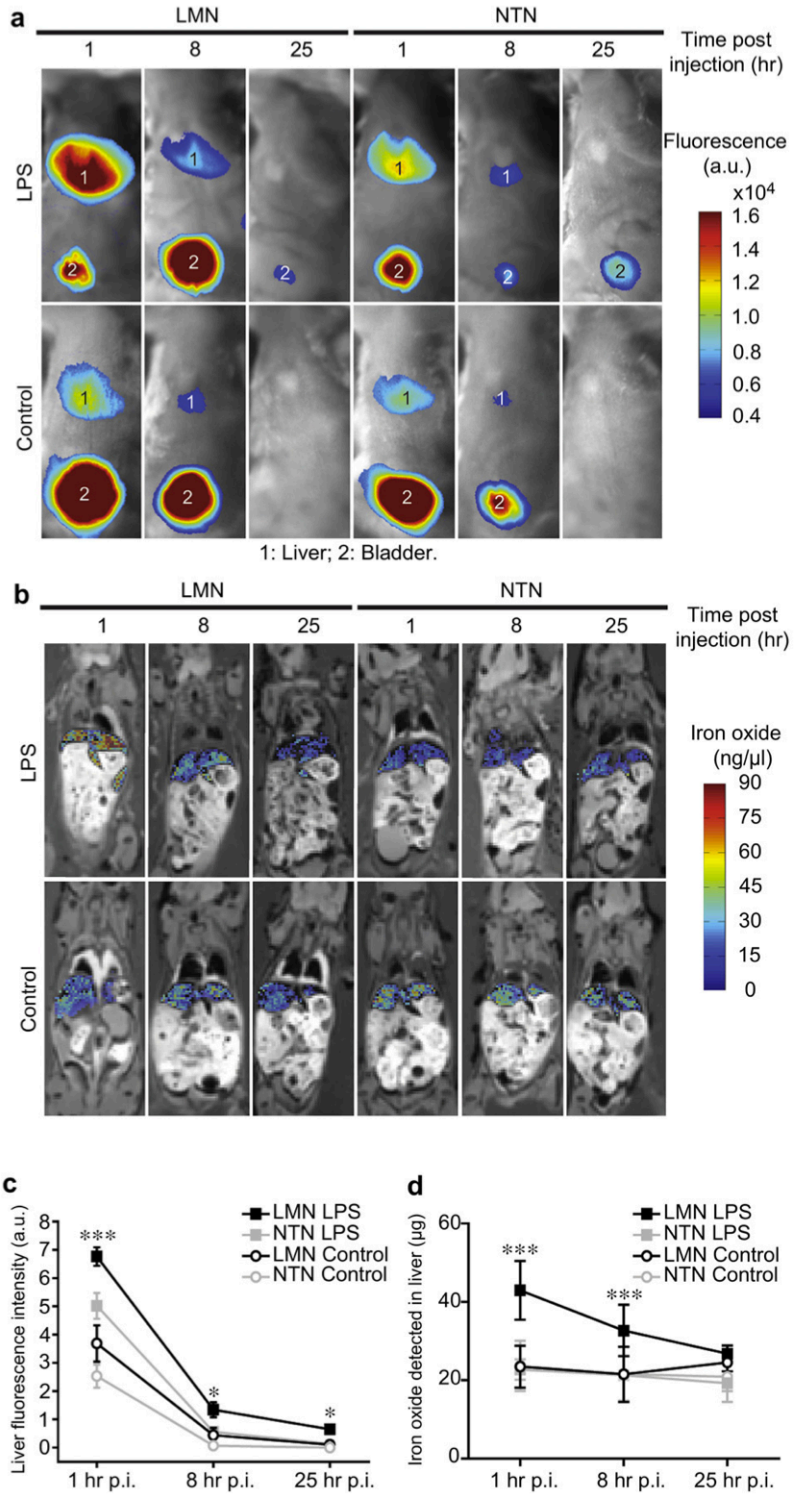
a
LMN
NTN
1
8
25
1
8
25
Time post injection (hr)
LPS
Control
Fluorescence (a.u.)
x10^4
1.6
1.4
1.2
1.0
0.8
0.6
0.4
1: Liver; 2: Bladder.
b
LMN
NTN
Time post injection (hr)
Iron oxide (ng/µl)
90
75
60
45
30
15
0
c
Liver fluorescence intensity (a.u.)
LMN LPS
NTN LPS
LMN Control
NTN Control
***
*
*
1 hr p.i.
8 hr p.i.
25 hr p.i.
d
Iron oxide detected in liver (µg)
***
***
1 hr p.i.
8 hr p.i.
25 hr p.i.

exhibiting qualitative agreement with the temporal mapping using optical imaging (Fig. 6b,d). Discrepancy between optical intensity and QSM was unavoidable as MRI was performed after perfusion of the mice as well as due to the different kinetics of degradation for fluorescence dye (AF750) and SPIO.

**Discussion**

Sensitive detection of inflammation will be of high significance for diagnosis of diseases caused directly by host inflammatory response such as sepsis, allograft rejection, lupus, as well as those that are influenced by inflammation such as cardiovascular disease and cancer. In this study, we designed MRI-compatible SPIO nanoparticles, and demonstrated a successful detection of constitutive expression of ICAM-1 in tumor, as well as ICAM-1 induction in tumor-associated vasculature, where tumor growth and angiogenesis are active. Prior approaches to inflammation detection have been largely based on antibodies that are against cell adhesion molecules such as ICAM-1 and VCAM-1 [8-13,29], lacking in the ability to fine-tune affinity and avidity of targeting moieties on nanoparticles that are critical to inflammation-specific targeting. From our previous in vitro studies [17,24], we have demonstrated specific localization into inflamed but not to resting endothelium and immune cells of nanoparticle (50-100 nm in diameter) coated with integrin LFA-1 I domain engineered for high affinity to ICAM-1. Furthermore, combining recently developed quantitative susceptibility mapping technique, we quantified sub-microgram quantity of iron oxide accumulated in both ICAM-1-expressing cell phantom in vitro and acute inflammation induced by LPS in vivo, corresponding to less than 1% of injected dose.

Despite the fact that ICAM-1 is basally expressed in all endothelium [16,23] and therefore the notion that ICAM-1 may not be a suitable target for inflammation, our studies emphasize selective delivery by targeting molecules that are induced greatly under inflammation [30,31]. Nanoparticles of ~100 nm will experience hydrodynamic force generated by the blood flow [32,33], such that there should be sufficient simultaneous molecular interactions with the cells for nanoparticles to remain on cell surface. The number of minimum molecular interactions required for stable adhesion of nanoparticles will also depend on the adhesion strength of each interaction. Therefore, specificity toward high ICAM-1 site will be influenced by the affinity of molecular interaction and the valency between nanoparticles and target cells, where the design of nanoparticles to permit tunable affinity and avidity of physiological interaction is of significant advantage. Our nanoparticles to a great extent mimic the behavior of activated leukocytes, which would adhere much better to inflamed endothelium.

Increasing number of studies has begun to focus on the crosstalk between the immune activation of vascular niche, angiogenesis, and tumor progression [34,35]. Upregulated levels of ICAM-1 in tumor have been linked to two different contexts, one serving as a marker for the recruitment of effector immune cells and tumor killing [36], while it was also observed in malignant and metastatic tumors with poor prognosis [37]. Seemingly contradicting roles of ICAM-1 may be due to the complexity of inflammation in various phases of tumor development, which can be better examined by in vivo imaging tools. Our nanoparticles did indeed show the localization into the tumor vasculature, while their localization into the vasculature elsewhere was non- detectable. With human tumor xenograft model, we observed that the majority of tumor mass was comprised of tumor cells with poor vascularity present

therein. Higher vascularity was found in the periphery of the tumor, often called the invasive tumor front, where ICAM-1 overexpression associated with higher immune activity has also been reported in many carcinoma cases [27,38-41]. Notably, we have demonstrated that intravenously injected nanoparticles targeting ICAM-1 specifically localized into the vasculature associated with the tumor progression. With further improvement of detection sensitivity in addition to more native tumor models containing not only tumor cells themselves but also fully-developed vasculatures and other stroma cells such as macrophages, our nanoparticles may provide a universal tumor imaging strategy not by tumor surface markers limited to specific cancer types but by the inflamed microenvironment which is associated with almost all cancer development.

Besides sensitive detection of chronic inflammation implicated in cancer, prompt and accurate detection of acute inflammation induced by bacterial or viral infection such as sepsis is also of clinical importance. Acute inflammation dramatically induces ICAM-1 induction not only in endothelium but also in immune cells, such that both cellular components become the targets by I domain-coated nanoparticle. Using LPS-induced acute inflammation model, we demonstrated optical imaging of the temporal dynamics of inflammation. Specific localization of LMN was also confirmed by QSM technique using MRI. The degree of localization of ICAM-1 targeting nanoparticles into an inflamed site will closely reflect different phases of inflammation, from the onset of inflammation to resolution phase. Therefore, quantitative prediction of spatiotemporal distribution of nanoparticles may provide critical information on diagnosis and the choice of therapy regimen in clinics.

In summary, our ICAM-1 targeting strategy by mimicking the behavior of leukocytes in their ability to localize to the inflamed endothelium was able to detect ICAM-1

overexpression in tumor cells, tumor vascular microenvironment, and acute inflammation. In the design of ICAM-1 targeting nanoparticles by conjugation with LFA-1 I domain, we employed His-tag binding to nickel-NTA, which we previously found [17] to be critical in order to fine-tune the coating density of targeting moieties to be specific to ICAM-1 overexpression but not to basally present ICAM-1. The idea of optimizing molecular interactions by tuning the avidity between ligands and receptors could provide a useful strategy to molecular targeting of some important targets that are basally expressed elsewhere. Inflammation-targeting nanoparticles with the lipid layer shell can also be used to carry small, hydrophobic drugs, achieving simultaneous imaging and targeted drug delivery.

**Conclusion**

This study presents physiology-inspired design of SPIO nanoparticles for in vivo detection by optical imaging and MRI, mimicking activated leukocyte in its ability to recognize inflamed endothelium. Nanoparticles in vivo will experience hydrodynamic force induced by the blood flow, requiring simultaneous molecular interactions with sufficient adhesion strength with the cells for nanoparticles to remain on cell surface. Therefore, the design of nanoparticles with tunable affinity and avidity of physiological interactions would be critical to selectivity and efficiency of leukocyte-mimetic nanoparticles in targeting inflammation. Notably, we observed specific accumulation of systemically-delivered nanoparticles into the vasculature within the tumor and invasive tumor front where the tumor growth and angiogenesis were active, while their localization into the vasculature elsewhere was much lower. The use of two different nanoparticles differed only by the type of I

domains (active vs. inactive) as targeting moieties against ICAM-1 enabled us to discriminate inflammation-driven accumulation into the tumor microenvironment from passive distribution, which may result from the leakiness of the vasculature within the tumor. Inflammation-targeting nanoparticles such as SPIO with the layer of phospholipid are also suitable for carrying small molecule drugs, achieving simultaneous imaging and targeted drug delivery.

# REFERENCES


1. Nathan C, Ding A. Nonresolving inflammation. Cell 2010;140:871-82.
2. Cohen J. The immunopathogenesis of sepsis. Nature 2002;420:885-91.
3. Glass CK, Saijo K, Winner B, Marchetto MC, Gage FH. Mechanisms underlying inflammation in neurodegeneration. Cell 2010;140:918-34.
4. Libby P. Inflammation in atherosclerosis. Nature 2002;420:868-74.
5. Hotamisligil GS. Inflammation and metabolic disorders. Nature 2006;444: 860-7.
6. Coussens LM, Werb Z. Inflammation and cancer. Nature 2002;420:860-7.
7. Mantovani A, Allavena P, Sica A, Balkwill F. Cancer-related inflammation.Nature 2008;454:436-44.
8. Sipkins DA, Gijbels K, Tropper FD, Bednarski M, Li KC, Steinman L. ICAM-1 expression in autoimmune encephalitis visualized using magnetic resonance imaging. J Neuroimmunol 2000;104:1-9.
9. Weller GE, Lu E, Csikari MM, Klibanov AL, Fischer D, Wagner WR, et al. Ultrasound imaging of acute cardiac transplant rejection with microbubbles targeted to intercellular adhesion molecule-1. Circulation 2003;108:218-24.
10. Zhang N, Chittasupho C, Duangrat C, Siahaan TJ, Berkland C. PLGA nano-particleepeptide conjugate effectively targets intercellular cell-adhesion molecule-1. Bioconjug Chem 2008;19:145-52.
11. Kelly KA, Allport JR, Tsourkas A, Shinde-Patil VR, Josephson L, Weissleder R. Detection of vascular adhesion molecule-1 expression using a novel multi-modal nanoparticle. Circ Res 2005;96:327-36.
12. Voinea M, Manduteanu I, Dragomir E, Capraru M, Simionescu M. Immunoliposomes directed toward VCAM-1 interact specifically with activated endo- thelial cellsea potential tool for specific drug delivery. Pharm Res 2005;22: 1906-17.
13. Nahrendorf M, Keliher E, Panizzi P, Zhang H, Hembrador S, Figueiredo JL, et al. 18F-4V for PET-CT imaging of VCAM-1 expression in atherosclerosis. JACC Cardiovasc Imaging 2009;2:1213-22.

14. Ehrhardt C, Kneuer C, Bakowsky U. Selectins-an emerging target for drug delivery. Adv Drug Deliv Rev 2004;56:527-49.
15. Chan JM, Zhang L, Tong R, Ghosh D, Gao W, Liao G, et al. Spatiotemporal controlled delivery of nanoparticles to injured vasculature. Proc Natl Acad Sci U S A 2010;107:2213-8.
16. Dustin ML, Rothlein R, Bhan AK, Dinarello CA, Springer TA. Induction by IL 1 and interferon-gamma: tissue distribution, biochemistry, and function of a natural adherence molecule (ICAM-1). J Immunol 1986;137:245-54.
17. Kang S, Park T, Chen X, Dickens G, Lee B, Lu K, et al. Tunable physiologic interactions of adhesion molecules for inflamed cell-selective drug delivery. Biomaterials 2011;32:3487-98.
18. Jin M, Song G, Carman CV, Kim YS, Astrof NS, Shimaoka M, et al. Directed evolution to probe protein allostery and integrin I domains of 200,000-fold higher affinity. Proc Natl Acad Sci U S A 2006;103:5758-63.
19. Liu T, Spincemaille P, de Rochefort L, Kressler B, Wang Y. Calculation of susceptibility through multiple orientation sampling (COSMOS): a method for conditioning the inverse problem from measured magnetic field map to susceptibility source image in MRI. Magn Reson Med 2009;61:196-204.
20. Wharton S, Schafer A, Bowtell R. Susceptibility mapping in the human brain using threshold-based k-space division. Magn Reson Med 2010;63: 1292-304.
21. Weber C, Fraemohs L, Dejana E. The role of junctional adhesion molecules in vascular inflammation. Nat Rev Immunol 2007;7:467-77.
22. Shimaoka M, Lu C, Palframan RT, von Andrian UH, McCormack A, Takagi J, et al. Reversibly locking a protein fold in an active conformation with a disulfide bond: integrin alphaL I domains with high affinity and antagonist activity in vivo. Proc Natl Acad Sci U S A 2001;98:6009-14.
23. Marlin SD, Springer TA. Purified intercellular adhesion molecule-1 (ICAM-1) is a ligand for lymphocyte function-associated antigen 1 (LFA-1). Cell 1987;51: 813-9.
24. Park S, Kang S, Veach AJ, Vedvyas Y, Zarnegar R, Kim JY, et al. Self-assembled nanoplatform for targeted delivery of chemotherapy agents via affinity- regulated molecular interactions. Biomaterials 2010;31:7766-75.

25. Dubertret B, Skourides P, Norris DJ, Noireaux V, Brivanlou AH, Libchaber A. In vivo imaging of quantum dots encapsulated in phospholipid micelles. Science 2002;298:1759-62.
26. Kelly CP, O'Keane JC, Orellana J, Schroy 3rd PC, Yang S, LaMont JT, et al. Human colon cancer cells express ICAM-1 in vivo and support LFA-1-dependent lymphocyte adhesion in vitro. Am J Phys 1992;263:G864-70.
27. Maurer CA, Friess H, Kretschmann B, Wildi S, Muller C, Graber H, et al. Over-expression of ICAM-1, VCAM-1 and ELAM-1 might influence tumor progres- sion in colorectal cancer. Int J Cancer 1998;79:76-81.
28. Hayes SH, Seigel GM. Immunoreactivity of ICAM-1 in human tumors, metastases and normal tissues. Int J Clin Exp Pathol 2009;2:553-60.
29. Reinhardt M, Hauff P, Linker RA, Briel A, Gold R, Rieckmann P, et al. Ultrasound derived imaging and quantification of cell adhesion molecules in experimental autoimmune encephalomyelitis (EAE) by Sensitive Particle Acoustic Quantification (SPAQ). Neuroimage 2005;27:267-78.
30. Osborn L. Leukocyte adhesion to endothelium in inflammation. Cell 1990; 62:3-6.
31. Springer TA. Adhesion receptors of the immune system. Nature 1990;346: 425-34.
32. Shi W, Wang J, Fan X, Gao H. Size and shape effects on diffusion and absorption of colloidal particles near a partially absorbing sphere: implica- tions for uptake of nanoparticles in animal cells. Phys Rev E Stat Nonlin Soft Matter Phys 2008;78. 061914.
33. Mailander V, Landfester K. Interaction of nanoparticles with cells. Bio-macromolecules 2009;10:2379-400.
34. Rajashekhar G, Willuweit A, Patterson CE, Sun P, Hilbig A, Breier G, et al. Continuous endothelial cell activation increases angiogenesis: evidence for the direct role of endothelium linking angiogenesis and inflammation. J Vasc Res 2006;43:193-204.
35. Franses JW, Baker AB, Chitalia VC, Edelman ER. Stromal endothelial cells directly influence cancer progression. Sci Transl Med 2011;3. 66ra5.

36. Pandolfi F, Trentin L, Boyle LA, Stamenkovic I, Byers HR, Colvin RB, et al. Expression of cell adhesion molecules in human melanoma cell lines and their role in cytotoxicity mediated by tumor-infiltrating lymphocytes. Cancer 1992; 69:1165-73.
37. Kobayashi H, Boelte KC, Lin PC. Endothelial cell adhesion molecules and cancer progression. Curr Med Chem 2007;14:377-86.
38. Nelson H, Ramsey PS, Donohue JH, Wold LE. Cell adhesion molecule expres- sion within the microvasculature of human colorectal malignancies. Clin Immunol Immunopathol 1994;72:129-36.
39. Fox SB, Turner GD, Leek RD, Whitehouse RM, Gatter KC, Harris AL. The prognostic value of quantitative angiogenesis in breast cancer and role of adhesion molecule expression in tumor endothelium. Breast Cancer Res Treat 1995;36:219-26.
40. Suzuki Y, Ohtani H, Mizoi T, Takeha S, Shiiba K, Matsuno S, et al. Cell adhesion molecule expression by vascular endothelial cells as an immune/ inflammatory reaction in human colon carcinoma. Jpn J Cancer Res 1995;86: 585-93.
41. Cianchi F, Cuzzocrea S, Vinci MC, Messerini L, Comin CE, Navarra G, et al. Heterogeneous expression of cyclooxygenase-2 and inducible nitric oxide synthase within colorectal tumors: correlation with tumor angiogenesis. Dig Liver Dis 2010;42:20-7.

# CHAPTER 4

# VIRUS-MIMETIC POLYPLEX PARTICLES FOR SYSTEMIC AND INFLAMMATION-SPECIFIC TARGETED DELIVERY OF LARGE GENETIC CONTENTS


## Abstract

Systemic and target-specific delivery of large genetic contents has been difficult to achieve. Although viruses effortlessly deliver kilobase-long genome into cells, its clinical use has been hindered by serious safety concerns and the mismatch between native tropisms and desired targets. Nonviral vectors, in contrast, are limited by low gene transfer efficiency and inherent cytotoxicity. Here we devised virus-mimetic polyplex particles (VMPs) based on electrostatic self-assembly among polyanionic peptide (PAP), cationic polymer polyethyleneimine (PEI) and nucleic acids. We fused PAP to the engineered ligand-binding domain of integrin aLb2 to target intercellular adhesion molecule-1 (ICAM-1), an inducible marker of inflammation. Fully assembled VMPs packaged large genetic contents, bound specifically to target molecules, elicited receptor-mediated endocytosis and escaped endosomal pathway, resembling intracellular delivery processes of viruses. Unlike conventional PEI-mediated transfection, molecular interaction- dependent gene delivery of



This chapter is modified and reprinted from, Kang S, Lu K, Leelawattanachai J, HuX, Park S, Park T, Min IM, and Jin MM. Virus-mimetic polyplex particles for systemic and inflammation-specific targeted delivery of large genetic contents. Gene Therapy 2013;20:1042-1052, with permission from the publisher. Leelawattanachai J developed and optimized the conditions for homogenous electrostatic self-assembly of VMPs, performed validation assays, and wrote the manuscript related to the assembly method and validation.

VMPs was unaffected by the presence of serum and achieved higher efficiency without toxicity. By targeting overexpressed ICAM-1, VMPs delivered genes specifically to inflamed endothelial cells and macrophages both in vitro and in vivo. Simplicity and versatility of the platform and inflammation-specific delivery may open up opportunities for multifaceted gene therapy that can be translated into the clinic and treat a broad range of debilitating immune and inflammatory diseases.

## Introduction

Viruses have evolved ways to efficiently deliver their genetic materials into cells that can be as large as multiples of kilobase-long nucleic acids. The use of viral gene delivery vectors for clinical applications [1–5], however, poses serious safety issues, including pathogenicity by insertional mutagenesis [6] and anaphylactic response to the virus [7, 8]. On the other hand, synthetic nonviral vectors suffer from inherent cytotoxicity and are severely limited due to low gene transfer efficiency in systemic parenteral applications. Particularly, cationic nonviral vectors, which can disrupt the integrity of plasma membrane during entry into cells [9, 10], are easily inactivated by negatively charged molecules such as glycosaminoglycans in circulation [11–13].

To achieve cell type- or cell state-specific targeted systemic delivery, it often requires the use of complex molecules such as antibodies and proteins that specifically bind to target molecules. However, systemic site-directed delivery of large nucleic acid molecules has met limited success. In fact, studies have been mostly constrained to the delivery of small nucleic acids, such as siRNA [14–17]. Although viruses possess the ability to overcome many

barriers of gene delivery such as cell entry through the membrane and escape from lysosomal nuclease degradation, engineering the tropism of viral vectors for site-directed delivery to a range of different targets [18–20] has been challenging. Nonviral vectors are capable of delivering large content of nucleic acids such as plasmids, but modifications to confer specific targeting have been mostly confined within chemical/covalent attachments of small molecules [21], peptides [22] and several types of proteins [23, 24], which would inevitably affect the original physicochemical properties of the vectors.

In this study, we devised a polyanionic peptide (PAP) comprised of 18 randomly ordered glutamic and aspartic acids that can be expressed as a fusion to proteins to mediate electrostatic attachment to cationic transfection agents. Polyethyleneimine (PEI) was used as a scaffold to hold both a large content of nucleic acid and PAP-fused targeting moieties. PEI has been extensively studied as a cationic polymer-mediated gene delivery agent and has been considered to have relatively high gene transfer efficiency [25–29]. PEI has all primary, secondary and tertiary amines, providing buffering capacity at low pH of late endosomes [30]. This promotes an influx of counter-ions such as chloride [31], raising osmotic pressure that eventually bursts the vesicles and releases nucleic acid payload, which has been termed as the proton sponge effect [32].

To achieve targeted gene delivery to inflammatory diseases, we fused the PAP to the major ligand-binding domain (I domain) of integrin lymphocyte function-associated antigen-1 (LFA-1; aLb2) as a targeting moiety. The physiological counter receptor for LFA-1 is the intercellular adhesion molecule-1 (ICAM-1), which is highly expressed on inflamed cell surfaces [33, 34] that often colocalizes at various disease sites [35, 36]. ICAM-1 is also subverted as a receptor for the major human rhinoviruses (HRVs) [37], which gain cell entry

by multivalent interaction with ICAM-1 that promotes rapid endocytosis [38, 39]. We have previously engineered the I domain into a high-affinity (HA) mutant to ICAM-1 by directed evolution [40]. The I domain is a globular Rossmann fold protein of approximately the size of a single-chain variable- fragment antibody. We previously used the HA I domain as a targeting moiety for various types of carriers to deliver drugs [41, 42] and imaging contrast agents [43] specifically to inflamed endothelial cells and immune cells, and to cancer cells and their stroma.

Here we show that, by fusing the PAP to the I domain (PAP-Id) and using a cationic nonviral vector PEI, we were able to establish a molecular interaction-dependent gene delivery platform based on their stepwise electrostatic self-assembly, which creates virus-mimetic polyplex particles (VMPs) that mimic the processes involved in virus infection. Similarly as to how cell entry is gained by HRVs, our VMPs were also able to mediate cellular endocytosis by clustering ICAM-1 via multivalent binding of the I domains. Because the attachment of targeting moieties is a self-assembling process, we were able to precisely control the moiety density or avidity, optimal for efficient endocytosis and gene transfer. Not only did the association of DNA and PEI particles with PAP-Id reduce the inherent cytotoxicity of PEI, it also enabled the delivery to be unaffected by the presence of serum. Similarly as acid-catalyzed conformational change in HRV capsid leads to penetration of the membrane, VMPs escaped endosomal degradation and led to efficient gene expression. Moreover, by targeting ICAM-1, we were able to deliver genes specifically to inflamed endothelial cells and immune cells both in vitro and systemically in vivo.

## Materials And Methods

*Cell culture conditions*

HeLa, bEnd.3, RAW 264.7 (ATCC, Manassas, VA, USA) and primary mouse lung cells were cultured in Advanced Dulbecco's modified Eagle's medium (Invitrogen, Carlsbad, CA, USA) containing 2 mM L-glutamine, Pen-step (100 units/ml penicillin and 100 μg/ml streptomycin) and 10% fetal bovine serum (FBS; endotoxin free, PAA Laboratories, Piscataway, NJ, USA). Primary mouse lung cells were harvested from fetus lungs of mouse strain Gt(ROSA)26Sor$^{tm4(ACTB-tdTomato,-EGFP)Luo}$ (Jackson Laboratory, Bar Harbor, ME, USA). Lungs were aseptically minced and digested in 1 mg/ml collagenase A (Roche, Basel, Germany) for 3 h at 37 °C, which were then filtered through 70-μm nylon mesh cell strainer and washed twice in complete media for culture. HMEC-1 (Center for Disease Control, Atlanta, GA, USA) was propagated in MCDB 131 medium (Invitrogen) supplemented with 10% FBS, 10 mM L-glutamine, Pen-strep, 1 μg/ml hydrocortisone (MP Biomedicals, Solon, OH, USA) and 10 ng/ml human epidermal growth factor (Invitrogen). THP-1 cells (ATCC) were cultured in RPMI 1640 medium (Invitrogen) with 10% FBS and Pen-strep. Endothelial cells and primary mouse lung cells were trypsinized at confluency and washed to remove residual trypsin before plating. All mammalian cells were maintained at 37 °C in a 5% $CO_2$ humidified incubator.

*Protein construction, design, and purification*

Wild-type LFA-1 I domain sequence (Asn-129 to Tyr-307) followed by a stop codon was subcloned into pET28a vector (Novagen, Madison, WI, USA) between BamH1 and

Xho1. QuickChange (Stratagene, La Jolla, CA, USA) site-directed mutagenesis was used to create F265S/F292G and D137A mutants. For GFP-Id, a superfolder GFP was inserted between Nhe1 and BamH1. To construct PAP-Id, complementary primers encoding 50 -ctagcgaggatgaagatgaggaagacgaagaagatgaagaggacgaagaggacgaggatg-30 and 50 -gatccatcctcgtcctcttcgtcctcttcatcttcttcgtcttcctcatcttcatcctcg-30 were annealed and directly ligated between Nhe1 and BamH1. Constructs were transformed into Escherichia coli, BL21 (DE3) cells (Novagen) for production of the fusion proteins. Overnight starter culture was used to inoculate a larger Luria Bertani medium at 1:40 volume ratio and was grown at 37 °C to OD600 of 0.4–0.5 (~2 h). Then cells were induced with freshly prepared 1 mM isopropyl-b-D-thiogalactopyranoside at 25 °C overnight (~15 h). Cells were recovered by centrifugation and sonicated in buffer A (50 mM $NaH_2PO_4$, 300 mM NaCl, 10 mM imidazole, protease inhibitor cocktail (ProteCEASE-EDTA free, G-Biosciences, St. Louis, MO, USA)) with pH adjusted to 8.0 for GFP-Id and 6.0 for PAP-Id. Soluble fraction of GFP-Id was purified by passage over a Ni-NTA column (Pierce, Rockford, IL, USA). Insoluble fraction of PAP-Id was washed in buffer A with four cycles of sonication and super-centrifugation at 20,000 g for 30 min. Protein pellet was then solubilized in buffer B (buffer A plus 6 M guanidine HCl, pH 8.0) and purified by Ni-NTA. GFP-Id and PAP-Id were washed in buffer C (50 mM $NaH_2PO_4$, 300 mM NaCl, 20 mM imidazole, pH 8.0) and then eluted in buffer D (50 mM $NaH_2PO_4$, 300 mM NaCl, 250 mM imidazole, pH 8.0). Eluted proteins were then subjected to gel filtration chromatography using Superdex S200 column in phosphate-buffered saline (PBS) connected to AKTA Purifier (GE Healthcare, Pittsburgh, PA, USA).

*Electrostatic self-assembly of VMPs*

For any given mass ratios, plasmid and PEI (branched, MW 25,000, Sigma- Aldrich, St. Louis, MO, USA) were each diluted in one volume of PBS (pH 7.4) and PAP-Id in two volumes of PBS. Solutions containing plasmid and PEI were first vortex mixed and incubated at room temperature for 40 min. Plasmid/PEI mixture was then gently mixed with PAP-Id solution and incubated at room temperature for 40 min. Vector for GFP expression (pGFP) was constructed by subcloning a complete Kozak consensus sequence and enhanced GFP sequence followed by a stop codon between EcoRI and BglII of pAAV-MCS vector (AAV Helper-Free System, Agilent Technologies, Santa Clara, CA, USA). Vectors for expression of diphtheria toxin A (pDTA) and Cre recombinase (pCRE) were obtained from Addgene (Cambridge, MA, USA), originally named as PGK-DTA-bpA (plasmid 13440) and pLOX-CW-CRE (plasmid 12238), respectively. All components used for assembly of VMPs, including plasmids, PAP-Id, PEI and PBS, were filter sterilized through 0.2-μm centrifugal or syringe filters before assembly.

*Dynamic light scattering and zeta-potential measurements of VMPs*

The size distribution and zeta-potential of VMPs were determined using Zetasizer Nano ZS (Malvern Instruments (Malvern, Worcestershire, UK)). VMPs prepared with 1 μg of plasmid and the relative mass of PEI and/or PAP-Id were each diluted in 750 μl of PBS (pH 7.4). The solution was added to the cell and the measurements were carried out at 25 °C.

*In vitro delivery of VMPs*

Cells were grown in 24-well plates to confluence and pretreated with complete media containing 1 μg/ml of LPS (E. coli, 026:B6, Sigma) to induce inflammation. Each well received VMPs prepared with 0.4 μg of plasmid and the relative mass and volumes of PEI and PAP-Id. Final VMPs were then mixed with an equal volume of FBS and incubated at room temperature for 40 min before delivery to cells. After delivery, cells were washed twice with media, followed by addition of fresh complete media.

*In vivo delivery of polyplex particles*

Eight-to-ten-week-old female BALB/c mice (Jackson Laboratory) were used. All administrations performed in this study were given intravenously, using 29G × 0.5" insulin syringes via lateral tail vein route injections. To induce systemic inflammation, 20 μg per mouse of LPS (E. coli, 026:B6, Sigma) in PBS (pH 7.4) was injected. VMPs bearing 5 μg of plasmid was formed in a mass ratio of the components (plasmid:PEI:PAP-Id) fixed to 1:6:16 in a final volume of 200 μl. All animal procedures were approved by the Cornell University IACUC and were conducted in accordance with recommendations in the Guide for the Care and Use of Laboratory Animals published by the National Institutes of Health.

*Immunofluorescence for imaging and flow cytometric analysis*

Mean fluorescence intensity and percentage of GFP-positive cells were quantified by flow cytometry (Beckman Coulter EPICS XL-MC, Brea, CA, USA). After in vitro delivery of VMPs for GFP expression, cells were trypsinized, washed with washing buffer (PBS, 0.5% bovine serum albumin, pH 7.4) and subjected to flow cytometer. Total fluorescence was quantified by lysing cells with 1% (v/v) Triton X-100 in PBS and measuring with a

fluorescence plate reader Infinite M1000, TECAN (Männedorf, Switzerland). Confocal microscopy (Zeiss LSM 710, Zeiss (Oberkochen, Germany)) was used to assess endocytosis of VMPs and protein expression in HeLa cells. PAP-Id was conjugated to Alexa Fluor 555 (succinimidyl ester, Invitrogen) and pGFP was labeled with Cy5 (Label IT Nucleic Acid Labeling Kit, Mirus Bio (Madison, WI, USA)). HeLa cells were grown in 35mm glass bottom dishes (0.16–0.19 mm cover glass, In Vitro Scientific (San Jose, CA, USA)) and fixed in 3.7% formaldehyde for 1 h at different time points after delivery of fluorescently labeled VMPs. Expression of ICAM-1 in mouse lungs were assessed by GFP-Id. Lungs were collected at different time points after systemic LPS treatment (20mg per mouse, E. coli, 026:B6, Sigma) and were minced and digested in 1 mg/ ml collagenase A (Roche) for 3 h at 37 °C. Singlet lung cells were prepared by passage through 70-μm nylon mesh cell strainer and incubation with red blood cell lysis buffer (eBiosciences, San Diego, CA, USA) for 5 min on ice. Cells were then washed and labeled for ICAM-1 with 10 μg/ml GFP-Id in ice-cold labeling buffer (PBS, 0.5% bovine serum albumin, 10 mM $MgCl_2$, pH 7.4) for 1 h. Cells were then labeled with either rat IgG anti-mouse CD31 (1:20, BD Pharmingen, San Diego, CA, USA) or rat IgG anti-mouse F4/80 (1:50, Abcam, Cambridge, UK) for 1 h, followed by goat anti-rat IgG-PE (Santa Cruz, Santa Cruz, CA, USA) as secondary antibody for 1 h. For detection of GFP expression after delivery of VMPs bearing pGFP, singlet lung cells were fixed with 3.7% formaldehyde for 1h and permeabilized with 1% (v/v) Triton X-100 for 30 min. Permeabilized cells were then labeled with rabbit IgG anti-GFP antibody (1:20, Invitrogen) for 1h, followed by goat anti-rabbit IgG-PE (1:100, Santa Cruz) for 1h. Cells were then labeled for CD31 and F4/80 similarly as described, followed by goat anti-rat IgG-FITC (1:100, Santa Cruz) for 1h.

*Real-time quantitative PCR*

Total RNAs from harvested lungs were extracted using TRI Reagent (Ambion, Austin, TX, USA). Briefly, mouse lung tissue (~150mg) was homogenized in 1 ml of TRI Reagent solution followed by brief sonication. Homogenized lysates were mixed with 200 µl chloroform and centrifuged at 12,000 g for 15 min. In all, 400 µl of colorless upper aqueous phase was collected and mixed with 500 µl isopropanol and loaded to spin columns (Zymo-Spin II, Zymo Research, Irvine, CA, USA). Eluted RNA (1µg) was converted to cDNA using a reverse transcription kit (High Capacity cDNA RT kits, Applied Biosystems, Foster City, CA, USA) in a thermal cycler (GeneAmp PCR System 2700, Applied Biosystems). Real-time gene amplification analysis (MyiQ iCycler, Bio-Rad) was performed using a quantitative PCR kit (Sybr Green 2 × Master Mix, Bio-Rad, Hercules, CA, USA) to measure gene expression of GFP relative to CYC1 housekeeping gene. Primers for GFP were previously reported and for CYC1 (NM_025567) were obtained from Mouse qPrimerDepot of the National Cancer Institute.

*Quantification of cell viability*

Cell viability of HeLa cells treated with VMPs bearing pDTA was analyzed by trypan blue exclusion test. Cells were incubated with 0.2% trypan blue for 5 min, and microscopic images were taken at random places of culture wells. Viable cells that excluded trypan blue and nonviable cells with blue cytoplasm were counted per given image field for analysis. Viability measurements presented in Figures 3–5 were quantified by MTT (3-(4,5-dimethylthiazol-2-yl)-2,5-diphenyltetrazolium bromide) assay. Cells were incubated with

basal media containing 0.5 mg/ml MTT for 4 h at 37 °C. Blue formazan products were solubilized in dimethyl sulfoxide and quantified by absorbance at 570 nm.

*Statistical analysis*

Data were expressed as mean ± s.d. of at least quadruplicate samples. Statistical analysis of data was carried out using GraphPad Prism 5; GraphPad Software Inc. (La Jolla, CA, USA). Unpaired Student's t-test was used to determine statistical significance in comparison to matching controls. One-way analysis of variance was used to compare mean responses among the different groups, followed by Tukey's post-hoc test to determine statistical significance.

**Results**

*Molecular interaction-specific VMPs for targeted gene delivery*

VMPs were designed to mimic the components of non-enveloped viruses (for example, HRVs) and their entry into a specific range of host cells (Figure 1a). VMPs were assembled in a sequential manner: first PEI and DNA plasmids were mixed together, to which proteins were added. The ratio of protein, DNA, and PEI was adjusted so that unsaturated positive charges in PEI would assemble with the negatively charged residues (PAP) and DNA (Figure 1b). When added to cells with ICAM-1 expression, VMPs that were assembled with integrin LFA-1 I domain would cluster ICAM-1 and trigger the cells for endocytosis. A decrease in pH in late endosomes would increase the degree of protonation in PEI, whereby it attracts counter-ions and bursts the vesicle by proton sponge effect [31, 32].

Escaped plasmid payloads are then transported into the nucleus and leads to the expression of encoding genes.

To visualize VMPs throughout the processes of cell entry, endosomal escape and gene expression, we fluorescently labeled plasmids and PAP-Id to track the particles by confocal microscopy. We used the I domain engineered for HA with double mutations F265S/F292G [40] (denoted as PAP-Id(HA)). We used a plasmid encoding enhanced green fluorescent protein (GFP) under cytomegalovirus promoter (denoted as pGFP). VMPs were constructed using Cy5-labeled pGFP and Alexa Fluor 555-conjugated PAP-Id(HA) at a mass ratio determined to be within an optimal range for delivery (1:6:16 for pGFP:PEI:PAP-Id(HA); see Figure 2). We then delivered the fluorescently labeled VMPs in the presence of serum to HeLa cells, which express a high level of ICAM-1. Cells were fixed at 3, 24 and 48 h after delivery. At 3 h post delivery, VMPs were found mostly inside cells, confirmed by confocal microscopy (Figures 1c and d). PAP-Id(HA) (red) and pGFP (blue) appeared to be in complex with each other, evidenced by colocalization of the two in the merged image. At 24 h post delivery, some cells began to express GFP, which coincided with the observation that the components of VMPs appeared to be dissociated from each other. At 48 h, most cells expressed GFP, while much of the components of VMPs were no longer detectable. PEI/DNA plasmids polyplex without the I domain (PEI:pGFP = 6:1 w/w) exhibited a size of 169 nm and a zeta potential of + 26 mV. With the addition of the I domain (PEI:eGFP:I domain = 6:1:12), VMPs increased in size (245.5 nm) but displayed a reduced zeta potential ( + 20 mV), presumably due to the presence of negatively charged peptides (PAP) fused to the I domains.

**Figure 1.** Cell entry, endosomal escape and gene expression of polyplex particles. (a) HRV gains cell entry by binding and clustering ICAM-1, which is overexpressed on inflamed cell surfaces. Acid-catalyzed conformational change in the viral capsid (violet) penetrates the membrane of late endosomes, through which it releases the RNA genome that leads to the synthesis of more viruses (green). (b) Self-assembly of VMPs is mediated by stepwise electrostatic interactions among negatively charged nucleic acids, positively charged PEI and PAP-Id. VMPs similarly gain cell entry by multivalent ICAM-1 clustering-mediated endocytosis. A decrease in pH in late endosomes protonates PEI, attracting counter-ions ($Cl^-$) and exerting osmotic pressure and eventually bursting the vesicle. Plasmid payloads that escaped endosomal nuclease degradation are then transported into the nucleus through the nuclear pore complex (NPC), leading to the expression of encoding genes. (c–e) Confocal microscopy was used to track intracellular localization of PAP-Id(HA) (high affinity) conjugated to Alexa Fluor 555 (red), pGFP labeled with Cy5 (blue) and GFP expression (green) in HeLa cells. (c) VMPs were self-assembled at its optimal mass ratio of pGFP:PEI:PAP-Id(HA) adjusted to 1:6:16. Cells received VMPs in the presence of serum, which then were fixed at time points of 3, 24 and 48 h after delivery. Colocalization of red and blue appears in magenta in merged image. Focal plane was set through the middle of cells to capture VMPs inside cells. Dotted lines mark the cell boundaries. Bar = 20 μm. (d) Z-stack confocal images also show localization of VMPs inside HeLa cells at 3, 24 and 48h after delivery. Dotted lines indicate the top surface of cells. Bar = 10 μm. (e) Similarly, confocal images were taken at 3 h post delivery to assess the uptake of control particles (formed with PEI and PAP-Id(HA), PAP-Id(HA) and pGFP or PEI and pGFP). Note that focal plane for imaging was set through the middle of cells to visualize only the particles

internalized into cells. Bar = 50 µm. (f ) Fluorescence microscope images (top view) of HeLa cells at 3 h post delivery are shown (imaged without fixation). PAP-Id(HA), conjugated to Alexa Fluor 555 for fluorescent detection, was either assembled with only plasmid or with PEI and plasmid. The particles were incubated with HeLa cells in the presence of serum. Bar = 50 µm.

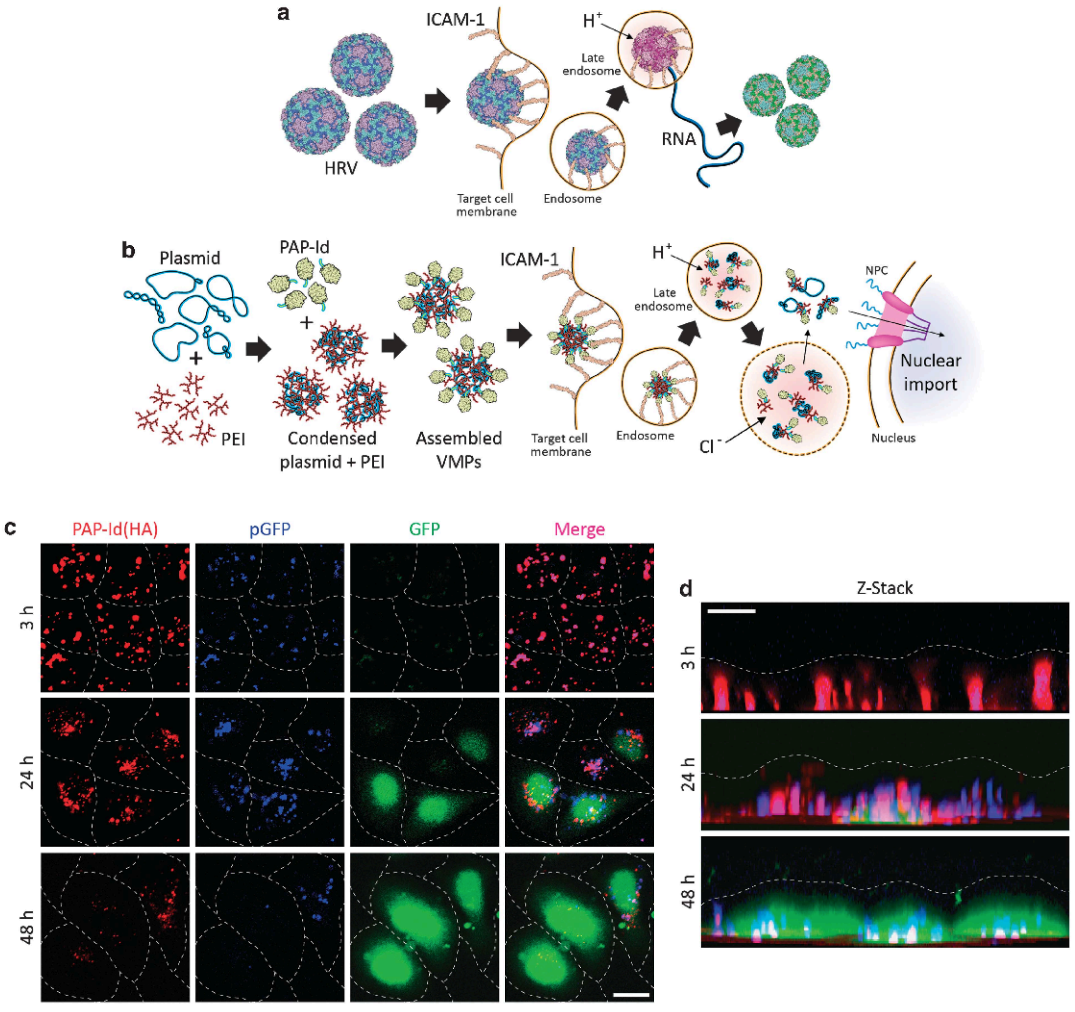

Fig. 1 (continued)

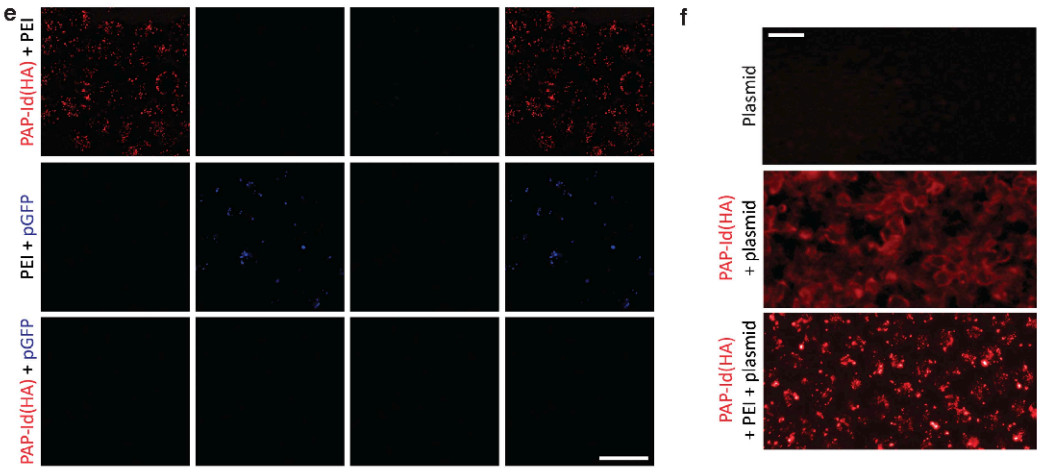


To show that all three components are necessary for gene delivery by VMPs, we assembled fluorescently labeled particles with one component omitted (that is, PAP-Id(HA)/PEI, PEI/pGFP, and PAP-Id(HA)/pGFP) and delivered to HeLa cells in the presence of serum (Figure 1e). At 3 h post delivery, the particles that were formed without pGFP (that is, PAP-Id(HA)/PEI) were found as small vesicles inside the cells but to a lesser extent than fully assembled VMPs. Particles that were assembled without PAP-Id(HA) (that is, PEI/pGFP) were sparsely found inside the cells. The mixture without PEI (that is, PAP-Id(HA)/pGFP), where PAP-Id(HA) would not associate with pGFP and remain as monomers, were not found inside the cells (Figure 1e). In order to show that clustering of ICAM-1 is necessary for internalization of particles by the cells, we imaged cells without fixation under conventional fluorescence microscopy (Figure 1f). The mixture of PAP-Id(HA)/plasmid was indeed smoothly distributed over the cell surfaces, which was in contrast to fully assembled VMPs appearing as endocytosed intracellular speckles (Figure 1f). As a negative control for

the HA I domain, we used the PAP-fused I domain containing a loss-of- function mutation D137A [44] (denoted as PAP-Id(D137A)). Particles that were assembled with Id(D137A) were neither observed on the cell surface nor inside the cells, proving that it is ICAM-1-mediated internalization by which our VMPs were delivered inside the cells (images and functional data shown throughout Figures 2–6).

*Determining optimal ratios of protein, DNA and PEI for efficient gene delivery*

In an effort to assemble VMPs for the highest gene transfer efficiency, we varied the mass ratios of individual components and examined the efficiency of gene expression (Figure 2). With a fixed amount of pGFP, we varied the amount of PEI ranging from 3 to 8 mass ratios of PEI to plasmids. To the mixture of pGFP/PEI particles, PAP-Id(HA) or PAP-Id(D137A) were added at mass ratios varying from 2 to 32 of proteins to plasmids (Figure 2a). Assembled VMPs were delivered to HeLa cells in the presence of serum. As additional controls and for comparison to conventional transfection methods, pGFP/PEI particles were used without proteins, both with and without serum (Figure 2a). Gene transfer efficiency was assessed by two different assays, that is, total fluorescence measured from cell lysates, and mean fluorescence intensity and the percentage of GFP-positive cells measured by flow cytometry. Overall, VMPs formulated with the mass ratios of 8–16-fold excess of PAP-Id(HA) and 5–7-fold excess of PEI over pGFP led to the highest readouts of total fluorescence and a percentage of GFP-positive cells (Figure 2a). Higher than optimal ratios of I domains mixed with pGFP/PEI resulted in a decrease in delivery efficiency due to the inhibition of VMP binding to cells by free I domains occupying available ICAM-1 on cell surface. Although VMPs assembled with PAP-Id(HA) produced over 80% GFP-positive

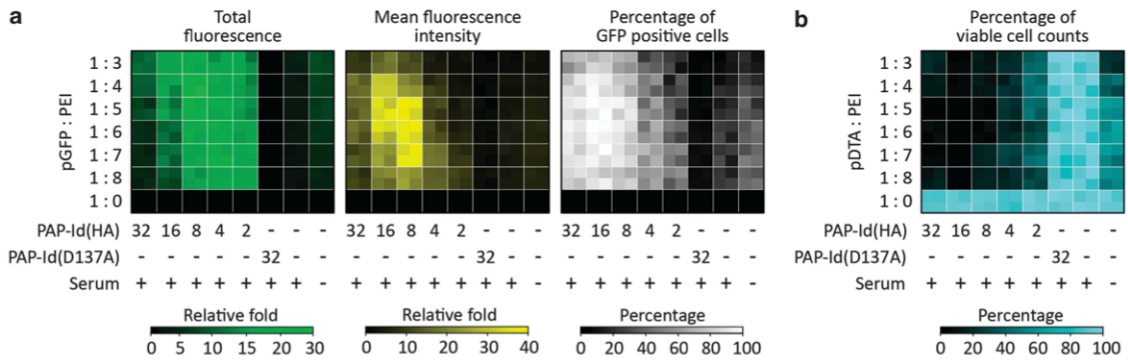


**Figure 2.** Molecular interaction-specific gene delivery of VMPs. (a, b) VMPs were assembled with varying mass ratios among the three components: pGFP, PEI and PAP-Id. The mass ratio of plasmid to PEI was titrated from 1:3 to 1:8, which were then assembled with various mass ratios of PAP-Id(HA) to probe optimal gene transfer efficiency. PAP-Id(D137A) (no affinity) was used as a negative control as the loss-of-function point mutation abrogates the interaction with ICAM-1. (a) Heatmap in green shows the total fluorescence measured by a fluorescence microplate reader after cell lysis (n = 4), in yellow shows the mean fluorescence intensity measured by flow cytometry (n = 4) and in white is the percentage of GFP-positive cells as compared with non-transfected control cells (n = 4). Fluorescence values are shown in relative fold difference compared with the negative control, of which the particles were assembled without PEI. (b) VMPs bearing pDTA (diphtheria toxin subunit A) were delivered to HeLa cells in a similar manner. Heatmap in cyan shows the percentage of viable cells counted per image field (n = 4) relative to untreated normal HeLa cells. Trypan blue exclusion assay was used to stain nonviable cells and exclude those from the counts.

cells and total fluorescence as high as 20-fold over the mixture of PAP-Id(HA)/pGFP, VMPs assembled with PAP-Id(D137A) did not show any sign of GFP expression. Particles assembled without the I domains, a formulation identical to conventional PEI-based transfection method, overall resulted in much lower GFP expression compared with VMPs. Furthermore, the addition of serum almost completely abolished GFP expression induced by conventional PEI-based transfection (Figure 2a).

To demonstrate ICAM-1-specific delivery of functional genes, we assembled the particles with a plasmid encoding a catalytic domain (subunit A) of diphtheria toxin without the other two domains responsible for receptor-binding and endosomal escape [45] (pDTA). This would limit a potent cell killing only to the transfected cells but not to the neighboring non-transfected cells. Cell death mediated by pDTA-encapsulating VMPs would thus indicate that our delivery system was able to compensate for the functions provided by the other two missing domains: cell binding/entry and endosomal escape. Potent cytotoxicity in HeLa cells was evident at similar mass ratios found to be optimal for the delivery of pGFP (Figure 2b). In contrast to highly efficient and ICAM-1-dependent cell killing by PAP-Id(HA)-mediated delivery, pDTA/PEI particles in the presence of serum and the VMPs assembled with PAP-Id(D137A) were completely ineffective in causing cell death. Altogether, these assays provided evidence that Id(HA), but not PEI, was responsible for specific targeting of ICAM-1 and cell entry of VMPs.

*Inflammation-specific gene delivery to endothelial cells and monocytes/macrophages*

Major cellular culprits of inflammatory diseases [46, 47] are endothelial cells that line the luminal surface of blood vessels and immune cells that actively elicit immune responses.

Cell-surface expression of ICAM-1 is highly upregulated in the course of acute and chronic inflammation, which makes ICAM-1 a target for inflammatory diseases. We chose human dermal microvascular endothelial cells (HMEC-1) and human acute monocytic leukemia cells (THP-1) as representative in vitro cellular models. As a model of inflammation, HMEC-1 and THP-1 were treated with endotoxin lipopolysaccharides (LPS) (Figure 3a) that would initiate nuclear factor-kappa B transcription factor-dependent inflammatory response [48] VMPs formulated with a fixed mass ratio of pGFP to PEI at 1:6 and varying amounts of targeting moiety were delivered to either normal or LPS-treated HMEC-1 (Figures 3b and c) and THP-1 cells (Figures 3d and e). Overall, LPS- or inflammation- dependent delivery of GFP gene was observed only with VMPs assembled with PAP-Id(HA), with 480% of cells being GFP-positive. Particles formed without the I domain showed a much lower efficiency of transfection independent of LPS treatment, which was largely abolished by the addition of serum. Notably, pGFP/PEI transfection caused cell death reaching as high as 90%, whereas VMPs with PAP-Id(HA) preserved the viability of both HMEC-1 and THP-1.

One of the major advantages of using the I domain for targeted delivery is that it cross-reacts with murine ICAM-1 [42, 43], allowing the same targeting moiety to be used for preclinical animal studies. Similarly, we chose two types of cells, mouse brain microvascular endothelial cells (bEnd.3) and mouse leukemic monocyte macrophage cells (RAW 264.7), to study inflammation- specific delivery of VMPs bearing pGFP. Overall, the induction of ICAM-1 in murine cells in response to LPS was slower than in human cells; accordingly, we delivered VMPs at 48 h post-LPS treatment (Figure 4a). Similar to the effects of VMPs on human cells, mean fluorescence intensity and the percentage of GFP-positive cells for both bEnd.3 and RAW 264.7 were significantly higher in the group that were treated with LPS

**Figure 3.** Inflammation-specific targeted gene delivery to human endothelial cells and monocyte/macrophages. (a) Timeline shows the sequence of LPS treatment, virus-particle delivery and measurements for human cell lines. Twenty-four hours of LPS treatment was required in human cells to trigger maximal ICAM-1 expression level for optimal delivery. (b–e) VMPs were formed with varying mass ratios of the components, pGFP, PEI and PAP-Id, and were delivered to either normal or LPS-treated HMEC-1 and human acute monocytic leukemia cells (THP-1). A fixed mass ratio of 1:6 between pGFP and PEI was used for all cases. Mass ratios of PAP-Id(HA) was titrated to assess the effect of avidity on the efficiency of ICAM-1-mediated endocytosis and gene delivery in human cell lines. PAP-Id(D137A) was used as a negative control. (b, d) Cells were analyzed for mean fluorescence intensity and percentage of GFP-positive cells by flow cytometry (n = 4). (b, d) Cell viability was measured by MTT assay (n = 4). Data represent mean ± s.d. (c, e) Representative fluorescence and light microscopic images of the optimal mass ratio (pGFP:PEI:PAP-Id adjusted to 1:6:16) are shown. Bar = 50 μm.

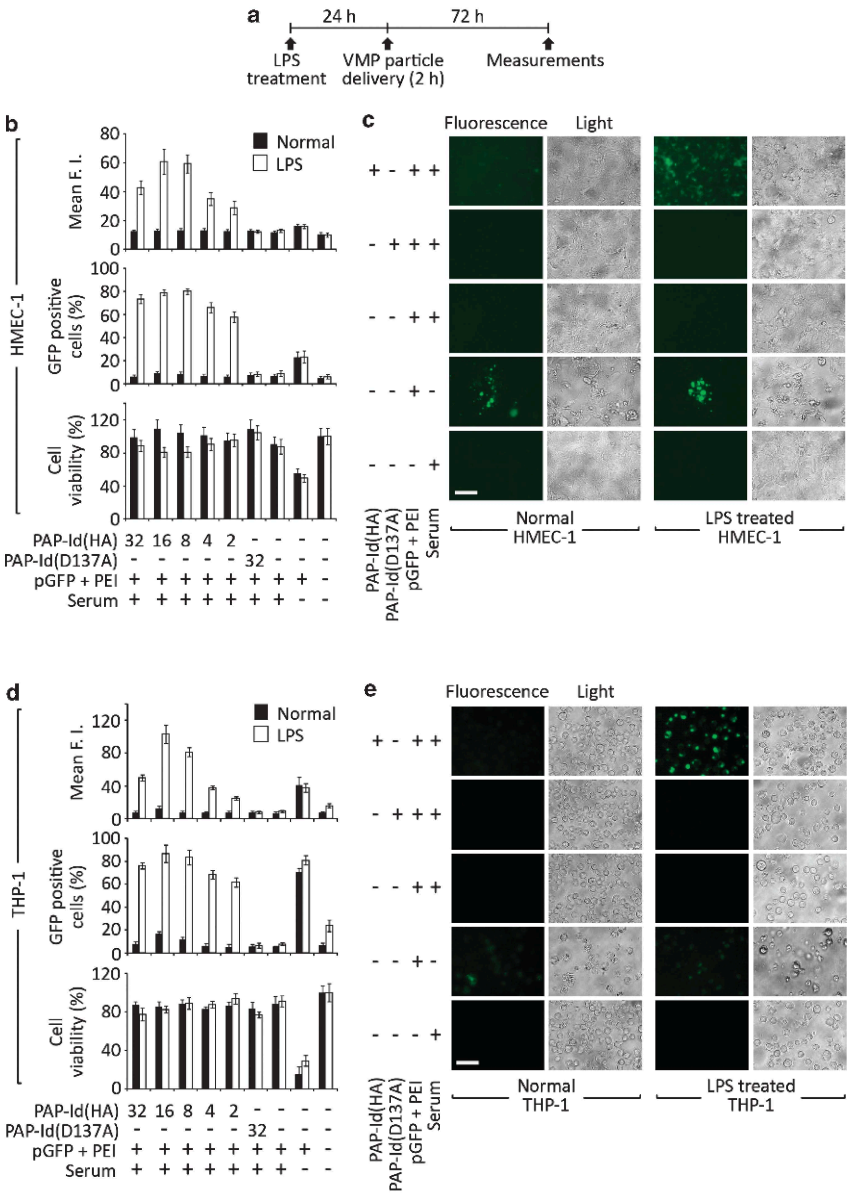
a
24 h
72 h
LPS treatment
VMP particle delivery (2 h)
Measurements
b
HMEC-1
Mean F. I.
GFP positive cells (%)
Cell viability (%)
Normal
LPS
PAP-Id(HA) 32 16 8 4 2 - - - -
PAP-Id(D137A) - - - - - 32 - - -
pGFP + PEI + + + + + + + + -
Serum + + + + + + + - -
c
Fluorescence
Light
PAP-Id(HA)
PAP-Id(D137A)
pGFP + PEI
Serum
Normal HMEC-1
LPS treated HMEC-1
d
THP-1
Mean F. I.
GFP positive cells (%)
Cell viability (%)
Normal
LPS
PAP-Id(HA) 32 16 8 4 2 - - - -
PAP-Id(D137A) - - - - - 32 - - -
pGFP + PEI + + + + + + + + -
Serum + + + + + + + - -
e
Fluorescence
Light
PAP-Id(HA)
PAP-Id(D137A)
pGFP + PEI
Serum
Normal THP-1
LPS treated THP-1

**Figure 4.** Inflammation-specific targeted gene delivery to mouse endothelial cells and monocyte/macrophages. (a) Timeline shows the sequence of LPS treatment, virus-particle delivery and measurements for mouse cell lines. LPS was treated for 48 h in mouse cells to reach maximal ICAM-1 expression level for optimal delivery. (b–e) VMPs were formed with varying mass ratios of the components, pGFP, PEI and PAP-Id, and were delivered to either normal or LPS-treated bEnd.3 and RAW 264.7. A fixed mass ratio of 1:6 between pGFP and PEI was used for all cases. Mass ratios of PAP-Id(HA) was titrated to assess the effect of avidity on the efficiency of ICAM-1-mediated endocytosis and gene delivery in mouse cell lines. PAP-Id(D137A) was used as a negative control. (b, d) Cells were analyzed for mean fluorescence intensity and percentage of GFP-positive cells by flow cytometry (n = 4). (b, d) Cell viability was measured by MTT assay (n = 4). Data represent mean ± s.d. (c, e) Representative fluorescence and light microscopic images of the optimal mass ratio (pGFP:PEI:PAP-Id adjusted to 1:6:16) are shown. Scale bar = 50 μm.

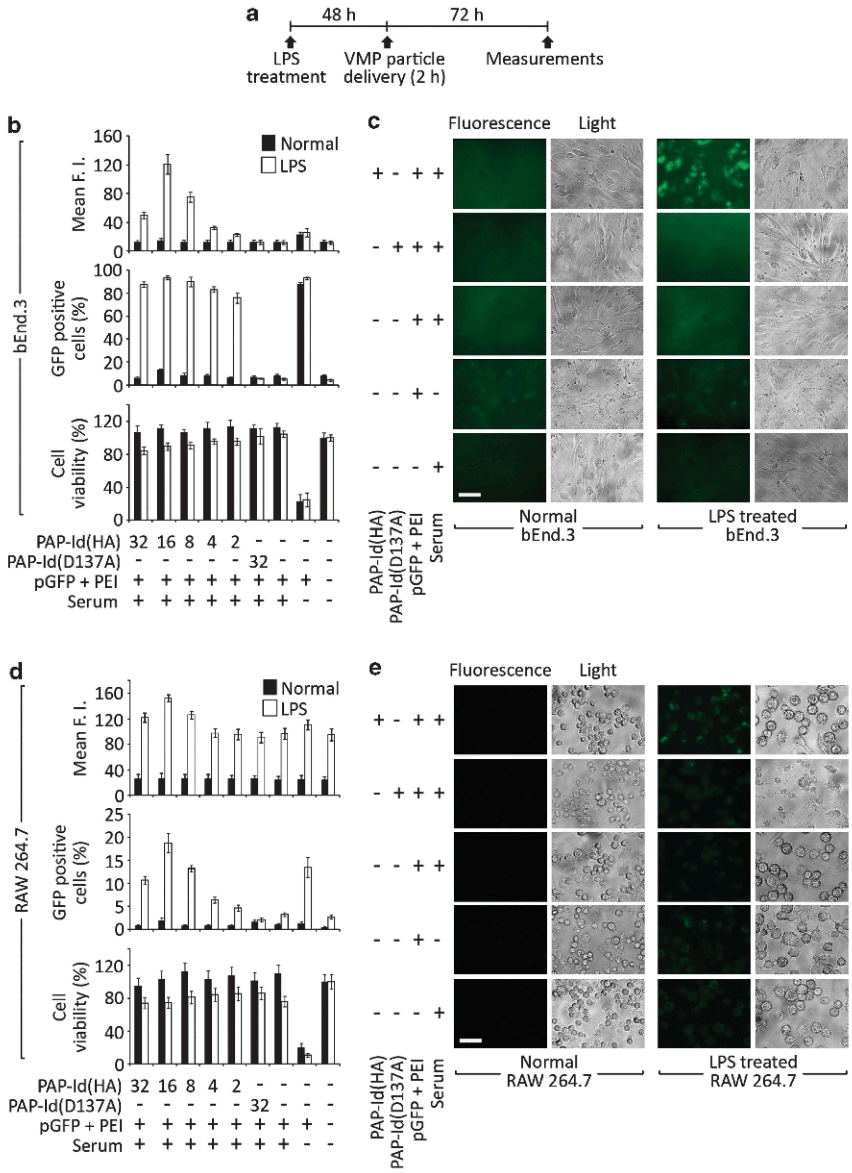
a
48 h
72 h
LPS treatment
VMP particle delivery (2 h)
Measurements
b
bEnd.3
Normal
LPS
Mean F. I.
GFP positive cells (%)
Cell viability (%)
PAP-Id(HA) 32 16 8 4 2 - - - -
PAP-Id(D137A) - - - - - 32 - - -
pGFP + PEI + + + + + + + + -
Serum + + + + + + + - -
c
Fluorescence
Light
PAP-Id(HA)
PAP-Id(D137A)
pGFP + PEI
Serum
Normal bEnd.3
LPS treated bEnd.3
d
RAW 264.7
Normal
LPS
Mean F. I.
GFP positive cells (%)
Cell viability (%)
PAP-Id(HA) 32 16 8 4 2 - - - -
PAP-Id(D137A) - - - - - 32 - - -
pGFP + PEI + + + + + + + + -
Serum + + + + + + + - -
e
Fluorescence
Light
PAP-Id(HA)
PAP-Id(D137A)
pGFP + PEI
Serum
Normal RAW 264.7
LPS treated RAW 264.7

and received VMPs formed with PAP-Id(HA) (Figures 4b–e). pGFP/PEI without added serum resulted in up to 90% GFP-positive in bEnd.3, irrespective of LPS treatment (Figures 4b and c). RAW 264.7 after treatment with LPS became enlarged and autofluorescent, resulted in an increase in fluorescence intensity across all conditions (Figures 4d and e). Nonetheless, PAP-Id(HA)-mediated delivery resulted in a significant increase in fluorescence and as much as 20% cells were determined GFP-positive (Figures 4d and e). For LPS-treated RAW 264.7cells, pGFP/PEI particles delivered without serum resulted in B15% GFP-positive cells, ascribed to nonspecific phagocytic uptake of activated macro- phages. PAP-Id(HA)-mediated delivery preserved cell viability, while non-specific pGFP/PEI transfection caused significant cell death in both the cell lines.

*Inflammation-specific gene delivery to primary mouse lung cells*

We also studied gene delivery to primary mouse lung cells cultured in vitro, harvested from a transgenic mouse strain, where exogenous Cre recombinase would excise the loxP-flanked transcriptional STOP region and turn on GFP expression. We formed VMPs with a plasmid encoding Cre recombinase fused to nuclear localization signal under the CMV promoter. Similarly, cells were treated with LPS and received VMPs (Figure 5a), formulated with a fixed ratio of pCRE to PEI (1:6) and with varying amounts of PAP-Id (Figure 5b). PAP-Id(HA)-mediated delivery was specific to LPS-treated cells, evidenced by increased mean fluorescence intensity (Figures 5b and c). Normal cells treated with VMPs were as high as 40% GFP-positive, presumably because even a low copy number of Cre recombinase can excise STOP signal and induce GFP expression. PAP-Id(HA)-mediated delivery to LPS-treated cells, however, resulted in 90% GFP-positive cells. Conventional transfection of

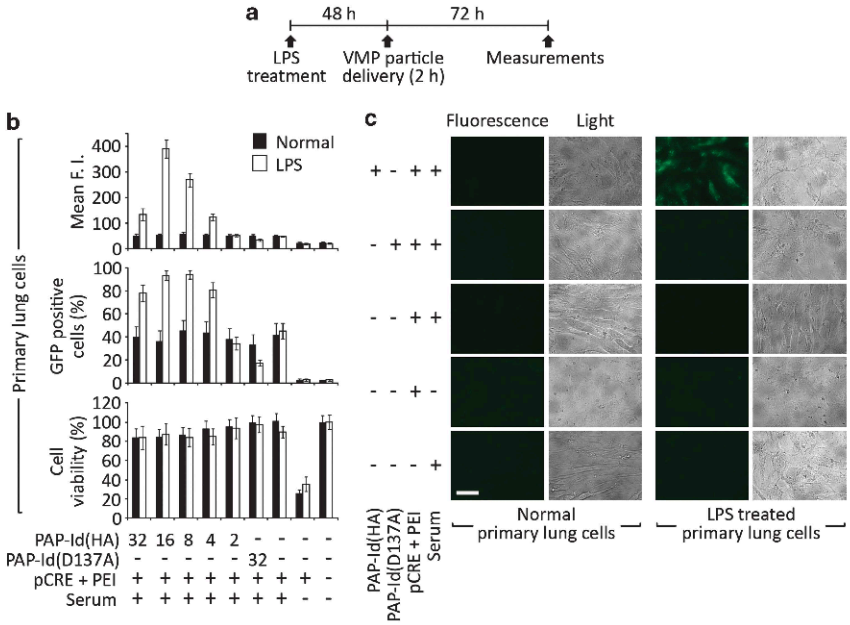


**Figure 5.** Inflammation-specific targeted delivery to primary mouse lung cells. (a) Timeline shows the sequence of treatments for VMP delivery to primary mouse lung cells in culture. Lung cells were harvested from a mouse strain engineered for inducible expression of GFP after Cre recombinase-mediated loxP-STOP-loxP excision. (b) VMPs were assembled with pCRE (Cre recombinase) and delivered to either normal or LPS treated primary mouse lung cells. A fixed mass ratio of 1:6 between pCRE and PEI was used for all cases. Mass ratios of PAP-Id(HA) was titrated to assess the effect of avidity on the efficiency of ICAM-1-mediated endocytosis and gene delivery in primary lung cells. PAP-Id(D137A) was used as a negative control. Cells were analyzed for mean fluorescence intensity and percentage of GFP-positive cells by flow cytometry (n = 4). Cell viability was measured by MTT assay (n = 4). Data represent mean ± s.d. c) Representative fluorescence and light microscopic images of the optimal mass ratio (pCRE:PEI:PAP-Id adjusted to 1:6:16) are shown. Bar = 50 μm.

**Figure 6.** Systemic and inflammation-specific targeted gene delivery to the mouse lung in vivo. (a) Cell-surface expression of ICAM-1 in CD31- positive endothelial cells and (b) F4/80-positive monocyte/macrophages in the mouse lung was detected by flow cytometry with I domain fused to GFP (GFP-Id(HA)) (n = 4). Lungs were collected 72 h after systemic LPS injection for comparison of the level of ICAM-1 expression between normal and inflamed states. Percentage of cells in each quadrant is shown. (c–g) VMPs bearing pGFP was systemically applied in vivo to target inflamed mouse lung. Mass ratio of the components of VMPs was fixed to 1:6:16 (pGFP:PEI:PAP-Id). VMPs were injected intravenously via lateral tail vein route into either normal or LPS-treated mice (BALB/c). (c) Timeline shows the sequence of treatments, injections and data collection. (d) Lungs were collected and analyzed for GFP mRNA expression by quantitative PCR. Expression was normalized to a housekeeping gene (CYC1) and presented as relative fold difference as compared with PAP-Id(D137A) case (n = 4). PAP-Id(HA)-mediated delivery to LPS-treated group was statistically significant among all the groups. Data represent mean ± s.d. (*$P < 0.05$, one-way analysis of variance followed by Tukey's post-hoc test). (e) Flow cytometric histograms show GFP expression assessed by immunostaining of fixed/ permeabilized lung cells (n = 4). Lung cells were dual labeled for GFP and for either CD31 or F4/80 and were analyzed for the percentage of GFP-positive cells (black dots) within (f) CD31-positive or (g) F4/80-positive subset (yellow region and dotted box). FSC, forward scatter; NS, not significant.

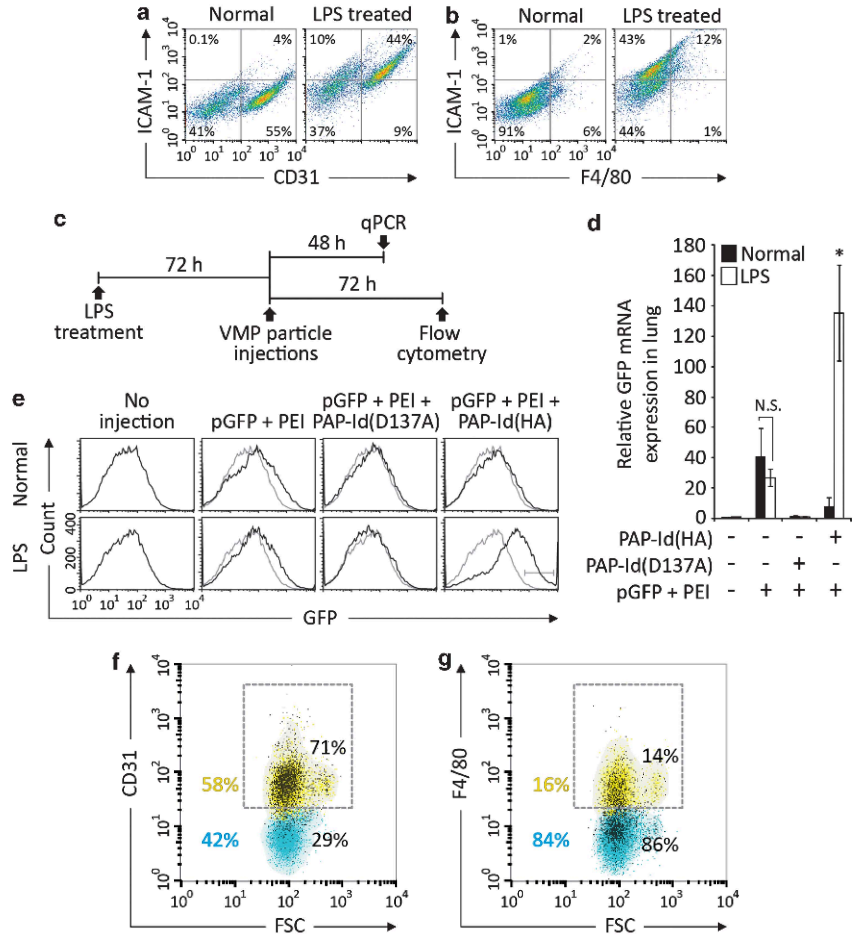
a
Normal
LPS treated
ICAM-1
CD31
0.1%
4%
41%
55%
10%
44%
37%
9%
b
Normal
LPS treated
ICAM-1
F4/80
1%
2%
91%
6%
43%
12%
44%
1%
c
qPCR
48 h
72 h
72 h
LPS treatment
VMP particle injections
Flow cytometry
d
Normal
LPS
Relative GFP mRNA expression in lung
N.S.
*
PAP-Id(HA)
PAP-Id(D137A)
pGFP + PEI
e
No injection
pGFP + PEI
pGFP + PEI + PAP-Id(D137A)
pGFP + PEI + PAP-Id(HA)
Normal
LPS
Count
GFP
f
CD31
FSC
71%
58%
42%
29%
g
F4/80
FSC
14%
16%
84%
86%

pCRE/PEI in serum-free media resulted in a significant cytotoxicity of primary cells, whereas no cell death was observed with fully assembled VMPs.

*Inflammation-specific targeted gene delivery of VMPs in vivo*

Gene delivery has the potential to treat many diseases, which may benefit much from systemic and targeted treatments via intravenous routes. Cationic nonviral gene delivery systems without molecular targeting are severely limited due to loss of efficiency in cell entry, inhibited by negatively charged molecules (for example, glycosaminoglycans) in blood serum. We chose to study the delivery of VMPs to the lung, where endothelial cells comprise a large portion of tissue composition. We also confirmed that cell-surface expression of ICAM-1 is highly upregulated in the lungs after systemic LPS treatment.

As for specific cell types, upregulation of ICAM-1 was observed in 450% of CD31-positive cells (Figure 6a), which consist of mainly endothelial cells and small percentages of a subset of immune cells. We also found a comparable level of ICAM-1 induction in F4/80-positive myeloid lineage macrophages, which participate critically in inflammatory diseases, including atherosclerosis and cancer (Figure 6b). We injected VMPs bearing pGFP via the lateral tail vein route, either to normal or LPS-treated mice (BALB/c) (Figure 6c). Relative amount of GFP mRNA expression in the lung was analyzed at 48 h post injection of VMPs (Figure 6d). PAP-Id(HA)-mediated delivery was specific to LPS-treated group, whereas pGFP/PEI particles had a lower gene transfer efficiency irrespective of the induction of inflammation (Figure 6d). Similarly, gene delivery by VMPs formulated with PAP-Id(D137A) was ineffective (Figure 6d). VMP delivery for GFP expression in the lung was also assessed at 72 h post delivery by immunostaining of fixed/permeabilized and

collagenase-digested lung cells (Figure 6e). Gene delivery by VMPs with PAP-Id(HA) was specific to LPS-treated group, resulting in nearly 15% of the entire cell population being GFP-positive, while pGFP/PEI particles produced much less GFP-positive cells irrespective of inflammatory condition (Figure 6e). We further analyzed for the types of cells that were targeted by PAP-Id(HA)-mediated delivery (Figures 6f and g). Specifically, 71% of GFP-positive cells were CD31-positive cells (Figure 6f), whereas only about 14% of GFP-positive cells were F4/80-positive (Figure 6g). This finding demonstrates that intravenous delivery of VMPs was mainly against the cellular components that are directly accessible to the agents in circulation and express high levels of ICAM-1 in response to LPS treatment.

**Discussion**

In this study, we have demonstrated that VMPs can be formulated by functionalizing PEI with a PAP for fusion to targeting moieties, allowing systemic and molecular interaction-dependent gene delivery. With the targeting moiety derived from the integrin LFA-1, our VMPs were highly selective to cells with inflammation-induced overexpression of ICAM-1. VMPs mimicked some of the essential properties of non-enveloped viruses by possessing the ability to (a) package large nucleic acid molecules by PEI-mediated condensation, (b) bind specifically to cell-surface receptors, (c) elicit receptor-mediated endocytosis, (d) escape endosomal degradation (attributed to the proton sponge effect of PEI) and (e) express the payload gene with high efficiency.

VMPs were far more efficient in delivering genes to cells with overexpressed ICAM-1 than cells at basal level, which enabled inflammation-specific delivery both in vitro and in

vivo. This is analogous to HRVs that displayed enhanced infectivity when host cells were treated with inflammatory cytokines and upregulated ICAM-1 [49]. The efficiency of gene transfer by VMPs was also largely dependent on the coating density or avidity of PAP-Id, as it would influence the degree of multimeric interaction with ICAM-1 necessary for receptor-mediated endocytosis. Furthermore, in contrast to toxicity-laden conventional transfection by PEI due to plasma membrane destabilization associated with non-specific internalization, molecular interaction-dependent uptake of VMPs produced little cytotoxicity. We speculate that, unlike how nonspecific uptake of densely charged cationic particles can damage cell membranes and cause cell death [9], viability may have been maintained as receptor-mediated endocytosis is an active cellular process that can be regulated by cells. Greatly reduced toxicity with VMPs is also ascribed to the presence of PAP that counterbalances positive charges of PEI.

By targeting ICAM-1, VMPs delivered genes mostly to CD31- positive cells in the lung, which are predominantly composed of pulmonary endothelial cells. With the current detection method of gene expression, we failed to observe GFP expression in other organs, including the liver, despite accumulation of VMPs therein. Although further work is required to finely control the size of VMPs and its subsequent effects on biodistribution, clearance rate and other pharmacokinetic parameters with the given size of VMPs (150–250nm in diameter), we expect that targeted cells would mainly be the ones that reside in the blood-accessible stroma as opposed to the parenchyma. However, endothelial cells as well as immune cells such as monocytes/macrophages have been implicated to have critical roles in the pathology of inflammatory diseases, especially in the cases of atherosclerosis [47], psoriasis and arthritis [50]. The ability to deliver corrective genes specifically to these types

of cells under dysregulated inflammation should provide an immense therapeutic opportunity, even without the access to the parenchyma.

Apart from the ability of viruses to efficiently deliver genes into host cells, they also have evolved mechanisms to self-replicate their genome, elude the immune system by synthesizing viral cytokine homologues and over-ride host cellular component or activity. Likewise, the use of more advanced genetic materials (for example, plasmids with promoters for improved expression or cell type-specific expression, mechanisms for self-replication/integration or functions that can be activated under disease-associated cellular activities) may further improve VMPs for enhanced gene transfer efficiency, specificity and safety. Finally, we anticipate that simplicity and versatility of the system developed in this study may facilitate rapid assessments of multifaceted VMPs, formed with a range of different targeting moieties and payloads, and contribute to successful translation of nonviral vectors into the clinic.

# REFERENCES


1. Hacein-Bey-Abina S, Hauer J, Lim A, Picard C, Wang GP, Berry CC et al. Efficacy of gene therapy for X-linked severe combined immunodeficiency. N Engl J Med 2010; 363: 355–364.
2. Bainbridge JW, Smith AJ, Barker SS, Robbie S, Henderson R, Balaggan K et al. Effect of gene therapy on visual function in Leber's congenital amaurosis. N Engl J Med 2008; 358: 2231–2239.
3. Manno CS, Pierce GF, Arruda VR, Glader B, Ragni M, Rasko JJ et al. Successful transduction of liver in hemophilia by AAV-Factor IX and limitations imposed by the host immune response. Nat Med 2006; 12: 342–347.
4. Mendell JR, Campbell K, Rodino-Klapac L, Sahenk Z, Shilling C, Lewis S et al. Dystrophin immunity in Duchenne's muscular dystrophy. N Engl J Med 2010; 363: 1429–1437.
5. Breitbach CJ, Burke J, Jonker D, Stephenson J, Haas AR, Chow LQ et al. Intravenous delivery of a multi-mechanistic cancer-targeted oncolytic poxvirus in humans. Nature 2011; 477: 99–102.
6. McCormack MP, Rabbitts TH. Activation of the T-cell oncogene LMO2 after gene therapy for X-linked severe combined immunodeficiency. N Engl J Med 2004; 350: 913–922.
7. Yang Y, Nunes FA, Berencsi K, Furth EE, Gonczol E, Wilson JM. Cellular immunity to viral antigens limits E1-deleted adenoviruses for gene therapy. Proc Natl Acad Sci USA 1994; 91: 4407–4411.
8. Yang Y, Li Q, Ertl HC, Wilson JM. Cellular and humoral immune responses to viral antigens create barriers to lung-directed gene therapy with recombinant adenoviruses. J Virol 1995; 69: 2004–2015.
9. Lv H, Zhang S, Wang B, Cui S, Yan J. Toxicity of cationic lipids and cationic polymers in gene delivery. J Control Release 2006; 114: 100–109.
10. Luo D, Saltzman WM. Synthetic DNA delivery systems. Nat Biotechnol 2000; 18: 33–37.

11. Moret I, Esteban Peris J, Guillem VM, Benet M, Revert F, Dasi F et al. Stability of PEI- DNA and DOTAP-DNA complexes: effect of alkaline pH, heparin and serum. J Control Release 2001; 76: 169–181.
12. Staprans I, Felts JM. Isolation and characterization of glycosaminoglycans in human plasma. J Clin Invest 1985; 76: 1984–1991.
13. Ruponen M, Yla-Herttuala S, Urtti A. Interactions of polymeric and liposomal gene delivery systems with extracellular glycosaminoglycans: physicochemical and transfection studies. Biochim Biophys Acta 1999; 1415: 331–341.
14. Kumar P, Ban HS, Kim SS, Wu H, Pearson T, Greiner DL et al. T cell-specific siRNA delivery suppresses HIV-1 infection in humanized mice. Cell 2008; 134: 577–586.
15. Peer D, Park EJ, Morishita Y, Carman CV, Shimaoka M. Systemic leukocyte-directed siRNA delivery revealing cyclin D1 as an anti-inflammatory target. Science 2008;319: 627–630.
16. Song E, Zhu P, Lee SK, Chowdhury D, Kussman S, Dykxhoorn DM et al. Antibody mediated in vivo delivery of small interfering RNAs via cell-surface receptors. Nat Biotechnol 2005; 23: 709–717.
17. Davis ME, Zuckerman JE, Choi CH, Seligson D, Tolcher A, Alabi CA et al. Evidence of RNAi in humans from systemically administered siRNA via targeted nanoparticles. Nature 2010; 464: 1067–1070.
18. Waehler R, Russell SJ, Curiel DT. Engineering targeted viral vectors for gene therapy. Nat Rev Genet 2007; 8: 573–587.
19. Maheshri N, Koerber JT, Kaspar BK, Schaffer DV. Directed evolution of adeno-associated virus yields enhanced gene delivery vectors. Nat Biotechnol 2006; 24:198–204.
20. Douglas JT, Rogers BE, Rosenfeld ME, Michael SI, Feng M, Curiel DT. Targeted gene delivery by tropism-modified adenoviral vectors. Nat Biotechnol 1996; 14: 1574–1578.
21. Lee RJ, Huang L. Folate-targeted, anionic liposome-entrapped polylysine- condensed DNA for tumor cell-specific gene transfer. J Biol Chem 1996; 271:8481–8487.

22. Erbacher P, Remy JS, Behr JP. Gene transfer with synthetic virus-like particles via the integrin-mediated endocytosis pathway. Gene Therapy 1999; 6: 138–145.
23. Ogris M, Brunner S, Schuller S, Kircheis R, Wagner E. PEGylated DNA/transferrin-PEI complexes: reduced interaction with blood components, extended circulation in blood and potential for systemic gene delivery. Gene Therapy 1999; 6: 595–605.
24. Wagner E, Zenke M, Cotten M, Beug H, Birnstiel ML. Transferrin-polycation conjugates as carriers for DNA uptake into cells. Proc Natl Acad Sci USA 1990; 87:3410–3414.
25. Boussif O, Lezoualc'h F, Zanta MA, Mergny MD, Scherman D, Demeneix B et al. A versatile vector for gene and oligonucleotide transfer into cells in culture and in vivo: polyethylenimine. Proc Natl Acad Sci USA 1995; 92: 7297–7301.
26. Sadeqzadeh E, Rahbarizadeh F, Ahmadvand D, Rasaee MJ, Parhamifar L, Moghimi SM. Combined MUC1-specific nanobody-tagged PEG-polyethylenimine polyplex targeting and transcriptional targeting of tBid transgene for directed killing of MUC1 over-expressing tumour cells. J Control Release 2011; 156: 85–91.
27. Somiya M, Yoshimoto N, Iijima M, Niimi T, Dewa T, Jung J et al. Targeting of polyplex to human hepatic cells by bio-nanocapsules, hepatitis B virus surface antigen L protein particles. Bioorg Med Chem 2012; 20: 3873–3879.
28. Hildebrandt IJ, Iyer M, Wagner E, Gambhir SS. Optical imaging of transferrin targeted PEI/DNA complexes in living subjects. Gene Therapy 2003; 10: 758–764.
29. Kunath K, von Harpe A, Fischer D, Kissel T. Galactose-PEI-DNA complexes for targeted gene delivery: degree of substitution affects complex size and transfection efficiency. J Control Release 2003; 88: 159–172.
30. Godbey WT, Wu KK, Mikos AG. Poly(ethylenimine) and its role in gene delivery. J Control Release 1999; 60: 149–160.
31. Sonawane ND, Szoka Jr FC, Verkman AS. Chloride accumulation and swelling in endosomes enhances DNA transfer by polyamine-DNA polyplexes. J Biol Chem 2003; 278: 44826–44831.
32. Akinc A, Thomas M, Klibanov AM, Langer R. Exploring polyethylenimine-mediated DNA transfection and the proton sponge hypothesis. J Gene Med 2005; 7: 657–663.

33. Dustin ML, Rothlein R, Bhan AK, Dinarello CA, Springer TA. Induction by IL 1 and interferon-gamma: tissue distribution, biochemistry, and function of a natural adherence molecule (ICAM-1). J Immunol 1986; 137: 245–254.
34. Marlin SD, Springer TA. Purified intercellular adhesion molecule-1 (ICAM-1) is a ligand for lymphocyte function-associated antigen 1 (LFA-1). Cell 1987; 51: 813–819.
35. Albelda SM, Smith CW, Ward PA. Adhesion molecules and inflammatory injury. FASEB J 1994; 8: 504–512.
36. van de Stolpe A, van der Saag PT. Intercellular adhesion molecule-1. J Mol Med (Berl) 1996; 74: 13–33.
37. Tomassini JE, Graham D, DeWitt CM, Lineberger DW, Rodkey JA, Colonno RJ. cDNA cloning reveals that the major group rhinovirus receptor on HeLa cells is intercellular adhesion molecule 1. Proc Natl Acad Sci USA 1989; 86: 4907–4911.
38. Grunert HP, Wolf KU, Langner KD, Sawitzky D, Habermehl KO, Zeichhardt H. Internalization of human rhinovirus 14 into HeLa and ICAM-1-transfected BHK cells. Med Microbiol Immunol 1997; 186: 1–9.
39. Muro S, Wiewrodt R, Thomas A, Koniaris L, Albelda SM, Muzykantov VR et al. A novel endocytic pathway induced by clustering endothelial ICAM-1 or PECAM-1. J Cell Sci 2003; 116(Pt 8): 1599–1609.
40. Jin M, Song G, Carman CV, Kim YS, Astrof NS, Shimaoka M et al. Directed evolution to probe protein allostery and integrin I domains of 200,000-fold higher affinity. Proc Natl Acad Sci USA 2006; 103: 5758–5763.
41. Park S, Kang S, Veach AJ, Vedvyas Y, Zarnegar R, Kim JY et al. Self-assembled nanoplatform for targeted delivery of chemotherapy agents via affinity-regulated molecular interactions. Biomaterials 2010; 31: 7766–7775.
42. Kang S, Park T, Chen X, Dickens G, Lee B, Lu K et al. Tunable physiologic interactions of adhesion molecules for inflamed cell-selective drug delivery. Biomaterials 2011; 32: 3487–3498.
43. Chen X, Wong R, Khalidov I, Wang AY, Leelawattanachai J, Wang Y et al. Inflamed leukocyte-mimetic nanoparticles for molecular imaging of inflammation. Biomaterials 2011; 32: 7651–7661.

44. Huth JR, Olejniczak ET, Mendoza R, Liang H, Harris EA, Lupher Jr. ML et al. NMR and mutagenesis evidence for an I domain allosteric site that regulates lymphocyte function-associated antigen 1 ligand binding. Proc Natl Acad Sci USA 2000; 97: 5231–5236.
45. Choe S, Bennett MJ, Fujii G, Curmi PM, Kantardjieff KA, Collier RJ et al. The crystal structure of diphtheria toxin. Nature 1992; 357: 216–222.
46. Coussens LM, Werb Z. Inflammation and cancer. Nature 2002; 420: 860–867.
47. Ross R. Atherosclerosis—an inflammatory disease. N Engl J Med 1999; 340:115–126.
48. Chow JC, Young DW, Golenbock DT, Christ WJ, Gusovsky F. Toll-like receptor-4 mediates lipopolysaccharide-induced signal transduction. J Biol Chem 1999; 274:10689–10692.
49. Subauste MC, Jacoby DB, Richards SM, Proud D. Infection of a human respiratory epithelial cell line with rhinovirus. Induction of cytokine release and modulation of susceptibility to infection by cytokine exposure. J Clin Invest 1995; 96: 549–557.
50. Folkman J. Angiogenesis in cancer, vascular, rheumatoid and other disease. Nat Med 1995; 1: 27–31.

# CHAPTER 5

# CONCLUSIONS AND FUTURE DIRECTIONS

The major requirement for the success in cancer intervention is specific and efficient cancer cell targeting with minimal off-target effect. Since Paul Ehrlich suggested the concept of a "magic bullet" in 1960, "a drug that selectively attaches to diseased cells but is not toxic to healthy cells" [1, 2], a great deal of effort has been made for this direction. A wide range of factors can affect nanomedicine performance in cancer targeting, including but not limited to size, shape, clearance rate from blood, specificity, and affinity for target antigens [3-6]. The properties inherent to tumor itself also influence sensitivity and specificity of biologics in molecular imaging, such as size, tendency for non-specific uptake, vascular and lymphatic supplies, and permeability within the tumor [4, 7-10]. In this dissertation, I have investigated the influence of size and specificity on pharmacokinetics, biodistribution, and tumor targeting. Using six different commonly used biologics in the clinic as the study models, it was found that even though the highest localization into the tumor was obtained with full-length antibody specific to tumor antigen, serum albumin and streptavidin were overall superior in tumor to blood ratios. Moreover, to our surprise, Fab format of antibodies, comparable in size to albumin and streptavidin, were much inferior in tumor detection to albumin and streptavidin, partly due to faster clearance of Fab from the blood. In addition, despite high level of localization into the tumor, neither control antibodies nor albumin and streptavidin were found inside cells. This perhaps partially explains why several currentl-approved nanomedicines using passive targeting strategy, e.g. Doxil (PEGylated liposomal

doxorubicin), Abraxane (albumin-based pacitaxel), and Genexol-PM (Micellar paclitaxel), failed to demonstrate significant benefit at the preclinical or clinical level, even though they have been observed to highly accumulate in tumor tissue as well as superior lower toxicity. In summary, our study in chapter 2 emphasizes that specific tumor detection by molecular targeting needs to be validated by comparing its biodistribution and targeting with that of control antibodies or other biologics (e.g., albumin). Furthermore, the use of biologics as a cytotoxic drug carrier will require specificity to tumor markers in order to achieve both localization and internalization to tumor cells. Utilizing information from our pharmacokinetics, biodistribution, and tumor targeting studies in vivo, we developed two different targeted delivery systems for both imaging and delivery applications. Our delivery systems include SPIO nanoparticles (chapter 3) and polyplex nanoparticles (chapter 4). Both systems implemented active targeting strategies to cancer cells as well as tumor-associated endothelial cells via ICAM-1. Our targeted delivery systems demonstrated preferential localization to tumor, inflamed vasculature, as well as systemic and subcutaneous inflammation. We anticipate that this work may greatly contribute to a successful translation of molecular imaging and therapeutic delivery systems into the clinic.

**Future Directions**

Targeted delivery systems are currently in active research areas. Several systems have been proposed so far. Each of them has their own pros and cons. As with others, our systems still need to be improved. To make targeted delivery systems safer, more efficient, and more applicable in clinical settings, several factors need to be taken into consideration. In this

dissertation, we have focused our attention to the delivery of targeted nanomedicine to tumors and inflammation via ICAM-1 interaction. Here are the potential factors that could enhance the targeting capability of our systems.

First, our studies as well as several other studies in the field of tumor-targeting drug delivery utilized xenografted mouse models; the most frequently used animal models. Human cancer cells generally grow faster in immunocompromised mice than in humans. If a subcutaneously inoculated tumor in a mouse grows to 1 cm (~0.5 g) within 2–4 weeks, this would comparable to a ~20 cm and ~1–2 kg tumor in humans, which would take years, instead of weeks, to establish [11]. Because of this rapid growth, blood vessels in mouse tumors typically do not develop properly, and they consequently tend to be much more leaky than their human counterparts. This leads to such a major pitfall that the EPR effect is often overrated and/or misinterpreted. As a matter of fact, almost all nanomedicines, regardless of targeting strategies, primarily rely on EPR effect for their passive distribution through the tumor vasculatures and tissue for tumor localization. This might explain why some of the very promising nanomedicines that worked very well in mouse models, failed to demonstrate significant benefit at the clinical level. Apart from overestimation of the potential usefulness of passively targeted nanomedicine formulations, another important aspect to keep in mind is the heterogeneity of EPR effect, which varies substantially from tumor to tumor, as well as from patient to patient [10, 12]. Therefore, I envision that it would be very helpful to incorporate some anatomical and (patho-) physiological information of each individual tumor while evaluating tumor-targeting efficacy. In addition, it would be of clinical importance to investigate tumor-targeting efficacy of our targeted nanomedicines in different tumor models with diverse EPR effect levels. Focusing especially on the case of properly differentiated

blood vessels and densely covered with pericytes and/or smooth muscle cells would be of great interest and it could take more than a year to grow such tumors in size relevant to human cancer patients.

The second important pitfall that could hamper the nanomedicine efficacy is tumor penetration ability. Upon leaving tumor blood vessels, extravasated nanoparticles need to penetrate into and distribute across the interstitium, to reach as many cancer cells as possible. Due to the high tumor cell density and the high interstitial fluid pressure, we found our nanoparticle accumulated heterogeneously, limited and preferably highly accumulated in perivascular regions. This insight strongly suggests that attempts should be made to tailor the size of nanomedicines to one that enables long-circulation properties, but at the same time also allows for proper extravasation and penetration. I reason that multistage nanoparticle delivery system should potentially improve the penetration and the intratumoral distribution. Specifically, multistage nanoparticles could offer initial benefit from their relatively large size to ensure prolonged circulation time. However upon extravasation, they should be degraded to ~10 nm-sized 'sub-particles' by tumor-associated proteases, such as matrix metalloproteinases, thereby enabling deep penetration into tumor tissue [13].

The last but not least, binding-site barrier phenomenon is another factor that need to be considered for our future targeting nanomedicine design[14]. The binding-site barrier is based on the notion that ligand-modified nanomedicines will bind to the first receptors they encounter, and therefore will not penetrate very deeply into the tumor. It could provide the perception that antibody with the highest affinity to the target antigen would not necessary result in the best therapeutic outcome, but the lower to medium affinity interaction could potentially be better suit for targeted delivery systems [15, 16]. In addition, specific uptake of

anti-ICAM/carrying nanoparticles directly correlated with nanoparticle avidity controlled by ligand surface density. High ligand surface density favors multivalent and avid binding of nanoparticles to off-target tissues with basal low expression target maker. Therefore in some cases reduction of ligand density may provide more selective targeting with optimal result [17]. Therefore, we should take into account and investigate the modulation of affinity and avidity of targeted delivery systems. By varying affinity and number of targeting molecules on the surface of nanoparticles, we could compare and optimize the delivery systems to provide better tumor penetration, enhance selectivity, and minimize off-target delivery into irrelevant tissues.

# REFERENCES


1. Strebhardt, K. and A. Ullrich, Paul Ehrlich's magic bullet concept: 100 years of progress. Nature reviews. Cancer, 2008. 8(6): p. 473-80.
2. Oriuchi, N., et al., Current status of cancer therapy with radiolabeled monoclonal antibody. Annals of nuclear medicine, 2005. 19(5): p. 355-65.
3. Chames, P., et al., Therapeutic antibodies: successes, limitations and hopes for the future. British journal of pharmacology, 2009. 157(2): p. 220-33.
4. Sanna, V., N. Pala, and M. Sechi, Targeted therapy using nanotechnology: focus on cancer. International journal of nanomedicine, 2014. 9: p. 467-83.
5. James, M.L. and S.S. Gambhir, A molecular imaging primer: modalities, imaging agents, and applications. Physiological reviews, 2012. 92(2): p. 897-965.
6. Ferrari, M., Cancer nanotechnology: opportunities and challenges. Nature reviews. Cancer, 2005. 5(3): p. 161-71.
7. Shi, J., et al., Self-assembled targeted nanoparticles: evolution of technologies and bench to bedside translation. Accounts of chemical research, 2011. 44(10): p. 1123-34.
8. Heneweer, C., et al., Magnitude of enhanced permeability and retention effect in tumors with different phenotypes: 89Zr-albumin as a model system. Journal of nuclear medicine : official publication, Society of Nuclear Medicine, 2011. 52(4): p. 625-33.
9. Jain, R.K., Transport of molecules, particles, and cells in solid tumors. Annual review of biomedical engineering, 1999. 1: p. 241-63.
10. Jain, R.K. and T. Stylianopoulos, Delivering nanomedicine to solid tumors. Nature reviews. Clinical oncology, 2010. 7(11): p. 653-64.
11. Lammers, T., et al., Drug targeting to tumors: principles, pitfalls and (pre-) clinical progress. Journal of controlled release : official journal of the Controlled Release Society, 2012. 161(2): p. 175-87.

12. Bae, Y.H. and K. Park, Targeted drug delivery to tumors: myths, reality and possibility. Journal of controlled release : official journal of the Controlled Release Society, 2011. 153(3): p. 198-205.
13. Wong, C., et al., Multistage nanoparticle delivery system for deep penetration into tumor tissue. Proceedings of the National Academy of Sciences of the United States of America, 2011. 108(6): p. 2426-31.
14. Juweid, M., et al., Micropharmacology of monoclonal antibodies in solid tumors: direct experimental evidence for a binding site barrier. Cancer research, 1992. 52(19): p. 5144-53.
15. Adams, G.P., et al., High affinity restricts the localization and tumor penetration of single-chain fv antibody molecules. Cancer research, 2001. 61(12): p. 4750-5.
16. Yu, Y.J., et al., Boosting brain uptake of a therapeutic antibody by reducing its affinity for a transcytosis target. Science translational medicine, 2011. 3(84): p. 84ra44.
17. Zern, B.J., et al., Reduction of nanoparticle avidity enhances the selectivity of vascular targeting and PET detection of pulmonary inflammation. ACS nano, 2013. 7(3): p. 2461-9.